

# **Modeling of induced flow anisotropy and its application to sheet metal forming**

Von der Fakultät Maschinenbau  
der Universität Dortmund  
zur Erlangung des Grades eines  
Doktor-Ingenieurs  
(Dr.-Ing.)  
genehmigte Dissertation

von

**Jian Wang**

Dortmund 2006



# Contents

<b>Summary</b>	<b>iii</b>
<b>1 Modeling and simulation of induced anisotropy in metals</b>	<b>1</b>
1.1 Introduction . . . . .	1
1.2 Basic framework . . . . .	2
1.3 Internal variables as structure tensors . . . . .	4
1.4 Application to metal inelasticity with hardening . . . . .	6
<b>2 Some numerical aspects of sheet metal forming and springback simulation</b>	<b>13</b>
2.1 Introduction . . . . .	13
2.2 Summary of material model . . . . .	14
2.3 Algorithmic formulation of the material model . . . . .	16
2.4 Shell element formulations . . . . .	19
2.5 Contact and friction modeling . . . . .	20
2.6 Convergence behavior and numerical integration . . . . .	22
2.7 Structural, process and boundary conditions . . . . .	28
2.8 Conclusions . . . . .	32
<b>3 On the modeling and simulation of directional hardening in metals</b>	<b>35</b>
3.1 Introduction . . . . .	35
3.2 Review of the Teodosiu and Hu model . . . . .	37
3.3 Algorithmic formulation and model behavior . . . . .	41
3.4 Alternative model for directional hardening . . . . .	45
3.5 Initial flow anisotropy and plastic spin . . . . .	48
3.6 Influence of material parameters . . . . .	50
3.7 Conclusions . . . . .	53
<b>4 Application of directional hardening modeling to the simulation of springback</b>	<b>55</b>
4.1 Introduction . . . . .	55
4.2 Material model . . . . .	56
4.3 Fully implicit and semi-implicit algorithmic formulations . . . . .	60
4.4 Application to springback prediction . . . . .	65
4.5 Conclusions . . . . .	77

<b>References</b>	<b>87</b>
<b>Acknowledgements</b>	<b>89</b>
<b>Curriculum Vitae</b>	<b>91</b>

# Summary

The modeling and simulation of forming processes and springback in sheet metal structures requires taking a number of physical processes into account and involves a number of algorithmic and numerical issues in the context of the finite-element method. On the material side, one must account for the effects of the material microstructural evolution on the material behavior due to complex, non-proportional loading-path histories involved. On the structural side, contact and friction between the tool and work-piece, as well as large deformation of very thin structures, are important. On the numerical side, issues such as the type of solution procedure, the type of element used, the mesh topology, as well as contact and friction algorithms, all play a role. The current work falls within this context and deals with selected aspects of the modeling and simulation of such processes in detail.

To this end, the thesis begins in Chapter 1 with a discussion of the thermodynamically-consistent formulation of material models for anisotropic elastic and inelastic behavior as based on the concept of evolving structure tensors. In this approach, all dependent constitutive fields (*e.g.*, stress) are by definition isotropic functions of the independent constitutive variables which include the evolving structure tensors. The evolution of these during loading results in an evolution of the anisotropy of the material. From an algorithmic point of view, the current approach leads to constitutive models which are quite amenable to numerical implementation. To demonstrate the applicability of the resulting constitutive formulation, we apply it to the case of metal plasticity with combined hardening involving both deformation- and permanently-induced anisotropy. Comparison of experimental and simulation results for the bending-tension of DP600 steel sheet-metal strips show good agreement.

Accurate simulation of forming and springback in sheet metal structures involves taking a number of processes into account. These include (i) complex loading path changes, (ii) contact and friction between the tool and work-piece, and (iii) the large deformations of very thin structures. In particular, (i) has a marked effect on the material, in particular the hardening, behavior, and has been investigated in more detail elsewhere (Wang et al., 2006a,d). In Chapter 2, attention is focused on some numerical aspects involved in such simulations. In particular, we examine the roles played by the element formulation as well as the type of contact and friction modeling, in the simulation of sheet metal forming. The goal here is an optimal choice of algorithms, element types, contact and friction modeling, as well as numerical control parameters in such a way that an efficient, robust and convergent solution is achieved.

Since standard combined hardening models do not account for additional hardening processes occurring during non-proportional (*e.g.*, orthogonal) loading-path changes, these must be extended accordingly. The third part (Chapter 3) of the thesis is concerned with the formulation of a phenomenological model for directional hardening effects in metals subject to non-proportional loading. This model is motivated by that of Teodosiu and Hu (1995, 1998). In their model, a fourth-order symmetric tensor-valued stress-like internal variable  $S$  is introduced

to account for the effect of the directional strength of planar dislocation structures on the material hardening behavior. The model for  $S$  is based on the formulation of evolution equations for its projections  $s^d$  parallel, and  $S^\ell$  orthogonal, to the current direction of (the rate of) plastic deformation. Several approaches have been proposed in the literature on how to integrate the evolution equations for  $s^d$  and  $S^\ell$  in order to obtain  $S$ , each leading to different physical results. The alternative model for directional hardening proposed here is based on an evolution relation for  $S$  itself. As in the model of Teodosiu and Hu (1995, 1998), this alternative model for directional hardening captures in particular hardening stagnation after a load reversal as well as cross hardening after an orthogonal strain-path change. Differences between the two models include their behavior during (i) monotonic shear loading and (ii) continuous strain-path changes. Besides this, plastic spin effects not accounted for in the Teodosiu model are taken into account in the current model.

Finally, in Chapter 4, the results of the previous two chapters are applied to the modeling and simulation of several sheet metal forming processes as well as springback. The first of these is the so-called draw-bending test, which has been widely used, in particular for the investigation of the effect of kinematic hardening and hardening stagnation on forming processes. Next, the so-called ring-splitting test for springback, as based on the deep-drawing of cylindrical cups, is simulated. Given the complex non-proportional loading history involved here, this test is in particular suited to the study of the contribution of directional hardening to the development of the residual stress state and to springback in such forming processes. In addition, the deep-drawing of a square box is considered. In particular, the simulation results for the draw-bending of the steel DP600 are used to show the significance of the hardening stagnation on the springback. With the help of the steel DC06, which exhibits a more pronounced directional hardening behavior than DP600, the initial application of the current model to the simulation of hardening effects on residual stresses during deep-drawing and subsequent springback in the ring-splitting test demonstrates its capabilities in the context of a non-trivial example involving complex non-proportional loading histories and in particular orthogonal strain-path changes. Lastly, in the case of square box, it was shown that in the areas where the load reversal dominates, the current model predicts lower residual stresses due to hardening stagnation, while in areas with strain-path changes close to orthogonal, it predicts higher residual stresses due to cross hardening effect.

# Zusammenfassung

Die Modellierung und Simulation von Umformprozessen samt Rückfederung erfordert die Berücksichtigung mehrerer physikalischer Prozesse und umfasst diverse algorithmische und numerische Aspekte im Rahmen der FE-Methoden. Auf der konstitutiven Seite hat man den Einfluss der mikrostrukturellen Entwicklung bei komplexen nichtproportionalen Belastungspfaden auf das Materialverhalten zu berücksichtigen. Auf der Strukturseite sind solche Aspekte wie Kontakt und Reibung zwischen dem Werkstück und den Werkzeugen sowie große Deformationen sehr dünner Strukturen von großer Bedeutung. Auf der numerischen Seite spielen die Lösungsprozedur, Elementtyp, Netztopologie sowie Kontakt- und Reibungsalgorithmus eine entscheidende Rolle. Die vorliegende Arbeit beschäftigt sich detailliert mit mehreren ausgewählten Aspekten der Modellierung und Simulation solcher Prozesse.

Zu diesem Zweck beginnt das erste Kapitel der Arbeit mit der Beschreibung der thermodynamisch konsistenten Formulierung anisotroper elastisch-plastischer Modelle, die auf dem Konzept sich entwickelnder Strukturtenoren basiert. Im Rahmen dieser Vorgehensweise sind alle abhängigen konstitutiven Variablen (z.B. die Spannung) per Definition isotrope Funktionen von den unabhängigen konstitutiven Variablen einschließlich der Strukturtenoren. Deren Entwicklung im Laufe des Deformationsprozesses induziert eine Anisotropie im Werkstoff. Algorithmisch gesehen führt diese Vorgehensweise zu Materialmodellen, die sich sehr gut zur numerischen Implementierung eignen. Um die Anwendbarkeit dieser konstitutiven Modelle zu demonstrieren, betrachten wir plastisch deformierbare metallische Werkstoffe mit kombinierter Verfestigung einschließlich anfänglicher und deformationsinduzierter Anisotropie. Der Vergleich experimenteller und numerischer Ergebnisse für den Streifenzugbiegeversuch an Streifen aus dem hochfesten Stahl DP600 zeigen eine gute Übereinstimmung.

Eine akkurate Simulation von Blechumformprozessen samt Rückfederung erfordert die Berücksichtigung mehrerer Aspekte. Diese Aspekte umfassen insbesondere (i) komplexe Belastungsrichtungswechseln, (ii) Kontakt und Reibung zwischen dem Werkzeug und dem Blech und (iii) große Deformationen dünner Strukturen. Vor allem (i) hat einen starken Einfluss auf die Mikrostruktur und das Materialverhalten, insbesondere das Verfestigungsverhalten, und wurde in (Wang et al., 2006a,d) untersucht. Im zweiten Kapitel ist das Augenmerk vor allem darauf gerichtet, welche Rolle die Elementformulierung sowie die Kontakt und Reibungsmodellierung in der Simulation von Blechumformprozessen spielen. Das Ziel dieses Kapitels ist es, den Algorithmus, den Elementtyp, die Kontakt- und Reibungsmodellierung sowie die numerischen Kontrollparameter so zu wählen, dass eine effiziente, robuste und konvergierte Lösung erreicht wird.

Weil die konventionellen Modelle mit nichtlinearer kombinierter Verfestigung die zusätzlichen Effekt, die bei nichtproportionaler (z.B. orthogonaler) Belastung auftreten, nicht abbilden können, müssen sie erweitert werden. Das dritte Kapitel befasst sich mit der Formulierung eines phänomenologischen Materialmodells für gerichtete Verfestigungseffekte in Metallen bei nicht-

proportionaler Belastung. Dieses Modell basiert auf dem Modell von Teodosiu and Hu (1995, 1998). In dem Modell von Teodosiu and Hu (1995, 1998) wird eine symmetrische vierstufige tensorwertige innere Variable  $S$  mit Spannungsdimension eingeführt, die den Einfluss der orientierungsabhängigen Stärke der Versetzungswände auf das Materialverhalten beschreibt. Um  $S$  zu beschreiben, werden Entwicklungsgleichungen für die Projektionen von  $S$  in Richtung des plastischen Fließens  $s^d$  und senkrecht dazu  $S^\ell$  eingeführt. Mehrere Ansätze wurden in der Literatur vorgeschlagen, die beschreiben, wie die Entwicklungsgleichungen für  $s^d$  und  $S^\ell$  integriert werden sollen, um  $S$  zu gewinnen. Sie führen allerdings zu verschiedenen Ergebnissen. Das alternative Modell für gerichtete Verfestigung, das in dieser Arbeit vorgeschlagen wird, basiert auf einer Entwicklungsgleichung für  $S$  selbst. Genauso wie das Modell von Teodosiu and Hu (1995, 1998) beschreibt auch die alternative Formulierung die Effekte der Verfestigungsstagnation nach einer Belastungsumkehr sowie der Querverfestigung nach einem orthogonalen Belastungsrichtungswechsel. Die beiden Modelle unterscheiden sich hinsichtlich deren Verhaltens in einfacher Scherung sowie in Prozessen mit kontinuierlichen Dehnungspfadänderungen. Außerdem wurde das aktuelle Modell um den Effekt des plastischen Spins erweitert.

Im vierten Kapitel werden die Ergebnisse der Kapiteln 2 und 3 zu der Simulation mehrerer Blechumformprozesse samt der Rückfederung angewendet. Das erste Beispiel ist der sogenannte Streifenzugbiegeversuch, der zur Untersuchung des Einflusses der kinematischen Verfestigung sowie der Verfestigungsstagnation auf Umformprozesse benutzt wurde. Als nächstes wird der sogenannte Ringzerlegungsversuch, der auf dem Zerlegen eines zylindrischen tiefgezogenen Napfes basiert, simuliert. Angesichts der komplexen nichtproportionalen Belastung ist dieser Test besonders gut zur Untersuchung des Einflusses von Querverfestigung auf die Eigenspannungen und die Rückfederung geeignet. Außerdem betrachten wir den Tiefziehprozess eines quadratischen Blechkastens. Die Simulationsergebnisse des Streifenzugbiegeversuchs am hochfesten Stahl DP600 wurden benutzt, um die Bedeutung der Verfestigungsstagnation auf die Rückfederung zu zeigen. Unter Benutzung des weichen einen ausgeprägten Querverfestigungseffekt aufweisenden Tiefziehstahls DC06 konnte man mit Hilfe des Ringzerlegungsversuches zeigen, wie wichtig die gerichtete Verfestigung bei Prozessen mit komplexen, insbesondere orthogonalen Belastungsrichtungsänderungen für die Simulation von Eigenspannungen und Rückfederung ist. Im Falle des Blechkastens wurde gezeigt, dass in Bereichen, wo die Lastumkehr dominiert, das aktuelle Modell niedrigere Eigenspannungen infolge der Verfestigungsstagnation vorhersagt, während in Bereichen, wo der Deformationspfad einen nahezu orthogonalen Wechsel vollzieht, höhere Eigenspannungen infolge der Querverfestigung.



# Chapter 1

## On the modeling and simulation of induced anisotropy in polycrystalline metals with application to springback\*

**Abstract** – The presence of initial, and the development of induced, anisotropic elastic and inelastic material behaviour in polycrystalline metals, can be traced back to the influence of texture and dislocation substructural development on this behaviour. As it turns out, via homogenization or other means, one can formulate effective models for such structure and its effect on the macroscopic material behaviour with the help of the concept of evolving structure tensors. From the constitutive point of view, these quantities determine the material symmetry properties. Most importantly, all dependent constitutive fields (e.g., stress) are by definition isotropic functions of the independent constitutive variables which include these evolving structure tensors. The evolution of these during loading results in an evolution of the anisotropy of the material. From an algorithmic point of view, the current approach leads to constitutive models which are quite amenable to numerical implementation. To demonstrate the applicability of the resulting constitutive formulation, we apply it to the case of metal plasticity with combined hardening involving both deformation- and permanently-induced anisotropy. Comparison of simulation results based on this model for the bending-tension of DP600 steel sheet-metal strips with corresponding experimental ones show good agreement.

### 1.1 Introduction

Initial and induced, anisotropic elastic and inelastic material behaviour in polycrystalline metals can often be traced back to concurrent texture and dislocation substructural evolution in the material. Indeed, many kinds of materials possess a microstructure which results in a macroscopic anisotropic material response. Classical examples of such behaviour include single crystals and composites in which the anisotropy can be considered to be fixed. A major simplification in the formulation of phenomenological material models for such anisotropy was achieved with the introduction of so-called structure tensors by Boehler (1979) (see also, e.g., Liu, 1982; Svendsen, 1994; Zhang and Rychlewski, 1990). To be precise, the term "structure tensor" is used here to designate quantities with respect to which the dependent constitutive fields can be represented as being *isotropic* functions of their arguments, *i.e.*, with respect to some local configuration<sup>1</sup>. In order to model induced elastic and inelastic anisotropic material behaviour, such an approach has been extended more recently, e.g., in the framework of the plastic spin (Dafalias, 1998), or in a thermodynamical setting (Reese and Svendsen, 2003; Svendsen, 1998, 2001) to

---

\*Wang et al. (2005b)

<sup>1</sup>In the phenomenological terminology of Truesdell & Noll (Truesdell and Noll, 1992, §32), such a configuration is referred to being "undistorted".

the modeling of internal variables having to do with processes such as kinematic hardening or texture development. In particular, evolution of the internal variables modeled in this fashion leads in general to induced orthotropic or yet more complex elastic and inelastic anisotropic material behaviour. The purpose of the current work is to show that, among other things, this approach results in further simplifications of the modeling of induced anisotropic elastic and inelastic material behaviour. In particular, in the current thermodynamic setting, the modeling of the internal variables as such tensors in the free energy *with respect to the so-called intermediate configuration* results in a six-dimensional flow rule. This is complementary to a previous result in Svendsen (2001) showing that the stress measure thermodynamically conjugate to the plastic “velocity gradient” is symmetric when the free energy is an isotropic function of its arguments, and in particular of any tensor-valued internal variables. As shown there, this result is completely general, *i.e.*, does not depend on any further assumptions about the form of the free energy. Beyond this, various applications of this approach are developed and discussed here, demonstrating that it can be applied to such diverse materials as metals and polymers. In recent work, Dettmer and Reese (2004) have compared such models with other approaches to the modeling of non-linear kinematic hardening in the context of large deformation.

The paper begins with a summary of the basic constitutive framework utilized in the sequel (§2). The corresponding formulation is carried out in a thermodynamic setting and in the context of the dissipation inequality. In particular, this is based on the modeling of the local inelastic deformation as a material isomorphism, as well as that of the internal variables as structure tensors (§3). Even in the case of a single scalar-valued, and a single symmetric-tensor-valued, internal variable, the approach is able to account for an evolving effective isotropic to general orthotropic elastic and inelastic material behaviour. Finally, to exemplify the approach, it is applied in the last part of the work (§4) to formulate a model for metal plasticity with combined hardening. This model is then applied to the simulation of DP600 steel sheet metal strips subject to tension and bending.

## 1.2 Basic framework

As stated in the introduction, the approach pursued here is based on a thermodynamic approach to the formulation of inelastic material behaviour (*e.g.*, Reese and Svendsen, 2003; Svendsen, 2001). For simplicity, attention is restricted here to the isothermal and quasi-static special case of this approach. In this case, the “external” mechanical state of any given material point is determined at any time by the values of the deformation gradient  $\mathbf{F}$ . Analogously, the “internal” mechanical state of any material point at any time is determined by the values of a set  $\mathbf{e} := (\boldsymbol{\epsilon}, \mathbf{F}_p)$  of internal variables, with  $\boldsymbol{\epsilon} := (\boldsymbol{\epsilon}_1, \dots, \boldsymbol{\epsilon}_n)$ . In particular,  $\mathbf{F}_p$  represents the local inelastic deformation. Except for  $\mathbf{F}_p$ , the  $\mathbf{e}$  are all modeled here as *referential* quantities, *i.e.*, quantities defined with respect to the above-mentioned arbitrary reference configuration of the material in question.

In the current isothermal context, the basic dependent constitutive fields of interest are the second Piola-Kirchhoff stress  $\mathbf{S}$ , the free energy density  $\psi$ , and the rates  $\dot{\boldsymbol{\epsilon}}$ . In the context of generally rate-dependent or rate-sensitive inelastic material behaviour, the thermodynamic

analysis Svendsen (2001), one obtains the reduced form

$$\psi = \psi(\mathbf{C}, \mathbf{e}) \quad (1.1)$$

for the isothermal free energy density  $\psi$ . Here,  $\mathbf{C} := \mathbf{F}^T \mathbf{F}$  represents as usual the right Cauchy-Green deformation. Further, one obtains the hyperelastic form

$$\mathbf{S} = 2 \psi_{,\mathbf{C}} \quad (1.2)$$

for the second Piola-Kirchhoff stress, as well as the residual form

$$\delta = \mathbf{s} \cdot \dot{\mathbf{e}} \quad (1.3)$$

for the dissipation-rate density, where

$$\mathbf{s} := - \psi_{,\mathbf{e}} \quad (1.4)$$

represents the thermodynamic force conjugate to  $\mathbf{e}$ . Now, in general, one might expect the inelastic rates  $\dot{\mathbf{e}}$  to remain bounded during a loading process. One possible measure of such boundedness can be based on the convex set

$$C_\phi(\mathbf{s}) := \{\mathbf{s}_* \mid \phi(\mathbf{s}_*) \leq \phi(\mathbf{s})\} \quad (1.5)$$

of all thermodynamic forces bounded by  $\mathbf{s}$  as measured by an inelastic potential

$$\phi = \phi(\mathbf{s}) \quad (1.6)$$

(*e.g.*, Edelen, 1973; Han and Reddy, 1999; Šilhavý, 1997) convex in  $\mathbf{s}$ . Indeed, one could assume that the inelastic rates attainable for a given thermodynamic force  $\mathbf{s}$  are bounded by the normal cone

$$N_\phi(\mathbf{s}) := \{\dot{\mathbf{e}}_* \mid \mathbf{s}_* \cdot \dot{\mathbf{e}}_* \leq \mathbf{s} \cdot \dot{\mathbf{e}}_* \quad \forall \mathbf{s}_* \in C_\phi(\mathbf{s})\} \quad (1.7)$$

to  $C_\phi(\mathbf{s})$ . Assuming in this context that  $\mathbf{s}$  represents an interior point of the domain of  $\phi$  such that  $\phi(\mathbf{s}) > 0$ , then  $\dot{\mathbf{e}} \in N_\phi(\mathbf{s})$  iff there exists a  $\gamma \geq 0$  such that<sup>2</sup>

$$\dot{\mathbf{e}} = \gamma \phi_{,\mathbf{s}} \quad (1.8)$$

holds (*e.g.*, Han and Reddy, 1999; Rockafellar, 1973). In this case,

$$\delta = \gamma \mathbf{s} \cdot \phi_{,\mathbf{s}} \geq \gamma \phi \geq 0 \quad (1.9)$$

from (1.3), the second form following from the convexity of  $\phi$  in  $\mathbf{s}$ . On this basis, the Coleman-Noll dissipation principle (*e.g.*, Coleman and Gurtin, 1967) is satisfied *sufficiently* here.

In particular, in the rate-independent special case,  $\gamma$  corresponds to the standard plastic multiplier. In general, however, the current formulation pertains to so-called rate-dependent material behaviour. Technically speaking, rate-independent behaviour is realized in the current formulation as a special case when the dissipation potential thermodynamically-conjugate to  $\phi$  is positive homogeneous of order one in  $\mathbf{s}$ . Even in this case, note that  $\phi$  does not reduce to a yield function in general. Indeed, in order to formulate rate-independent thermodynamic models for non-linear kinematic hardening, it is necessary to deviate from standard associated elastoplasticity here (*e.g.*, in the small deformation context, Lemaitre and Chaboche, 1990).

---

<sup>2</sup>In general, the derivative here does not exist for all generalized stress states, in which case it should be replaced by the subdifferential (*e.g.*, Han and Reddy, 1999; Šilhavý, 1997).

### 1.3 Internal variables as structure tensors

Recall now that  $e = (\epsilon, \mathbf{F}_P)$ . In this work, inelastic processes represented by  $\mathbf{F}_P$  are assumed to not affect the form of the dependence of  $\psi$  on  $\mathbf{C}$  and the  $e$ . In this case,  $\mathbf{F}_P$  represents a so-called material isomorphism for  $\psi$  (e.g., Bertram, 1993; Svendsen, 1998; Wang and Bloom, 1974). As shown in previous work (e.g., Svendsen, 1998, 2001), this will be the case when there exists a reduced form  $\psi_I$  of  $\psi$  such that

$$\psi(\mathbf{C}, \epsilon, \mathbf{F}_P) = \psi_I(\mathbf{F}_{P*} \mathbf{C}, \mathbf{F}_{P*} \epsilon) = \psi_I(\mathbf{C}_E, \epsilon_I) \quad (1.10)$$

holds. Here,  $\mathbf{C}_E := \mathbf{F}_{P*} \mathbf{C} = \mathbf{F}_P^{-T} \mathbf{C} \mathbf{F}_P^{-1}$  represents the elastic right Cauchy-Green deformation tensor, and  $\epsilon_I := \mathbf{F}_{P*} \epsilon$  the push-forward of  $\epsilon$  by  $\mathbf{F}_P$  to the intermediate configuration. The particular form of this latter pull-back depends on the nature of the  $\epsilon$ . Examples of this will be given in the following sections. From an alternative point of view, (1.10) follows from the idea that only a "part" of the deformation processes represented by  $\mathbf{C}$  and the  $\epsilon$  are responsible for energy storage in the material during deformation, *i.e.*, "parts"  $\mathbf{F}_{P*} \mathbf{C}$  and  $\mathbf{F}_{P*} \epsilon$ , respectively. On the basis of (1.10), one obtains

$$\delta = -\psi_{,\epsilon} \cdot \dot{\epsilon} - \psi_{,\mathbf{F}_P} \cdot \dot{\mathbf{F}}_P = \boldsymbol{\sigma}_I \cdot \epsilon_I^* + \boldsymbol{\Sigma}_I \cdot \mathbf{L}_P \quad (1.11)$$

from (1.3) for the reduced dissipation-rate density. Here,

$$\begin{aligned} \boldsymbol{\sigma}_I &:= -\psi_{I,\epsilon_I}, \\ \boldsymbol{\Sigma}_I &:= 2 \mathbf{C}_E \psi_{I,\mathbf{C}_E} - (\epsilon_{I,\mathbf{F}_P})^T [\psi_{I,\epsilon_I}] \mathbf{F}_P^T, \end{aligned} \quad (1.12)$$

represent thermodynamic forces in the intermediate configuration driving the evolution of  $\epsilon$  and  $\mathbf{F}_P$ , respectively, with

$$\begin{aligned} \epsilon_I^* &:= \mathbf{F}_{P*} \dot{\epsilon}, \\ \mathbf{L}_P &:= \mathbf{F}_{P*} \dot{\mathbf{F}}_P = \dot{\mathbf{F}}_P \mathbf{F}_P^{-1}. \end{aligned} \quad (1.13)$$

Note that the effective stress  $\boldsymbol{\Sigma}_I$  in (1.12)<sub>2</sub> conjugate to  $\mathbf{L}_P$  is determined by the difference of the Mandel stress  $2 \mathbf{C}_E \psi_{I,\mathbf{C}_E}$  (e.g., Mandel, 1974) and the back stress

$$\mathbf{X}_I := (\epsilon_{I,\mathbf{F}_P})^T [\psi_{I,\epsilon_I}] \mathbf{F}_P^T. \quad (1.14)$$

In the context of (1.11), analogous to the reduced form (1.10) of the free energy, we work with that

$$\phi = \phi_I(\boldsymbol{\Sigma}_I, \boldsymbol{\sigma}_I) \quad (1.15)$$

for the inelastic potential  $\phi$  from (1.6) relative to the intermediate configuration in terms of  $\boldsymbol{\Sigma}_I$  and  $\boldsymbol{\sigma}_I$ . On the basis of (1.3), (1.8) and (1.11), we have

$$\begin{aligned} \epsilon_I^* &= \gamma \phi_{I,\boldsymbol{\sigma}_I}, \\ \mathbf{L}_P &= \gamma \phi_{I,\boldsymbol{\Sigma}_I}. \end{aligned} \quad (1.16)$$

These constitute the basic relations of the model with respect to the intermediate configuration. With the help of the alternative form

$$\delta = \boldsymbol{\sigma} \cdot \dot{\epsilon} + \boldsymbol{\Sigma} \cdot \mathbf{M}_P = \boldsymbol{\sigma}_C \cdot \epsilon_C^* + \boldsymbol{\Sigma}_C \cdot \mathbf{M}_C \quad (1.17)$$

of  $\delta$ , these relations can also be formulated with respect to the reference or current configuration. Here,

$$\begin{aligned}\boldsymbol{\sigma} &:= (\boldsymbol{\epsilon}_I, \boldsymbol{\epsilon})^T \boldsymbol{\sigma}_I = -(\boldsymbol{\epsilon}_I, \boldsymbol{\epsilon})^T \psi_{I, \boldsymbol{\epsilon}_I}, \\ \boldsymbol{\Sigma} &:= \mathbf{F}_P^T \boldsymbol{\Sigma}_I \mathbf{F}_P^{-T} = \mathbf{C} \mathbf{S} - \mathbf{X}_R,\end{aligned}\quad (1.18)$$

are the referential forms, and

$$\begin{aligned}\boldsymbol{\sigma}_C &:= (\mathbf{F}_E^{-T})_* \boldsymbol{\sigma}_I = -(\mathbf{F}_E^{-T})_* \psi_{I, \boldsymbol{\epsilon}_I}, \\ \boldsymbol{\Sigma}_C &:= \mathbf{F}_E^{-T} \boldsymbol{\Sigma}_I \mathbf{F}_E^T = \mathbf{K} - \mathbf{X}_C,\end{aligned}\quad (1.19)$$

the current forms, of  $\boldsymbol{\sigma}_I$  and  $\boldsymbol{\Sigma}_I$ , respectively, with

$$\begin{aligned}\mathbf{S} &= 2 \mathbf{F}_P^{-1} \psi_{I, C_E} \mathbf{F}_P^{-T}, \\ \mathbf{K} &= 2 \mathbf{F}_E \psi_{I, C_E} \mathbf{F}_E^T,\end{aligned}\quad (1.20)$$

the second Piola-Kirchhoff stress and the Kirchhoff stress, respectively, the former via (1.2), and

$$\begin{aligned}\mathbf{X}_R &:= \mathbf{F}_P^T (\boldsymbol{\epsilon}_I, \mathbf{F}_P)^T [\psi_{I, \boldsymbol{\epsilon}_I}], \\ \mathbf{X}_C &:= \mathbf{F}_E^{-T} (\boldsymbol{\epsilon}_I, \mathbf{F}_P)^T [\psi_{I, \boldsymbol{\epsilon}_I}] \mathbf{F}^T,\end{aligned}\quad (1.21)$$

the referential and current forms of the back stress. In addition,

$$\mathbf{M}_P := \mathbf{F}_P^* \mathbf{L}_P = \mathbf{F}_P^{-1} \mathbf{L}_P \mathbf{F}_P \quad (1.22)$$

represents the referential form of  $\mathbf{L}_P$ . Further,

$$\begin{aligned}\boldsymbol{\epsilon}_C^* &:= \mathbf{F}_* \dot{\boldsymbol{\epsilon}}, \\ \mathbf{M}_C &:= \mathbf{F}_{E*} \mathbf{L}_P = \mathbf{F}_E \mathbf{L}_P \mathbf{F}_E^{-1},\end{aligned}\quad (1.23)$$

are the corresponding forms with respect to the current configuration. These transformations of the stress measures into the current configuration facilitate the formulation of the material model with respect to this configuration.

A second major simplification of interest here arises when the free energy in the reduced form (1.10), as well as the inelastic potential  $\phi_I$  in the form (1.15), can be modeled as isotropic functions of their arguments. As discussed elsewhere (Svendsen, 2001), in this case the internal variables  $\boldsymbol{\epsilon}_I$  and  $\boldsymbol{\sigma}_I$  with respect to the intermediate configuration play (at least formally) the role of so-called structure tensors. Consequences of this include the fact that both  $\boldsymbol{\Sigma}_I$  as given by (1.12)<sub>2</sub> and the corresponding Eshelby-like stress are symmetric with respect to the Euclidean metric. On this basis,  $\psi_I$  and  $\phi_I$  reduce further to

$$\begin{aligned}\psi_I(\mathbf{C}_E, \boldsymbol{\epsilon}_I) &= \psi_I(\mathbf{G}_P^* \mathbf{C}, \mathbf{G}_P^* \boldsymbol{\epsilon}), \\ \phi_I(\boldsymbol{\Sigma}_I, \boldsymbol{\sigma}_I) &= \phi_I(\mathbf{G}_P^* \boldsymbol{\Sigma}, \mathbf{G}_P^* \boldsymbol{\sigma}),\end{aligned}\quad (1.24)$$

respectively, via the polar decomposition  $\mathbf{F}_P = \mathbf{R}_P \mathbf{U}_P$  of  $\mathbf{U}_P$ . Here,

$$\mathbf{G}_P := \mathbf{C}_P^{-1} = \mathbf{U}_P^{-2} = \mathbf{F}_P^{-1} \mathbf{F}_P^{-T} \quad (1.25)$$

is a symmetric, positive-definite-tensor-valued *referential* internal variable with evolution relation

$$\dot{\mathbf{G}}_P = -2 \mathbf{F}_P^{-1} \mathbf{D}_P \mathbf{F}_P^{-T} = -\mathbf{M}_P \mathbf{G}_P - \mathbf{G}_P \mathbf{M}_P^T \quad (1.26)$$

following from (1.13)<sub>2</sub> and (1.22)<sub>1</sub>. From (1.24)<sub>1</sub>, one obtains the referential forms

$$\begin{aligned} \psi_R(\mathbf{C}, \boldsymbol{\epsilon}, \mathbf{G}_P) &:= \psi_I(\mathbf{G}_P^* \mathbf{C}, \mathbf{G}_P^* \boldsymbol{\epsilon}), \\ \phi_R(\boldsymbol{\Sigma}, \boldsymbol{\sigma}, \mathbf{G}_P) &:= \phi_I(\mathbf{G}_P^* \boldsymbol{\Sigma}, \mathbf{G}_P^* \boldsymbol{\sigma}), \end{aligned} \quad (1.27)$$

for the free energy and inelastic potential, respectively, determined by the isotropic forms of  $\psi_I$  and  $\phi_I$ , respectively. Again, we emphasize that  $\psi_R$  and  $\phi_R$  are not arbitrary, but rather follow from the isotropic forms of  $\psi_I$  and  $\phi_I$ , respectively. In particular, the reduction (1.24)<sub>1</sub> induces in turn that

$$\boldsymbol{\Sigma} = 2 \psi_{R, \mathbf{G}_P} \mathbf{G}_P \quad (1.28)$$

for the thermodynamic conjugate to  $\mathbf{M}_P$  in terms of the dependence of  $\psi_R$  on  $\mathbf{G}_P$  via (1.18)<sub>2</sub>. As in the reduced form (1.27)<sub>1</sub> of the free energy, note that the form (1.26) of the evolution relation for  $\mathbf{G}_P$ , as well as that (1.11) of the residual dissipation rate density, are explicitly independent of  $\mathbf{F}_P$ . For this class of material models, then, one can in effect reduce the dependence of the model on the nine-dimensional quantity  $\mathbf{F}_P$  to one on the six-dimensional quantity  $\mathbf{G}_P$ . Lastly, note that the isotropy of  $\psi_I$  and  $\phi_I$  leading to the reductions (1.24) also implies the forms

$$\begin{aligned} \psi_C(\mathbf{B}_E, \boldsymbol{\epsilon}_C) &:= \psi_I(\mathbf{B}_E^* \mathbf{I}, \mathbf{B}_E^* \boldsymbol{\epsilon}_C), \\ \phi_C(\mathbf{B}_E, \boldsymbol{\Sigma}_C, \boldsymbol{\sigma}_C) &:= \phi_I(\mathbf{B}_E^* \boldsymbol{\Sigma}_C, \mathbf{B}_E^* \boldsymbol{\sigma}_C), \end{aligned} \quad (1.29)$$

of the free energy and inelastic potential with respect to the current configuration in terms of the left elastic Cauchy-Green deformation

$$\mathbf{B}_E := \mathbf{F}_E \mathbf{F}_E^T = \mathbf{F} \mathbf{G}_P \mathbf{F}^T \quad (1.30)$$

Analogous to (1.26), we have

$$\dot{\mathbf{B}}_E^* := \mathbf{F} \dot{\mathbf{G}}_P \mathbf{F}^T = -\mathbf{M}_C \mathbf{B}_E - \mathbf{B}_E \mathbf{M}_C^T \quad (1.31)$$

via (1.22)<sub>2</sub>. Likewise, analogous to (1.28) is the form

$$\boldsymbol{\Sigma}_C = 2 \psi_{C, \mathbf{B}_E} \mathbf{B}_E \quad (1.32)$$

for  $\boldsymbol{\Sigma}_C$  via (1.19)<sub>2</sub>, again with respect to the current configuration.

This completes the discussion of the general results required for the sequel. Now we turn to the application of the current approach to the cases of induced anisotropy in metals and in polymer membranes.

## 1.4 Application to metal inelasticity with hardening

To examine some of the aspects and consequences of the general formulation outlined in the last section in more detail, consider its application to the formulation of a model for rate-independent metal plasticity including isotropic and non-linear kinematic hardening. More general models involving elastic anisotropy due to texture development, as well as flow anisotropy

resulting from the development of persistent dislocation structures (*e.g.*, Li et al., 2003), are developed and discussed in Svendsen (2001). For simplicity, attention is restricted here to the case of non-linear isotropic and kinematic hardening, the latter including the effects of dynamic recovery. In particular, this latter effect is represented in the current context with the help of a referential symmetric second-order tensor  $\mathbf{G}_H$  formally analogous to  $\mathbf{G}_P$ . As such, we have  $\epsilon = (\mathbf{G}_H, \epsilon)$  in this case, where  $\epsilon$  represents the equivalent accumulated plastic strain. Analogous to that  $\mathbf{C}_E = \mathbf{F}_P^{-T} \mathbf{C} \mathbf{F}_P^{-1}$  of  $\mathbf{C}$ , the push-forward  $\mathbf{G}_{HI} = \mathbf{F}_{P*} \mathbf{G}_H = \mathbf{F}_P \mathbf{G}_H \mathbf{F}_P^T$  of  $\mathbf{G}_H$  to the intermediate configuration is interpreted as a measure of local internal deformation resulting in energy storage in the material. Let  $\sigma_I = (\mathbf{J}_I, \varsigma)$  represent the thermodynamic conjugates to  $\epsilon_I$ , with

$$\begin{aligned} \mathbf{J}_I &= -\psi_{I, \mathbf{G}_{HI}}, \\ \varsigma &= -\psi_{I, \epsilon}, \end{aligned} \quad (1.33)$$

via (1.4). Assuming now that the Green-strain-like strain measures

$$\begin{aligned} \mathbf{E}_E &:= \frac{1}{2}(\mathbf{C}_E - \mathbf{I}), \\ \mathbf{E}_H &:= \frac{1}{2}(\mathbf{G}_{HI} - \mathbf{I}), \end{aligned} \quad (1.34)$$

determined by  $\mathbf{C}_E$  and  $\mathbf{G}_{HI}$ , respectively, are small, a model for combined hardening behaviour with respect to the intermediate configuration can be based on the special isotropic ‘‘quadratic’’ forms

$$\begin{aligned} \psi_I(\mathbf{C}_E, \mathbf{G}_{HI}, \epsilon) &= \frac{1}{2} \lambda (\mathbf{I} \cdot \mathbf{E}_E)^2 + \mu \mathbf{E}_E \cdot \mathbf{E}_E + \frac{1}{2} c \mathbf{E}_H \cdot \mathbf{E}_H + \psi_H(\epsilon), \\ \phi_I(\boldsymbol{\Sigma}_I, \mathbf{J}_I, \varsigma) &= y_I(\boldsymbol{\Sigma}_I, \varsigma) + \frac{b}{2c} \mathbf{I} \cdot \mathbf{J}_I^2, \end{aligned} \quad (1.35)$$

of the free energy density and inelastic potential, respectively, with respect to the intermediate configuration, where

$$y_I(\boldsymbol{\Sigma}_I, \varsigma) = \sqrt{\frac{3}{2} \text{dev}(\boldsymbol{\Sigma}_I) \cdot \text{dev}(\boldsymbol{\Sigma}_I)} + \varsigma - \sigma_{Y0} \quad (1.36)$$

represents the yield function, with  $\text{dev}(\boldsymbol{\Sigma}_I) := \boldsymbol{\Sigma}_I - \frac{1}{3}(\mathbf{I} \cdot \boldsymbol{\Sigma}_I) \mathbf{I}$  the deviatoric part of  $\boldsymbol{\Sigma}_I$ . Here,  $\lambda$  and  $\mu$  represent Lamé’s constants. Further,  $c$  and  $b$  are kinematic hardening parameters controlling deformation-induced hardening and dynamic recovery, respectively. In addition,  $\sigma_{Y0} - \varsigma$  represents the yield stress, and  $\sigma_{Y0}$  the initial yield stress. Note that (1.35)<sub>1</sub> results in the forms

$$\begin{aligned} \boldsymbol{\Sigma}_I &= \lambda (\mathbf{I} \cdot \mathbf{E}_E) \mathbf{I} + 2\mu \mathbf{E}_E - c \mathbf{E}_H + O(2), \\ \mathbf{J}_I &= -\frac{1}{2} c \mathbf{E}_H, \\ \varsigma &= -\psi_{H, \epsilon}, \end{aligned} \quad (1.37)$$

for the stress-like internal variables to first order in  $\mathbf{E}_E$  and  $\mathbf{E}_H$ . Complementary to these are the forms<sup>3</sup>

$$\begin{aligned}\dot{\mathbf{F}}_P \mathbf{F}_P^{-1} &= \gamma \phi_{I, \Sigma_I} = \gamma \sqrt{\frac{3}{2}} \frac{\text{dev}(\Sigma_I)}{\sqrt{\text{dev}(\Sigma_I) \cdot \text{dev}(\Sigma_I)}}, \\ \mathbf{F}_P \dot{\mathbf{G}}_H \mathbf{F}_P^T &= \gamma \phi_{I, \mathbf{J}_I} = -\frac{1}{2} \gamma b \mathbf{E}_H, \\ \dot{\varepsilon} &= \gamma \phi_{I, \varsigma} = \gamma,\end{aligned}\tag{1.38}$$

for the corresponding evolution relations via (1.8) and (1.13). As mentioned in §2, the inelastic potential  $\phi_I$  is not a yield function here. On the other hand, being a yield function,  $y_I$  does bound the  $\Sigma_I$ -states from above. And  $\phi_I$  is assumed to bound the  $(\Sigma_I, \mathbf{J}_I)$ -states via the corresponding normal cone, as discussed in §2.

As in the case of finite-deformation elasticity, there exist a number of possible finite forms for the free energy and inelastic potential which reduce in the case of small elastic strain to the same model relations (e.g., Svendsen, 2001). In this case, we have

$$\begin{aligned}\mathbf{F}_E &\approx \mathbf{R}_E, \\ \mathbf{V}_E &\approx \mathbf{I} + \ln \mathbf{V}_E.\end{aligned}\tag{1.39}$$

In addition, this approximation results in the simplified forms

$$\begin{aligned}\mathbf{B}_E &= \mathbf{F} \mathbf{G}_P \mathbf{F}^T = \exp(2 \ln \mathbf{V}_E) = \mathbf{I} + 2 \ln \mathbf{V}_E + O(2), \\ \mathbf{B}_H &= \mathbf{F} \mathbf{G}_H \mathbf{F}^T = \exp(2 \ln \mathbf{V}_H) = \mathbf{I} + 2 \ln \mathbf{V}_H + O(2),\end{aligned}\tag{1.40}$$

for  $\mathbf{B}_E$  and  $\mathbf{B}_H$  in terms of corresponding logarithmic strain measures  $\ln \mathbf{V}_E$  and  $\ln \mathbf{V}_H$ , respectively. Combining (1.39) and (1.40), then, results in the reduced forms

$$\begin{aligned}\mathbf{E}_E &= \frac{1}{2} \mathbf{F}_E^T (\mathbf{I} - \mathbf{B}_E^{-1}) \mathbf{F}_E = \mathbf{R}_E^T \ln \mathbf{V}_E \mathbf{R}_E + O(2), \\ \mathbf{E}_H &= \frac{1}{2} \mathbf{F}_E^{-1} (\mathbf{B}_H - \mathbf{B}_E) \mathbf{F}_E^{-T} = \mathbf{R}_E^T (\ln \mathbf{V}_H - \ln \mathbf{V}_E) \mathbf{R}_E + O(2),\end{aligned}\tag{1.41}$$

for the strain measures  $\mathbf{E}_E$  and  $\mathbf{E}_H$  from (1.34). In turn, these imply

$$\begin{aligned}\psi_C &= \frac{1}{2} \lambda (\mathbf{I} \cdot \ln \mathbf{V}_E)^2 + \mu \ln \mathbf{V}_E \cdot \ln \mathbf{V}_E \\ &\quad + \frac{1}{2} c (\ln \mathbf{V}_H - \ln \mathbf{V}_E) \cdot (\ln \mathbf{V}_H - \ln \mathbf{V}_E) + \psi_H(\varepsilon), \\ y_C &= \sqrt{\frac{3}{2} \text{dev}(\Sigma_C) \cdot \text{dev}(\Sigma_C)} + \varsigma - \sigma_{Y0}, \\ \phi_C &= y_C + \frac{b}{2c} \mathbf{I} \cdot \mathbf{J}_C^2.\end{aligned}\tag{1.42}$$

from (1.35) for the free energy, inelastic potential and yield function with respect to the current configuration. From these, one obtains the reduced forms

$$\begin{aligned}\mathbf{K} &= \lambda (\mathbf{I} \cdot \ln \mathbf{V}_E) \mathbf{I} + 2\mu \ln \mathbf{V}_E, \\ \mathbf{J}_C &= -\frac{1}{2} c (\ln \mathbf{V}_H - \ln \mathbf{V}_E), \\ \mathbf{X}_C &= c (\ln \mathbf{V}_H - \ln \mathbf{V}_E), \\ \Sigma_C &= \psi_{C, \ln \mathbf{V}_E},\end{aligned}\tag{1.43}$$

---

<sup>3</sup>Because the von Mises form (1.36) of the yield function  $y$  is not differentiable at  $\Sigma_I = \mathbf{0}$ , the expression for  $M_P$  in (1.38)<sub>1</sub> must be generalized to the subdifferential form there. In any case, from a physical point of view, such values always belong to the elastic range of the material, for which  $\gamma = 0$ .



for the stresses in the case of small elastic strain. Lastly, exponential backward-Euler integration of the flow rule (1.38)<sub>1</sub> in the form (1.31) combined with (1.38)<sub>2,3</sub> yields the algorithmic backward-Euler system

$$\begin{aligned}\ln \mathbf{V}_{E \text{ tr}} &= \ln \mathbf{V}_E + \Delta\gamma \phi_{C, \Sigma_C}, \\ \ln \mathbf{V}_{H \text{ tr}} &= \ln \mathbf{V}_H + \Delta\gamma b (\ln \mathbf{V}_H - \ln \mathbf{V}_E), \\ \varepsilon_0 &= \varepsilon - \Delta\gamma,\end{aligned}\tag{1.44}$$

for the evolution relations in the context of small elastic strain, *i.e.*, (1.39) and (1.40), with  $\Delta\gamma := \gamma \Delta t$ . Here,

$$\begin{aligned}\ln \mathbf{V}_{E \text{ tr}} &:= \frac{1}{2} \ln(\mathbf{F} \mathbf{G}_{Pn} \mathbf{F}^T), \\ \ln \mathbf{V}_{H \text{ tr}} &:= \frac{1}{2} \ln(\mathbf{F} \mathbf{G}_{Hn} \mathbf{F}^T),\end{aligned}\tag{1.45}$$

represent the so-called trial values of  $\ln \mathbf{V}_E$  and  $\ln \mathbf{V}_H$ , respectively.

The above model has been implemented into a number of finite-element codes such as ABAQUS Standard via user-material and user-element interfaces such as UMAT and UEL, respectively. On this basis, it has been used to simulate a number of structures involving cyclic loading and strain-path changes resulting in kinematic hardening. For example, consider the case of combined tension-bending loading of a sheet metal strip. Such a test is used in particular in springback studies. In this test (*e.g.*, Kleiner et al., 2003, 2005), as shown in Figure 1.1, a straight sheet metal strip is bent approximately 90° around a roller at the top of the machine, clamped at both ends, and then pulled from left to right around the roller. The advantage of this type of strain-path-change test lies in the minimization of friction since the roller turns with the sheet metal strip as it is bent. The experimental results here are represented by the final profiles of the sheet metal samples after the test as shown in Figure 1.2 for the case of DP600 steel. The parameter identification was carried out by first fitting a purely isotropic hardening model to the uniaxial tension test data, then a purely kinematic model, and finally the combined model. This was carried out ignoring the mild initial flow anisotropy for sheet metal with a thickness of 1mm and 2mm, respectively. In particular, we worked with the Voce model

$$-\zeta = \psi_{H, \varepsilon} = (\sigma_{Y\infty} - \sigma_{Y0})(1 - e^{-\beta \varepsilon})\tag{1.46}$$

for isotropic hardening. On this basis, the parameter values obtained for the sheet metal DP600 in the case of combined hardening were  $\lambda = 109615.4$  MPa,  $\mu = 73076.9$  MPa,  $\sigma_{Y0} = 395$  MPa,  $\sigma_{Y\infty} = 615$  MPa,  $\beta = 10$ ,  $c = 1533.3$  MPa, and  $b = 10$ .

The simulation results are shown in Figures 1.3 and 1.4. Although the simulation results systematically overestimate the amount of springback determined in the experiments, the agreement is relatively good. In particular, such agreement of the experimental results with the initial combined-hardening simulation results for different sheet metal thicknesses may imply that springback is hardening-dominated for this material and under these conditions. As such, other effects having to do with the effect of dislocation substructure orientation and orientation evolution as a function of strain-path-type (*e.g.*, Li et al., 2003) may, like the initial flow anisotropy, be minimal. Further investigation of these issues represents work in progress.

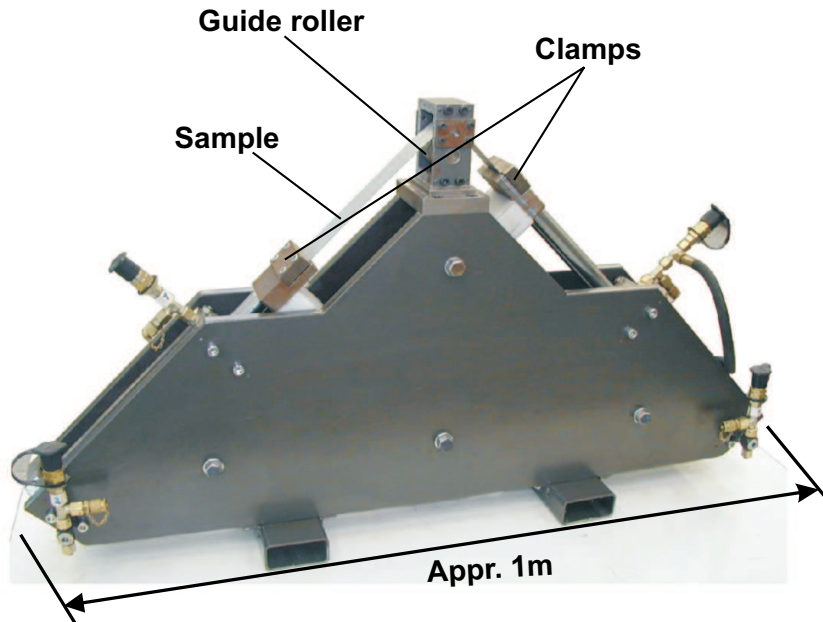


Figure 1.1: Bending-tension test machine and experimental set-up from Kleiner et al. (2005). In this test, the sheet metal strip is first pre-bent, clamped into the machine and stretched around the roller to the corresponding form. The test itself is then performed by pulling the strip from left to right via the clamps around the roller.



Figure 1.2: Specimens of the sheet metal DP600 with thicknesses of 1mm and 2mm after being subject to bending-tension shown in Figure 1.1 (Kleiner et al., 2005). After the bending-tension test is carried out, the specimens are released from the clamps and spring back into their final forms shown here.

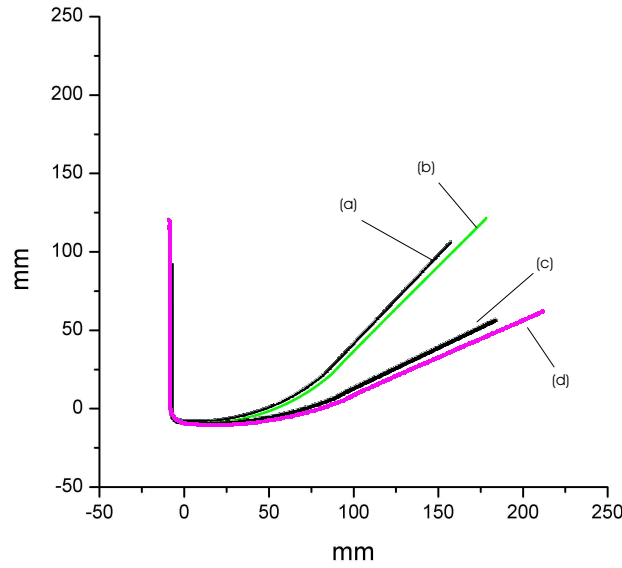


Figure 1.3: Comparison of experimental (Kleiner et al., 2005) and simulation results based on the current combined hardening model for the final form of DP600 sheet metal strips with a thickness of  $t = 1$  mm and  $t = 2$  mm subject to bending-tension around a roller of 5 mm radius: (a) simulation results for  $t = 1$  mm; (b) experimental result for  $t = 1$  mm; (c) result from the simulation with combined hardening for  $t = 2$  mm; (d) experimental result for  $t = 2$  mm.

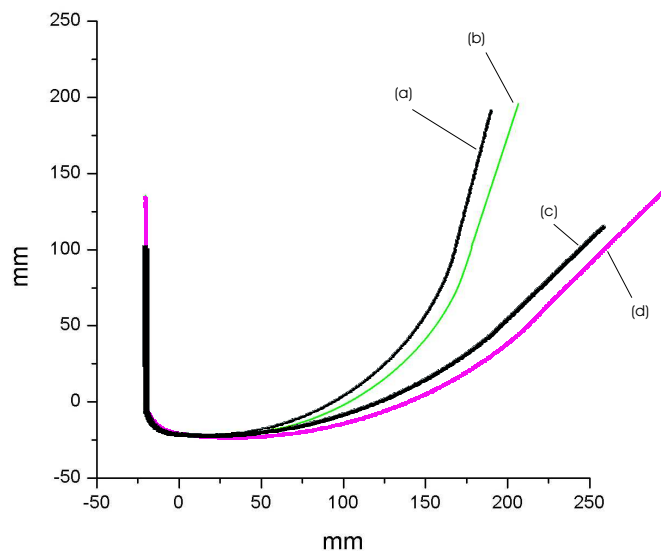


Figure 1.4: Comparison of experimental (Kleiner et al., 2005) and simulation results based on the current combined hardening model for the final form of DP600 sheet metal strips with a thickness of  $t = 1$  mm and  $t = 2$  mm subject to bending-tension around a roller of radius of 15 mm. Curves (a) to (d) have the same meaning as in Figure 1.3.



## Chapter 2

# On some numerical aspects of the simulation of sheet metal forming and springback\*

**Abstract** – Accurate simulation of forming and springback in sheet metal structures involves taking a number of processes into account. These include (i) complex loading path changes, (ii) contact and friction between the tool and work-piece, and (iii) the large deformations of very thin structures. In particular, (i) has a marked effect on the material, in particular the hardening, behavior, and has been investigated in more detail elsewhere (Wang et al., 2006a,d). In the current work, attention is focused on some numerical aspects involved in such simulations. In particular, we examine the roles played by the element formulation as well as the type of contact and friction modeling, in the simulation of sheet metal forming. The goal here is an optimal choice of algorithms, element types, contact and friction modeling, as well as numerical control parameters in such a way that an efficient, robust and convergent solution is achieved.

### 2.1 Introduction

The prediction of springback, defined as the difference between the shape of the work piece before and after unloading at the end of a forming process such as deep drawing, remains to this day one of the great challenges in the modeling and simulation of forming processes and one of the greatest problems for the manufacturer. The preferred use of high-strength materials such as dual phase steels in many modern manufacturing processes only aggravates the problem, *i.e.*, resulting in increased springback. With the rapid increase in computational power and the continuing development of numerical methods, the prediction of springback has progressed all the way from analytical approaches involving highly-idealized structures (*e.g.*, Baba and Tozawa, 1964; Chan, 1999; Huang and Gerdeen, 1994; Levy, 1984; Mickalich and Wenner, 1988; Queener and Angelis, 1968; Shaffer and House, 1955; Sudo et al., 1974; Ueda et al., 1981; Wenner, 1983; Yuen, 1900; Zhang and Lee, 1995) to numerical modeling and simulation in the context of, *e.g.*, the finite element method (FEM) (*e.g.*, Gelin and Picart, 1999; Lee et al., 1996; Makinouchi et al., 1993). Recent benchmark tests (*e.g.*, Chen et al., 2005; Strano, 2005; Wagoner and Li, 2005) demonstrate the state of the art in this regard. In addition, the increased availability of commercial programs for the simulation of forming processes (*e.g.*, LS-DYNA, PAM-STAMP, AutoForm, DYNAform, Stampack, *etc.*) has greatly facilitated the numerical simulation of springback (*e.g.*, Cao et al., 2005). In combination with experimental work, such approaches and programs have been utilized for predicting springback after simple forming operations, *e.g.*, cylindrical tool bending (*e.g.*, Martin and Tsang, 1966), V-die bending (*e.g.*, Asnafi, 2000; Huang and Leu, 1998; Tan et al., 1992), U-channel forming (*e.g.*, Huang and

---

\*Wang et al. (2006c)

Leu, 1995) and flanging (*e.g.*, Davies and Liu, 1984). Of course, springback simulations are only as good as the underlying forming simulation (*e.g.*, Lee and Yang, 1998; Mattiasson et al., 1995).

Given these developments, it becomes increasingly important to investigate and establish the possible influence of algorithmic and numerical aspects of the simulation on the corresponding results. These include the material model (*e.g.*, Geng and Wagoner, 2000; Haddag et al., 2005; Kleiner et al., 2005), the integration scheme (*e.g.*, Focellese et al., 1998; He and Wagoner, 1996; Lee and Yang, 1998; Narasimhan and Lovell, 1999), the element type (*e.g.*, Li et al., 1999), process conditions (*e.g.*, Meinders et al., 2005; Wagoner et al., 2002), and the solution procedure (*e.g.*, Hu and Du, 1999; Narasimhan and Lovell, 1999; Park et al., 1999). The purpose of the current work is the investigation of a number of these factors on the basis of the combined hardening model which has been implemented in the commercial finite element codes ABAQUS/Standard. To this end, relatively “simple” forming processes such as draw-bending or deep drawing of a cylindrical cup are utilized. The draw-bending test (*e.g.*, Carden et al., 2002; Kleiner et al., 2005; Wagoner et al., 2002; Wang, 2004) mimics closely the typical stamping deformation of the sheet metal as it is drawn, stretched, compressed, bent, and unbent over a die radius entering a matrix cavity. In particular, bending and unbending represent a loading path change of the load-reversal type in which isotropic and kinematic hardening are the principle hardening mechanisms. More complicated loading paths (*e.g.*, orthogonal) arise during processes such as deep drawing of closed structures. To show the effects of different numerical parameters, the ring-splitting process is used in this study. Ring-splitting after deep drawing involves a complex, non-proportional loading history and has been used by a number of authors (*e.g.*, Chen et al., 2005; Govindarajan et al., 2005; Rohleder et al., 2001) to investigate springback behavior. In this test, a deep-drawn cup is cut into a number of rings perpendicular to its symmetry axis and then the rings are split. Here, springback is characterized by the amount of ring opening after splitting.

The paper begins (§2) with a brief review of the material model used in the present work. In order to focus on numerical and other issues (*e.g.*, contact and friction), attention is restricted in this model for simplicity to isotropic von-Mises yielding as well as to isotropic and kinematic (*i.e.*, classical combined) hardening. The extension of this model to hardening stagnation, anisotropic flow and directional hardening effects has been carried out elsewhere (Wang et al., 2006a,d). Next, the algorithmic formulation and implementation of the material model is discussed (§3). After a brief review of the issues of element formulation (§4) as well as the contact and friction algorithm (§5), attention is focused on the investigation of the dependence of the solution on the number of elements, the element formulation, the number of integration points, as well as on contact and friction modeling (§6). Some additional physical aspects of the simulation (*e.g.*, boundary conditions) are also investigated (§7). Finally, the work ends with a brief summary and conclusions (§8).

## 2.2 Summary of material model

Standard so-called “combined” hardening models based on isotropic and kinematic mechanisms (*e.g.*, Chun et al., 2002) represent perhaps those most widely-used model to simulate

metal forming processes and springback. Such models are intended to represent the hardening behavior particularly during cyclic loading or during a strain-path reversal. For more complex loading histories, additional hardening mechanisms resulting in directional hardening effects generally need to be taken into account (Teodosiu and Hu, 1998; Wang et al., 2006a,d). Since we are focusing here, however, on numerical issues, attention is restricted for simplicity to combined hardening.

The incremental model to be summarized in what follows is derived assuming inelastic multiplicative decomposition, plastic incompressibility, and small elastic strain. As usual, in the incremental setting, the evolution of all tensor-valued internal variables is defined for reasons of material frame indifference with respect to a local configuration rotating relative to the current configuration. In the current model, this is identified with the rotation  $\mathbf{R}_E$  of the intermediate configuration with respect to the current configuration, with evolution equation

$$\dot{\mathbf{R}}_E = \mathbf{W}\mathbf{R}_E - \mathbf{R}_E\mathbf{W}_P \quad (2.1)$$

determined by the continuum  $\mathbf{W} = \text{skw}(\mathbf{L})$  and plastic  $\mathbf{W}_P$  spins,  $\mathbf{L} = \dot{\mathbf{F}}\mathbf{F}^{-1}$  being the velocity gradient as usual. On this basis, the elastic behavior of the model is based on the incremental hypoelastic relations

$$\begin{aligned} \overline{\mathbf{I} \cdot \mathbf{K}} &= 3\kappa(\mathbf{I} \cdot \mathbf{D}), \\ \dot{\mathbf{M}} &= 2\mu \{ \mathbf{R}_E^T \text{dev}(\mathbf{D}) \mathbf{R}_E - \mathbf{D}_P \}, \end{aligned} \quad (2.2)$$

for the Kirchhoff stress  $\mathbf{K}$  in the context of the orthogonal split

$$\mathbf{K} = \frac{1}{3}(\mathbf{I} \cdot \mathbf{K}) \mathbf{I} + \text{dev}(\mathbf{K}) \quad (2.3)$$

of  $\mathbf{K}$  into spherical and deviatoric parts, with

$$\mathbf{M} = \mathbf{R}_E^T \text{dev}(\mathbf{K}) \mathbf{R}_E \quad (2.4)$$

These relations are determined in particular by the continuum deformation rate  $\mathbf{D} = \text{sym}(\mathbf{L})$  and its inelastic counterpart  $\mathbf{D}_P$ , with  $\mathbf{L} = \dot{\mathbf{F}}\mathbf{F}^{-1}$  the velocity gradient, and  $\mathbf{F}$  the deformation gradient. As usual for metals,  $\mathbf{D}_P$  is assumed to satisfy incremental inelastic incompressibility  $\mathbf{I} \cdot \mathbf{D}_P = 0$ . In addition, we also have  $\mathbf{I} \cdot \mathbf{D} \approx 0$ . Here,  $\kappa$  represents the elastic bulk modulus, and  $\mu$  the shear modulus, both with respect to the reference configuration. For simplicity, we also neglect the plastic spin  $\mathbf{W}_P$  in what follows. In this case,  $\mathbf{R}_E$  is determined solely by  $\mathbf{W}$ . As such, it is purely kinematic in nature and a dependent constitutive quantity.

Turning next to the inelastic behavior, we work with the standard isotropic form

$$\phi = \sigma_v(\mathbf{M} - \mathbf{X}) - \sigma_{Y0} - r \quad (2.5)$$

of the yield function. Here,

$$\sigma_v(\mathbf{M} - \mathbf{X}) = \sqrt{\frac{3}{2} \text{dev}(\mathbf{M} - \mathbf{X}) \cdot \text{dev}(\mathbf{M} - \mathbf{X})} \quad (2.6)$$

represents the von-Mises equivalent stress. Further,  $\mathbf{X}$  represents the back stress, and  $\sigma_{Y0}$  represents the initial yield stress. In the current associated context,  $\phi$  determines in particular the inelastic deformation rate

$$\mathbf{D}_P = \lambda \partial_{\mathbf{M}-\mathbf{X}} \phi = \lambda \mathbf{N} \quad (2.7)$$

in terms of the measure

$$\mathbf{N} = \sqrt{\frac{3}{2}} \frac{\text{dev}(\mathbf{M} - \mathbf{X})}{|\text{dev}(\mathbf{M} - \mathbf{X})|} \quad (2.8)$$

of the direction of the effective flow stress. In the current rate-independent context,  $\lambda$  represents the plastic multiplier enforcing rate-independence.

Consider next the evolution relations for hardening. Isotropic hardening is described here using the Voce or Swift laws. The Voce law takes the form

$$r = (\sigma_{Y\infty} - \sigma_{Y0}) [1 - \exp(-c_r \alpha)] \quad (2.9)$$

Here,  $\sigma_{Y\infty}$  is the saturation value of the yield stress,  $\sigma_{Y0}$  is the initial yield stress,  $c_r$  controls the saturation rate, and  $\alpha$  represents the accumulated equivalent inelastic deformation, with evolution relation

$$\dot{\alpha} = \lambda \quad (2.10)$$

The Swift law is given by

$$r = \sigma_{Yr} (\alpha_0 + \alpha)^n \quad (2.11)$$

In this relation,  $\sigma_{Yr}$  and  $\alpha_0$  are related to the initial yield stress via  $\sigma_{Y0} = \sigma_{Yr} \alpha_0^n$ , and  $n$  is the hardening exponent. In contrast to the Voce model, note that the Swift model predicts no saturation of the yield stress. Turning next to kinematic hardening, the evolution of the back stress  $\mathbf{X}$  is given here by the Armstrong-Frederick form

$$\dot{\mathbf{X}} = c_x (x_{\text{sat}} \mathbf{N} - \mathbf{X}) \lambda \quad (2.12)$$

involving growth and dynamic recovery. Here,  $c_x$  represents the growth rate, and  $x_{\text{sat}}$  the saturation magnitude of the back stress.

The above relations contain a number of material parameters to be stipulated or determined. These include  $\sigma_{Y0}$ ,  $\sigma_{Y\infty}$ , and  $c_r$  in the case of the Voce law,  $\sigma_{Yr}$ ,  $\alpha_0$  and  $n$  in the case of the Swift law, as well  $c_x$  and  $x_{\text{sat}}$  in the case of kinematic hardening. This completes the material model summary. Next, we turn to algorithmic considerations.

### 2.3 Algorithmic formulation of the material model

In the context of the material model summarized in the last section, the goal of the present work is the investigation of the effects of some numerical issues on the simulation of metal forming processes and concomitant effects such as springback. To this end, the above material model has been implemented in the implicit finite-element program ABAQUS/Standard via the user-material interface UMAT. Therefore, both forming and springback processes were simulated using ABAQUS/Standard.

Consider the implicit numerical integration and solution of the model over a finite time-interval  $[0, d] = \bigcup_{n=0}^{m-1} [t_n, t_{n+1}]$  consisting of  $m$  disjoint subintervals  $[t_0, t_1], \dots, [t_{m-1}, t_m]$ . Each such subinterval  $[t_n, t_{n+1}]$  is of duration  $t_{n+1, n} = t_{n+1} - t_n$ . As is common, the deformation gradient  $\mathbf{F}_n$ , as well as the values  $\mathbf{R}_{En}$ ,  $\mathbf{M}_n$  and  $\mathbf{X}_n$  are all known at the start  $t = t_n$  of this interval from the solution for the last one. On this basis, the current algorithm calculates the updates  $\mathbf{R}_{En+1}$ ,  $\mathbf{M}_{n+1}$  and  $\mathbf{X}_{n+1}$  directly from the current algorithmic value  $\mathbf{F}_{n+1}$  of  $\mathbf{F}$ ,



representing in the current isothermal context the basic input at the Gauss-point level. In the context of commercial user interfaces such as ABAQUS UMAT, this means that we require as input variables (*i.e.*, in the incremental case) only  $\mathbf{F}_n$  and  $\mathbf{F}_{n+1}$ . All other quantities made available by such interfaces are not needed.

Assuming that  $\mathbf{L} = \dot{\mathbf{F}}\mathbf{F}^{-1}$  is approximately constant in the interval  $[t_n, t_{n+1}]$ , exponential backward-Euler integration yields the approximation

$$\mathbf{L}_{n+1,n} := t_{n+1,n} \mathbf{L}_{n+1} = \ln(\mathbf{F}_{n+1,n}) = \mathbf{H}_{n+1,n} - \frac{1}{2} \mathbf{H}_{n+1,n}^2 + \frac{1}{3} \mathbf{H}_{n+1,n}^3 - \dots \quad (2.13)$$

for the incremental velocity gradient in terms of the corresponding relative displacement  $\mathbf{H}_{n+1,n} = \mathbf{F}_{n+1,n} - \mathbf{I}$  and deformation  $\mathbf{F}_{n+1,n} = \mathbf{F}_{n+1} \mathbf{F}_n^{-1}$  gradients. Assuming  $|\mathbf{H}_{n+1,n}| \ll 1$ , this will be approximated here for algorithmic simplicity by the midpoint form

$$\mathbf{L}_{n+1,n} = \mathbf{H}_{n+1,n} [\mathbf{I} + \frac{1}{2} \mathbf{H}_{n+1,n}]^{-1} = \mathbf{H}_{n+1,n} - \frac{1}{2} \mathbf{H}_{n+1,n}^2 + \frac{1}{4} \mathbf{H}_{n+1,n}^3 - \dots \quad (2.14)$$

In turn,  $\mathbf{L}_{n+1,n}$  determines the measures  $\mathbf{D}_{n+1,n} = \text{sym}(\mathbf{L}_{n+1,n})$  and  $\mathbf{W}_{n+1,n} = \text{skw}(\mathbf{L}_{n+1,n})$  of incremental strain and rotation, respectively. Consequently, both these quantities and the trace

$$\mathbf{I} \cdot \mathbf{K}_{n+1} = \mathbf{I} \cdot \mathbf{K}_n + 3\kappa (\mathbf{I} \cdot \mathbf{D}_{n+1,n}) \quad (2.15)$$

of the Kirchhoff stress obtained from backward-Euler integration of (2.2)<sub>1</sub> are determined directly by  $\mathbf{F}_{n+1,n}$ .

In the context of the backward-Euler approximation, numerical time-integration of the evolution relations (2.1), (2.2)<sub>2</sub>, (2.12) and (2.10) over an arbitrary time interval  $[t_n, t_{n+1}]$  yields the implicit system

$$\begin{aligned} \mathbf{r}_{\mathbf{M}_{n+1,n}} &= \mathbf{M}_{n+1,n} - 2\mu \{ \mathbf{R}_{\mathbf{E}n+1}^T \text{dev}(\mathbf{D}_{n+1,n}) \mathbf{R}_{\mathbf{E}n+1} - \lambda_{n+1,n} \mathbf{N}_{n+1} \} = \mathbf{0}, \\ \mathbf{r}_{\mathbf{X}_{n+1,n}} &= \mathbf{X}_{n+1,n} - c_x \{ x_{\text{sat}n+1} \mathbf{N}_{n+1} - \mathbf{X}_{n+1} \} \lambda_{n+1,n} = \mathbf{0}, \\ r_{\alpha_{n+1,n}} &= \alpha_{n+1,n} - \lambda_{n+1,n} = 0, \\ r_{\lambda_{n+1,n}} &= \phi_{n+1} = 0, \end{aligned} \quad (2.16)$$

for the unknowns  $\mathbf{M}_{n+1}$ ,  $\mathbf{X}_{n+1}$ ,  $\alpha_{n+1}$  and  $\lambda_{n+1,n} := t_{n+1,n} \lambda_{n+1}$ . Again, recall that we are neglecting the plastic spin  $\mathbf{W}_P$ . In this case,  $\mathbf{R}_{\mathbf{E}}$  is determined solely by  $\mathbf{W}$  and is purely kinematic in nature. Algorithmically, we have

$$\mathbf{R}_{\mathbf{E}n+1} = \text{exv}(\mathbf{w}_{n+1,n}) \mathbf{R}_{\mathbf{E}n}, \quad (2.17)$$

with  $\text{axv}(\mathbf{W})$  the axial vector of any skew-symmetric tensor  $\mathbf{W}$  and  $\mathbf{w}_{n+1,n} := \text{axv}(\mathbf{W}_{n+1,n})$ . Further, the vector form

$$\text{exv}(\mathbf{w}) = \mathbf{I} + \sin |\mathbf{w}| \text{axt}(\text{sgn}(\mathbf{w})) + (\cos |\mathbf{w}| - 1) \text{axt}(\text{sgn}(\mathbf{w}))^2 \quad (2.18)$$

of the Rodrigues formula maps any non-zero vector  $\mathbf{w}$  into a rotation  $\text{exv}(\mathbf{w})$  with rotation axis  $\text{sgn}(\mathbf{w}) := \mathbf{w}/|\mathbf{w}|$  and rotation angle  $|\mathbf{w}|$ . In addition,  $\text{axt}(\mathbf{w})$  is the skew-symmetric tensor induced by any Euclidean vector  $\mathbf{w}$ , *i.e.*,  $\text{axt}(\mathbf{w})\mathbf{a} := \mathbf{w} \times \mathbf{a}$  for all  $\mathbf{a}$ . Introducing then the array

$$\boldsymbol{\epsilon}_{n+1} := \{ \mathbf{M}_{n+1}, \mathbf{X}_{n+1}, \alpha_{n+1}, \lambda_{n+1,n} \} \quad (2.19)$$

of all internal variables, the backward-Euler system can be written in the compact form

$$\mathbf{r}_{\epsilon_n}(\epsilon_{n+1}; \mathbf{F}_{n+1}) = \mathbf{0} \quad . \quad (2.20)$$

On this basis, this system can be solved in standard predictor-corrector fashion (e.g., Simo and Hughes, 1998, Chapter 8). Note that in the elastic corrector step (i.e.,  $\phi_{n+1}^{\text{tr}} < 0$ ), the system (2.16) reduces to the form

$$\begin{aligned} \mathbf{M}_{n+1} &= \mathbf{M}_n + 2\mu \mathbf{R}_{\mathbf{E}n}^{\text{T}} \text{dev}(\mathbf{D}_{n+1,n}) \mathbf{R}_{\mathbf{E}n} , \\ \mathbf{X}_{n+1} &= \mathbf{X}_n , \\ \alpha_{n+1} &= \alpha_n . \end{aligned} \quad (2.21)$$

Lastly, we require the algorithmic derivative  $\partial_{\mathbf{F}_{n+1}}^a \mathbf{K}_{n+1}$  of the Kirchhoff stress  $\mathbf{K}_{n+1}$  with respect to  $\mathbf{F}_{n+1}$  for consistent linearization of the algorithmic weak form. This is based on the result

$$\mathbf{K}_{n+1} = \frac{1}{3} \kappa (\mathbf{I} \cdot \mathbf{D}_{n+1,n}) \mathbf{I} + \mathbf{R}_{\mathbf{E}n+1} \mathbf{M}_{n+1} \mathbf{R}_{\mathbf{E}n+1}^{\text{T}} \quad (2.22)$$

for  $\mathbf{K}_{n+1}$  from (2.3), (2.4), and (2.15). On this basis, one obtains

$$\partial_{\mathbf{F}_{n+1}}^a \mathbf{K}_{n+1} = (\partial_{\mathbf{D}_{n+1,n}}^a \mathbf{K}_{n+1})(\partial_{\mathbf{F}_{n+1}} \mathbf{D}_{n+1,n}) + (\partial_{\mathbf{w}_{n+1,n}}^a \mathbf{K}_{n+1})(\partial_{\mathbf{F}_{n+1}} \mathbf{w}_{n+1,n}) \quad , \quad (2.23)$$

with

$$\partial_{\mathbf{D}_{n+1,n}}^a \mathbf{K}_{n+1} = \frac{1}{3} \kappa (\mathbf{I} \otimes \mathbf{I}) + (\mathbf{R}_{\mathbf{E}n+1} \square \mathbf{R}_{\mathbf{E}n+1}^{\text{T}})(\partial_{\mathbf{D}_{n+1,n}}^a \mathbf{M}_{n+1}) \quad (2.24)$$

and

$$\partial_{\mathbf{w}_{n+1,n}}^a \mathbf{K}_{n+1} = (\mathbf{K}_{n+1} \triangle \mathbf{I} + \mathbf{I} \square \mathbf{K}_{n+1})(\mathbf{I} \square \mathbf{R}_{\mathbf{E}n+1}^{\text{T}})(\partial_{\mathbf{w}_{n+1,n}}^a \mathbf{R}_{\mathbf{E}n+1}) \quad . \quad (2.25)$$

Here, the usual tensor products

$$\begin{aligned} (\mathbf{A} \square \mathbf{B})\mathbf{C} &:= \mathbf{ACB} , \\ (\mathbf{A} \triangle \mathbf{B})\mathbf{C} &:= \mathbf{AC}^{\text{T}}\mathbf{B} , \\ (\mathbf{A} \otimes \mathbf{B})\mathbf{C} &:= (\mathbf{B} \cdot \mathbf{C})\mathbf{A} , \end{aligned} \quad (2.26)$$

between second-order Euclidean tensors have been used. The backward-Euler system (2.20) yields the algorithmic derivatives

$$\begin{bmatrix} \partial_{\mathbf{D}_{n+1,n}}^a \mathbf{M}_{n+1} \\ \partial_{\mathbf{D}_{n+1,n}}^a \mathbf{X}_{n+1} \\ \partial_{\mathbf{D}_{n+1,n}}^a \alpha_{n+1} \\ \partial_{\mathbf{D}_{n+1,n}}^a \lambda_{n+1,n} \end{bmatrix} = - \begin{bmatrix} \partial_{\mathbf{M}_{n+1}} \mathbf{r}_{\mathbf{M}n} & \cdots & \partial_{\lambda_{n+1,n}} \mathbf{r}_{\mathbf{M}n} \\ \vdots & \ddots & \vdots \\ \mathbf{0} & \cdots & 0 \end{bmatrix}^{-1} \begin{bmatrix} \partial_{\mathbf{D}_{n+1,n}} \mathbf{r}_{\mathbf{M}n} \\ \mathbf{0} \\ \mathbf{0} \\ \mathbf{0} \end{bmatrix} \quad (2.27)$$

of the internal variables with respect to  $\mathbf{F}_{n+1}$ ; in compact form

$$\partial_{\mathbf{D}_{n+1,n}}^a \epsilon_{n+1} = -(\partial_{\epsilon_{n+1}} \mathbf{r}_{\epsilon_n})^{-1}(\partial_{\mathbf{D}_{n+1,n}} \mathbf{r}_{\epsilon_n}) \quad . \quad (2.28)$$

Here,  $(\partial_{\epsilon_{n+1}} \mathbf{r}_{\epsilon_n})$  represents the Jacobian of the system (2.20). In particular,

$$\partial_{\mathbf{D}_{n+1,n}} \mathbf{r}_{\mathbf{M}n} = 2\mu (\mathbf{R}_{\mathbf{E}n+1}^{\text{T}} \square \mathbf{R}_{\mathbf{E}n+1}) \quad (2.29)$$

follows from (2.20)<sub>1,2</sub>. Lastly,

$$\begin{aligned}\partial_{\mathbf{F}_{n+1}} \mathbf{D}_{n+1,n} &= \frac{1}{2} (\mathbf{I} \square \mathbf{I} + \mathbf{I} \triangle \mathbf{I}) (\partial_{\mathbf{H}_{n+1,n}} \mathbf{L}_{n+1,n}) (\mathbf{I} \square \mathbf{F}_n^{-1}), \\ \partial_{\mathbf{F}_{n+1}} \mathbf{w}_{n+1,n} &= \frac{1}{2} \text{axv} (\mathbf{I} \square \mathbf{I} - \mathbf{I} \triangle \mathbf{I}) (\partial_{\mathbf{H}_{n+1,n}} \mathbf{L}_{n+1,n}) (\mathbf{I} \square \mathbf{F}_n^{-1}),\end{aligned}\quad (2.30)$$

are obtained from the midpoint approximation (2.14) to the exact algorithmic expression (2.13).

For the implementation of the above algorithm in ABAQUS UMAT, we require only the “material part” of  $\partial_{\mathbf{F}_{n+1}}^a \mathbf{K}_{n+1}$ . In the current context, we have

$$\text{DDSDDE} \equiv \det(\mathbf{F}_{n+1}^{-1}) (\partial_{\mathbf{D}_{n+1,n}}^a \mathbf{K}_{n+1}) \quad . \quad (2.31)$$

where DDSDDE represents the ABAQUS UMAT variable for the material part of the consistent tangent. This together with the current algorithmic state of stress  $\mathbf{K}_{n+1}$  (in the form of the corresponding Cauchy stress) are returned to ABAQUS/Standard for the global solution via global Newton-Raphson iteration. Again, we emphasize that the implementation of the current algorithm in ABAQUS UMAT requires only the variables DFGRD0  $\equiv \mathbf{F}_n$  and DFGRD1  $\equiv \mathbf{F}_{n+1}$  as input. All other quantities made available by such interfaces are not needed.

## 2.4 Shell element formulations

ABAQUS provides both conventional shell elements and continuum shell elements. Conventional shell elements are formulated with respect to a reference surface having displacement and rotational degrees of freedom at each node. Shell thickness is defined for such elements by the user as an element property (shell section). As is the case of ABAQUS, such elements are generally based on the plane-stress assumption. In contrast to such elements, continuum shell elements possess only displacement degrees of freedom. Both element types allow for a variable number of integration points through the thickness. Although not necessary, continuum shell elements in ABAQUS, as well as many in the literature (*e.g.*, Hauptmann and Schweizerhof, 1998) also work with the plane-stress assumption.

For the forming simulations of interest here, large-deformation continuum and conventional shells are relevant. In the latter case, the shell element S4R (4-node doubly curved general-purpose shell) is most frequently used. Each node has three displacement and three rotation degrees of freedom. Bilinear interpolation is used. This element is based on a mixed finite element formulation in which neither pure Kirchhoff-Love nor pure Mindlin-Reissner theory is used. Instead, thick shells use a theory similar to that of Mindlin-Reissner and the formulation of thin shells is similar to that of the discrete Kirchhoff theory. A transverse shear strain field is used in the formulation and it is calculated at the element center. Besides this, S4R is a reduced integration element with stabilization control against hourglassing. The membrane behavior of this element is based on the uniform strain formulation for a 4-node quadrilateral plane-stress element. Beyond such elements, stress/displacement continuum shell elements in ABAQUS are also used in three-dimensional sheet forming analysis. These elements have displacement degrees of freedom only and are based on linear interpolation.

It is known that continuum shell elements such as SC6R and SC8R (6 and 8-node in-plane general-purpose continuum shell with reduced integration, respectively) are more accurate in

contact modeling than conventional shells, since they employ two-sided contact taking into account changes in thickness no matter how thick the elements are compared to other element dimensions. However, although continuum shells provide robust and accurate solutions to most shell applications, these elements may show slow convergence for very thin shell applications. In such cases conventional thin shell elements should be used, as we will see later on.

## 2.5 Contact and friction modeling

It is well known that contact between at least two bodies is an essential feature of just about every metal forming simulation. Appropriate modeling of the contact conditions is vital to the success of such simulations. In typical forming applications, the tools like dies deform very little and are modeled as rigid bodies. In the current work, the attention will be focused on the interface between a deformable body and a rigid body.

In order to introduce the contact algorithm used in this work, consider now first the kinematics of the interacting surfaces. As shown in ABAQUS Theory Manual, let  $A$  be a point on the deforming mesh, with current coordinates  $x_A$ . Let  $C$  be the rigid body reference node that defines the position of the rigid body with current coordinates  $x_C$ . Let  $A'$  be the closest point on the surface of the rigid body to  $A$  at which the normal to the surface of the rigid body passes through  $A$ . Define  $r$  as the vector from  $C$  to  $A'$ . The configuration described by these quantities is shown in Figure 2.1. Here,  $h$  is the distance from  $A'$  to  $A$  along direction  $-n$ : the

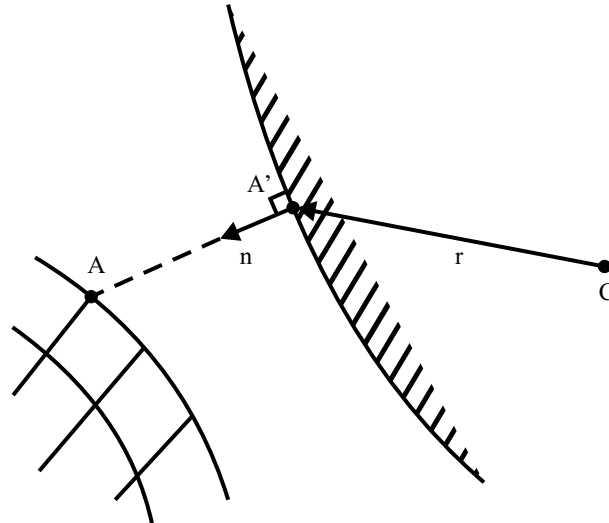


Figure 2.1: Rigid boundary surface geometry (ABAQUS 6.5-3 Theory Manual 5.1.3).

”overclosure” of the surfaces. From the definitions introduced above, we have

$$h \mathbf{n} = -\mathbf{x}_A + \mathbf{x}_C + \mathbf{r} \quad . \quad (2.32)$$

Then if  $h < -c$ , there is no contact between the surfaces at  $A$ , and no further surface interaction calculations need be done at this point. Here  $c$  is the clearance below which contact occurs. We define a ”hard” surface for the case of  $c = 0$ . The standard contact relationship using the ”hard” surface is defined as ”hard contact”, which is the most frequently used contact in

ABAQUS/Standard. The hard contact allows no penetration of the slave nodes into the master surface, thus, leading to "real" contact.

The conventional shell element formulation in ABAQUS works with both "hard" contact and "softened" contact. Generally, when a "softened" contact relationship is used, the contact pressure is a function of the clearance between the surfaces. The pressure-overclosure relationship can be prescribed by using different forms, *e.g.*, an exponential form (Figure 2.2), which is used here. With this (softened) contact pressure-overclosure relationship, the surfaces begin to

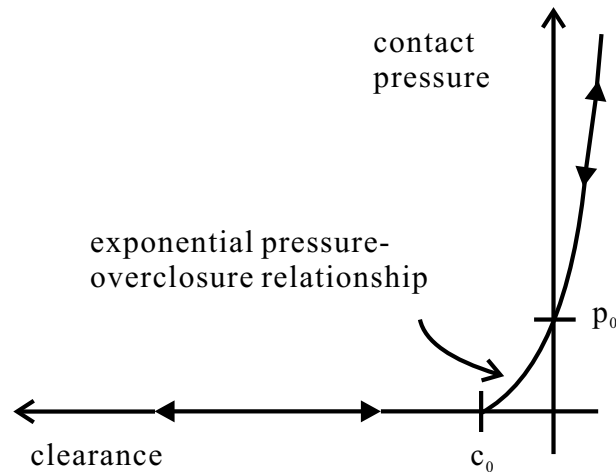


Figure 2.2: "Softened" pressure-overclosure relationship defined with the exponential relation (ABAQUS 6.5-3 Analysis's User's Manual 22.1.2).

transmit contact pressure once the clearance between them, as measured in the contact (normal) direction, reduces to  $c_0$ . The contact pressure transmitted between the surfaces then increases exponentially as the clearance continues to diminish. Later we will show that the parameter  $p_0$  can have a significant effect on the simulation results, and in particular on the predicted amount of springback. In ABAQUS/Standard contact constraints are enforced with the Lagrange multiplier method. All contact inequalities must be satisfied before the solution is accepted. For each potential contact point the contact condition is described by a single, often nonlinear, inequality constraint. With full Newton method used in ABAQUS/Standard, optimal and reliable convergence is only obtained if the stiffness is calculated properly. Since with contact the stiffness depends on the surface curvature, if the die surface is not smooth, the curvature tensor becomes singular and convergence cannot be guaranteed. In particular, in metal forming processes, contact occurs between a deformable body (blank) and one or more rigid bodies (forming tools). In such cases, a pure master-slave relationship is enforced. The surface of the blank is considered as the slave, and the surface of the forming tool is considered as the master. The contact constraint algorithm precludes penetration of nodes on the slave surface through the master surface, but the algorithm does not preclude penetration of nodes on the master surface through the slave surface (*e.g.*, in the case of insufficient mesh refinement of the blank). Therefore, if we use softened pressure-overclosure relationship, the higher contact pressure will lead to less penetration of the master surface through the slave surface and keep the result more reasonable.

The friction between the die and the workpiece plays a significant role in metal forming simulations. We distinguish between *cohesive* and *adhesive* friction. In cohesive friction the

sliding stresses depend on the yield stress of the workpiece, and the sliding actually occurs in a small boundary layer in the workpiece. This is typical in (but not limited to) bulk forming processes. In adhesive friction, the sliding stresses are proportional to the contact stress. In this case, sliding occurs between the die and the workpiece, which is typical in (but not limited to) sheet forming processes. Adhesive friction is modeled in ABAQUS with a classical Coulomb friction model. The friction coefficient and contact pressure are both important here. In the current investigations, isotropic adhesive friction is assumed. As we will see later, the corresponding (isotropic) friction coefficient  $\mu$  has a significant influence on sheet forming and springback.

## 2.6 Convergence behavior and numerical integration

The sheet forming example used in the current investigation involves cylindrical deep-drawing followed by ring-splitting. In this test, a cylindrical deep drawn cup is sliced into several rings which are then split in the vertical direction. Due to high residual stresses resulting from the deep drawing process, significant springback in the form of ring opening takes place (Figure 2.3). In the current context, the circular blank being drawn has an initial radius of 140 mm

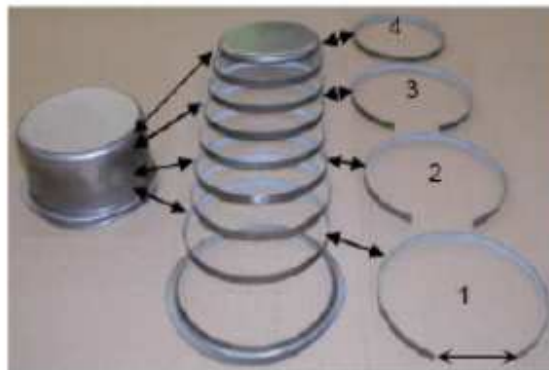


Figure 2.3: Ring-splitting test on the steel DC04 (Rohleder et al., 2001).

and an initial thickness of 0.6 mm. The punch has a radius of 73.35 mm and is rounded off at the corner with a radius of 8 mm. The die has an internal radius of 76 mm and is rounded off at the corner with a radius of 6.5 mm. The blank holder has an internal radius of 76 mm. The blank holder force used set at 130 kN and the maximum punch displacement at 89 mm. An oil lubricant is applied to both sides of blanks to reduce friction. Four circular rings of 10 mm width are cut from the formed cup and then split, resulting in ring opening as shown in Figure 2.4. Springback here is quantified by the ring opening after splitting. This results from the release of residual stresses which build-up and develop in the closed structure during deep drawing. For more information on this test, the reader is referred to the work of Rohleder et al. (2001).

Simulations are carried out for deep drawing of a cylindrical cup followed by ring splitting and ring opening after splitting. ABAQUS Version 6-5.3 was used for all simulations. In order to obtain more accurate results and reduce the sources of simulation errors, the static

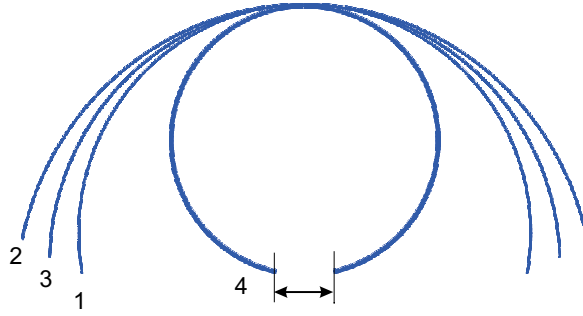


Figure 2.4: Definition of springback in terms of ring opening.

implicit method was used for both cup drawing and springback for the most simulations. Due to the symmetry of the part, only half of the 3D structure was modeled. Neglecting the initial flow anisotropy for simplicity, we have two possibilities. In the first case, the deep drawing stage was simulated using the 2-node linear axisymmetric shell element SAX1 to reduce the computational cost. In a second step, these results are transformed to a three-dimensional FE model for half of the cup using the general purpose shell elements S3 or S4 in order to carry out the ring-splitting process. For the purpose of investigation of numerical factors such as element number and integration points, the 3D shell element S4R is used for both deep drawing and ring splitting stages. The remaining numerical studies are carried out using a combination of the axisymmetric and 3D models. For simplicity, the punch, the die and the blank holder are modeled as analytical rigid surfaces. The mechanical interaction between the contact surfaces is set to be frictional contact using the isotropic Coulomb model with friction coefficient 0.07. For the numerical investigations to follow, the combined hardening with Voce-type isotropic hardening is generally assumed. The corresponding parameter values assumed are those for the steel DP600 as given in Table 2.1.

parameter	value	units
$\kappa$	158333	MPa
$\mu$	73077	MPa
$\sigma_{Y0}$	308.3	MPa
$c_r$	6.75	
$\sigma_{Y\infty}$	673.9	MPa
$x_{\text{sat}}$	225.3	MPa
$c_x$	73.7	

Table 2.1: Material model parameter values for DP600 (Banu et al., 2001).

### 2.6.1 Convergence behavior

We begin with a convergence study for the finite element discretizations used in the context of the deep-drawing and ring-splitting simulations. To this end, we work with the amount of draw-in. As shown in Figure 2.5, this represents the horizontal displacement of a point in the flange edge during the drawing stage. The results in Figure 2.6 (left) imply that 15372 elements are sufficient for a convergence solution as judged by the amount of draw-in (with

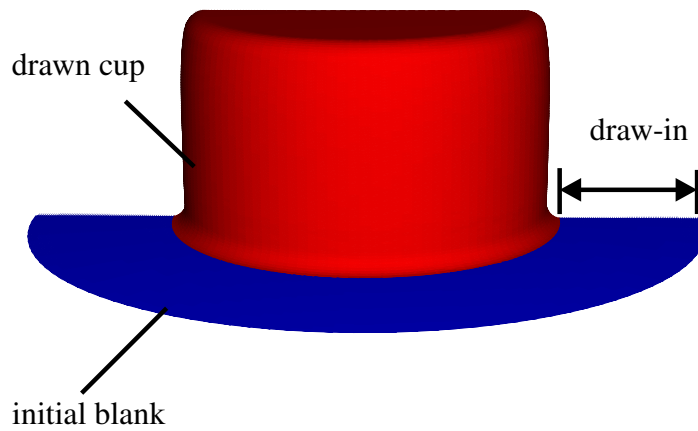


Figure 2.5: Definition of the amount of draw-in during the cup drawing.

100 elements in the circumferential direction and 15 elements in the width direction for one ring as shown in Figure 2.7). In contrast to other forming processes like bending, where the

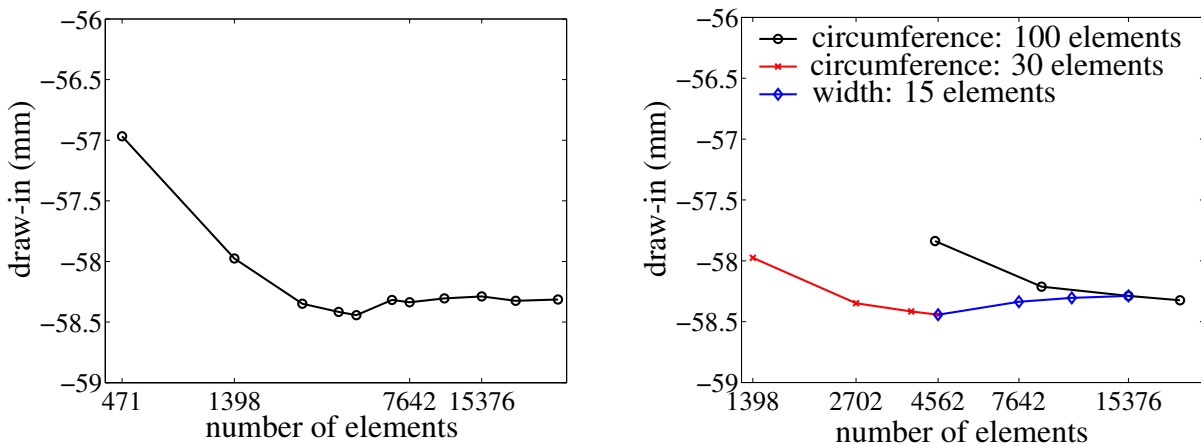


Figure 2.6: Influence of the number of elements on the amount of draw-in. Left: Increasing number of elements in both width and circumferential directions. Right: Mesh refinement in either the width or circumferential direction.

discretization along the strip is most important, the ring-splitting is more complicated, such that discretization in both the width and circumferential directions because of the excessive stretching and compression in both. Figure 2.6 (right) displays the influence of increasing the number of elements in either width or circumferential direction while fixing the number of elements in the other direction. In particular, we looked at refinement in the width direction for (i) 100 elements and (ii) 30 elements in the circumferential direction, as well as at refinement in the circumferential direction for (iii) 15 elements in the width direction. As shown, the results are more sensitive to the number of elements along the width direction of the blank and width direction of the rings. Indeed, in the case of a finer mesh (15 elements) in the width direction (Figure 2.6, right), increasing the number of elements in the circumferential direction



has no significant effect. The reason why the convergence behavior is more sensitive to mesh refinement in the width than in the circumferential direction could have to do with that the curvature difference in the tool in two directions. For example, the curvature in the width direction of the die is much larger than the curvature in its circumferential direction, which implies that the bending of the sheet in the width direction is more extreme. Furthermore, the deformation in the width direction involves strong bending and unbending, while in the circumferential direction only relatively mild bending occurs.

It is also of interest to investigate convergence in the context of ring splitting. The corresponding finite-element mesh is shown in Figure 2.7. Figure 2.8 shows the four ring opening

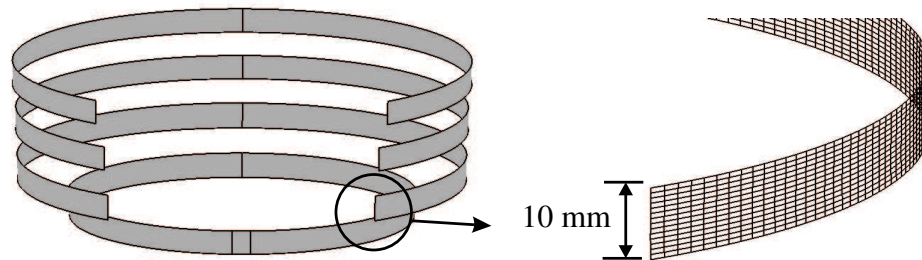


Figure 2.7: Example of a finite element mesh for the ring-splitting test (circumference  $\times$  width =  $100 \times 15$  elements).

values as a function of the number of elements used in the simulation. Note that the shape

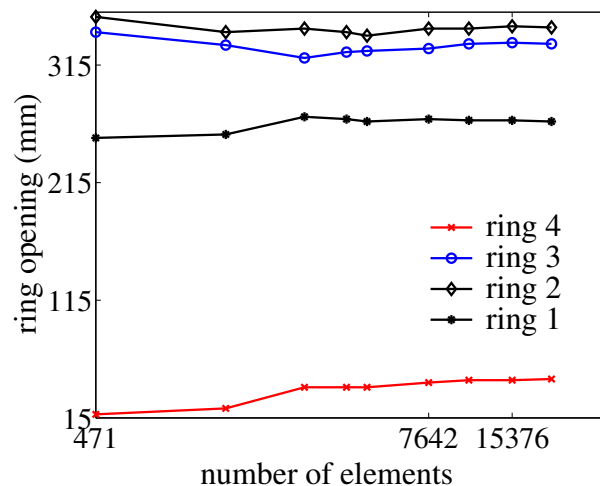


Figure 2.8: Influence of the number of elements on the amount of ring opening after ring splitting.

of the elements basically remain the same. In terms of springback, the simulation using 7642 elements has not yet converged, in contrast to the draw-in results. Increasing the number of elements to 15376, however, appears to result in a converged solution with respect to the amount of springback. On this basis, we use 15376 elements and the mesh depicted in Figure 2.7 (with 100 elements in the circumferential direction and 15 elements in the width direction for one ring) for the simulations in what follows.

### 2.6.2 Shell elements

It is well known that the element formulation or element type employed in the simulation could influence the results quite much, particularly in the case of precise prediction of springback behavior. To look briefly into a possible influence of the shell element formulation on simulation results, consider for simplicity the case of the draw-bending test (*e.g.*, Kleiner et al., 2003, 2005). In this test, a straight sheet metal strip is bent approximately  $90^\circ$  around a roller at the top of the machine, clamped at both ends, and then pulled from left to right around the roller. The advantage of this type of test lies in the minimization of friction since the roller turns with the sheet metal strip as it is bent. For more details, the reader is referred to Wang et al. (2006b). Figure 2.9 shows the simulated springback profile after draw-bending as based on the ABAQUS 3D conventional shell element S4R, and the ABAQUS continuum shell element SC8R. As shown, the springback results are quite insensitive to the shell element formulation

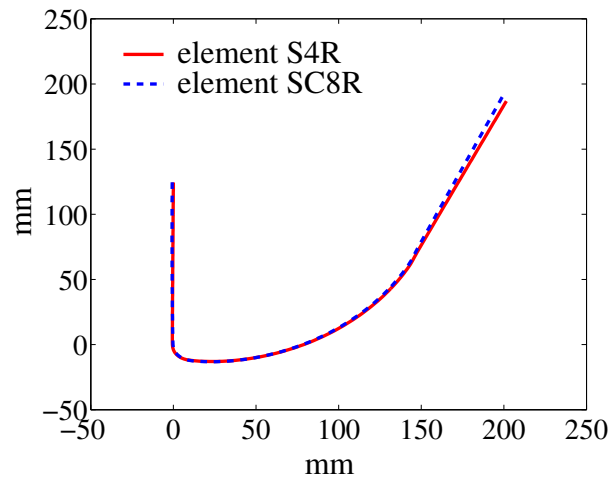


Figure 2.9: Influence of the element formulation on the simulation results for the draw-bending test.

chosen in the case of draw-bending. Indeed, as discussed above, more important in the context of sheet metal forming simulations are issues such as contact modeling. The conventional shell element SR4 is combined in ABAQUS with softened contact, while the continuum shell SC8R employs hard contact. This is most likely why the springback effect is slightly larger for the continuum shell case (Figure 2.9). Even in this case of different contact algorithms, however, the simulation results for the two element formulations deviate very little from each other. Therefore, considering the efficiency of the conventional shell element, we will focus our attention on only conventional shell elements in what follows.

### 2.6.3 Number of integration points in the thickness direction

As is well-known, the resolution of the residual stress state and the amount of springback predicted in the simulation are quite sensitive to the number of integration points used in the thickness direction (also called section points: Wagoner et al., 2002). The purpose of this section is to examine this issue in the context of the ring splitting simulation.

Figure 2.10 shows the simulation results using S4R with a variable number of integration points along the shell thickness. The results shown here demonstrate indeed the sensitivity

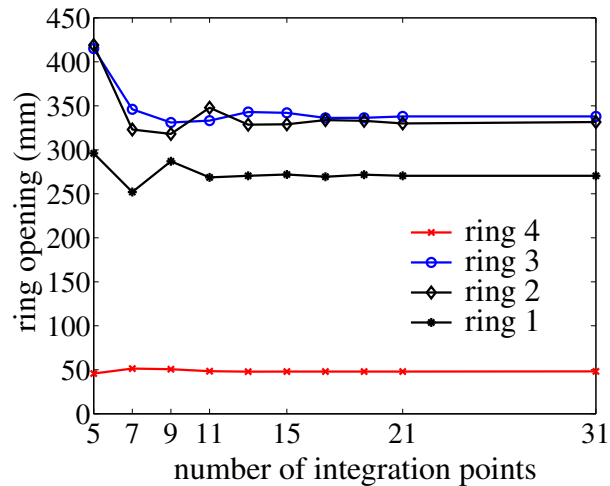


Figure 2.10: Influence of the number of integration points on the simulation results for ring opening.

of springback behavior to the number of integration points used. Note that the ring opening solution oscillates when the number of the integration points is less than 15. In addition, the order of the springback values for rings 2 and 3 shifts when 11 and 15 integration points are used. When 11 integration points are used, the values are 333.2 mm and 347.8 mm respectively, while in the case of 15 integration points, we obtain the springback values of 338.0 mm and 330.0 mm for ring 2 and ring 3, respectively. As such, 11 integration points, often regarded as sufficient, do not yield a convergent solution in the current context. On the basis of the results in Figure 2.10, at least 21 integration points would appear to be necessary for solution convergence in the context of springback prediction for the ring-splitting test.

Consider next the residual stress distribution after forming along the thickness in the case of 11 integration points and 21 integration points. In the ring splitting case, the amount of ring opening is related to the stress gradient in the thickness direction, particularly in the circumferential or tangential component of stress. Figure 2.11 shows the two curves of the tangential stress distribution in the case of 11 and 21 integration points for one element on the ring 2. As

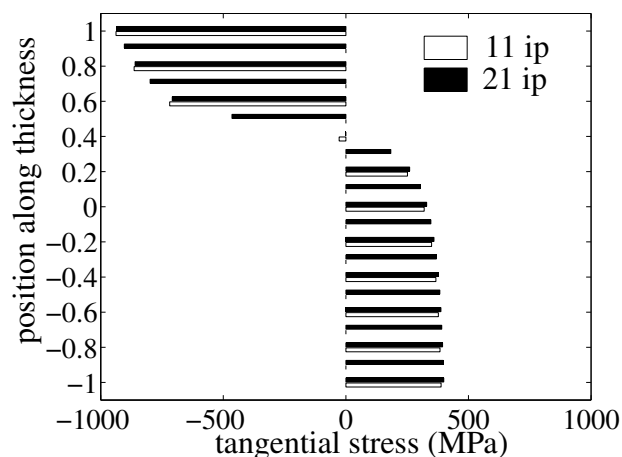


Figure 2.11: Tangential stress distribution along the thickness direction (ring 2). Here, "ip" means "integration points." The vertical axis represents the fraction in the thickness direction.

shown, on the compressed side of the shell, the stress magnitude with 11 integration points is slightly larger than that with 21 integration points. On the stretched side, this trend is reversed. These differences explain why the springback for ring 2 with 11 integration points is larger than in the case of 21 integration points. Added up over the entire structure, one obtains significantly different predictions for the structure as a whole.

## 2.7 Structural, process and boundary conditions

As shown in the previous sections, several numerical aspects of the simulation can have a considerable effect on the prediction of springback. Beyond this, of course, the process and boundary conditions play a role in the amount of springback obtained. In what follows, we consider briefly in this regard the contact pressure, the blank holding force, frictional effects, and geometric factors such as the tool radius.

### 2.7.1 Contact pressure

The contact between tool and sheet is a main controlling factor for most metal forming processes. As such, it is important to study its influence on simulation results. To simplify things, axisymmetric conditions are assumed and the element SAX1 with softened contact as discussed in the previous section is used. The contact algorithm used in this test is the contact pair algorithm between a deformed body and an analytical rigid body. The over-closure relationship is assumed to be in exponential form. In fact, the accuracy of the softened contact is determined by the value of the pressure when at zero clearance. Too small a value of the stiffness causes over-penetration, but has the benefit of smoother contact. On the other hand, too large value will lead to convergence difficulties. A parameter study on the effect of contact pressure on the springback has been performed with ABAQUS/Standard. The results are shown in Figure 2.12. For rings 3 and 4, we can see that a larger contact pressure results in smaller openings

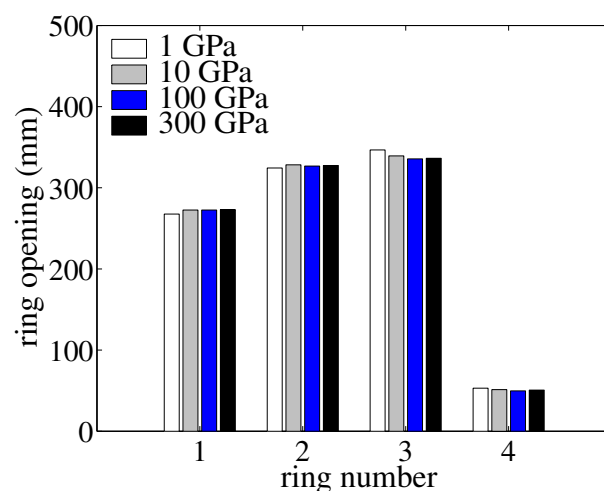


Figure 2.12: Dependence of predicted ring opening on the contact pressure.

of the split rings, while for ring 1 and 2, the results are basically on the contrary. In addition, the fluctuation of the ring openings for ring 3 is larger (larger than 6 mm) than that for other rings (less than 5 mm) when the pressure increases. Note that the amount of springback remains

basically unchanged when the contact pressure is larger than 100 GPa, which could be taken as the contact parameter for the converged solution.

### 2.7.2 Holder force

In Figure 2.13 are displayed the results for the ring-splitting simulation assuming different blank holder forces (65 kN, 130 kN and 260 kN) for the axisymmetric case. The results for rings 1

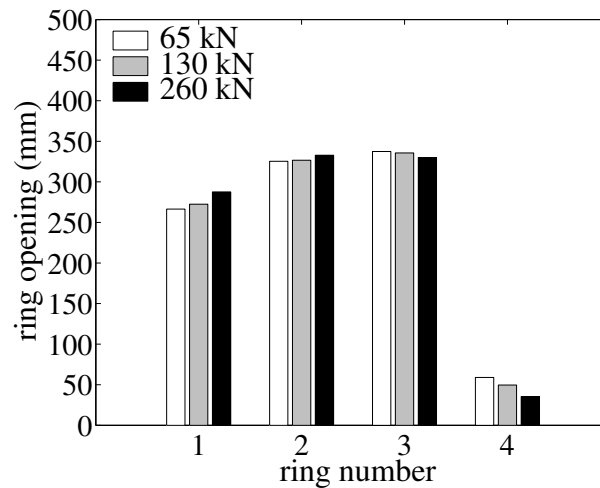


Figure 2.13: Springback sensitivity to holder force after ring-splitting.

and 2, for example, *i.e.*, the larger the holder force, the more springback, are as expected. On the other hand, those for rings 3 and 4 are reversed. This may have to do with the fact that rings 1 and 2 come from near the cup edge, while 3 and 4 come from the cup bottom. For ring 1 and 2, most of the deformation is from the blank flange. Consequently, compression in the circumferential direction and bending-unbending in the width direction are the dominant deformation modes. In addition, friction combined with higher holder forces will result in more stretch of the blank in the width direction. The larger stretch in the width direction in the case of higher holder force leads to higher accumulated plastic strain and work-hardening, resulting in higher stress levels. These would in turn lead to larger elastic deformation in the material, leading to more springback. In contrast, for rings 3 and 4 are dominated by bending deformation. As such, there is less material from the flange area dragged into the die cavity compared as compared to rings 1 or 2. The resulting decrease in the level of plastic deformation results in a smaller amount of springback.

To examine briefly a possible role of the material behavior in this effect, consider the Swift model as an alternative model for isotropic hardening. In contrast to the Voce case, the Swift model assumes that there is no saturation. The material parameter values for DP600 in this case are shown in Table 2.2. Table 2.3 shows the simulation results for springback and two different holder forces. As can be seen, there is no change in the trend of the dependence of ring opening on holder force for different rings here. As such, this effect would seem to be independent of the material behavior. More nearly, it has to do with the amount of inelastic deformation accumulated and the corresponding proportions of the elastic and plastic deformation resulting in the four rings.

parameter	value	units
$\kappa$	158333	MPa
$\mu$	73077	MPa
$\sigma_{Y0}$	330.3	MPa
$\sigma_{Yr}$	1093.0	MPa
$\alpha_0$	0.00169	
$n$	0.187	

Table 2.2: Swift isotropic hardening model parameter values for DP600 (Banu et al., 2001).

holder force (kN)	ring opening (mm)			
	ring 1	ring 2	ring 3	ring 4
130	304.4	350.3	342.3	21.8
260	327.1	359.4	337.2	5.2

Table 2.3: Dependence of simulated ring opening on the magnitude of holder force after ring splitting on the basis of the Swift model.

If a very large deformation arises in the material, the bigger holder force would result in a larger elastic deformation portion while increasing the elastic energy portion stored in the structure, which finally increase the springback (like in ring 1). On the other hand, if the deformation is not large enough (like ring 4 where the increase of plastic deformation portion prevails in the total increased deformation over the increased elastic deformation), the increase of the holder force would result in decreased springback. In fact, the springback is also directly linked to the stress gradient along the shell thickness. The different stress distribution along the thickness would result in different kinds of springback and magnitudes. The overall effects and stress distribution will decide the final springback quantities. For these reasons, the trend of springback observed here has not been fully understood and this would be the subject of future investigation.

### 2.7.3 Friction coefficient

Consider next simulations with and without Coulomb friction. To this end, the friction coefficient was set to 0.0, 0.07 and 0.1 (in the experiment, a value of 0.07 is used). For simplicity, the simulations are performed with ABAQUS/Standard using the conventional shell elements. The corresponding springback predictions are listed in Table 2.4. From Table 2.4, it can be

$\mu$	ring opening (mm)			
	ring 1	ring 2	ring 3	ring 4
0.0	251.6	320.0	339.6	93.9
0.07	272.6	326.8	335.6	49.7
0.1	279.5	330.0	324.7	35.9

Table 2.4: Dependence of ring opening on the magnitude of friction after ring splitting.

concluded that friction has a large influence on the springback behavior. Not surprisingly, the trend observed here with respect to the rings is completely analogous to that for holder force

established in the last section. In other words, a larger friction coefficient (or holder force) leads to increased ring opening in rings 1 and 2 and to decreased ring opening in rings 3 and 4.

#### 2.7.4 Boundary conditions

Generally speaking, a springback simulation can be performed by gradually retracting the punch. Since this method of unloading requires additional numerical effort, the response of the sheet due to the release of the tool is often simulated in one step, representing a so-called instantaneous release (Meinders et al. (2005)). Sometimes this increment is subdivided into a number of subincrements in order to avoid numerical instabilities. These occur because the contact forces are suddenly removed and transformed to reaction forces. If these reaction forces are removed abruptly, this can easily result in local buckling effects. Such abrupt removal or change of boundary conditions can also occur during cutting or splitting of the rings. In this context, convergence problems have been observed in ring-splitting simulations during the springback step caused by the thin curved form of the rings. In this case, there are two approaches to solve the instability problem. One is the use of a stabilization technique based on damping. This approach has proven to be effective. On the other hand, this approach may result in inaccuracy if one is not careful about the choice of damping factor. Table 2.5 summarizes some simulation results for different damping factors. Clearly, this factor can have a significant effect. Gen-

damping factor	ring opening (mm)			
	ring 1	ring 2	ring 3	ring 4
$1 \times 10^{-3}$	11.2	12.1	11.2	1.4
$1 \times 10^{-4}$	65.2	69.9	64.4	8.7
$1 \times 10^{-5}$	266.5	318.4	325.6	47.8

Table 2.5: Dependence of ring opening on the choice of numerical damping factor in the ring-splitting simulation.

erally speaking, the smaller the damping factor, the more accurate is the simulation. The trick here is to choose the value of this factor such that the simulation converges reasonably well and is sufficiently accurate. Generally speaking, this can be achieved only by trial-and-error.

Given this state of affairs, consider now a second approach. In this approach, one releases the degrees of freedom (DOF) of the boundary conditions of the split edge step by step, resulting in a "gradual release". Table 2.6 summarizes some results depending on different release sequences. We can see that the use of the gradual release approach could perfectly retrieve the same result with the simulation without using the stabilization technique. In contrast, the simulation with the nonzero damping factor, which although is a very small value, produces an underestimation of the springback magnitude compared with that without stabilization option. Furthermore, we see that the gradual approach predicts basically the same results and is independent of the sequence of DOF release (the maximum deviation is only around 1%), since the release step is basically a pure elastic springback in this case.

Much work has been done on comparing the difference between tool release methods in the frictionless and friction situation for springback after deep drawing of open structures such as a channel (e.g., Haddag et al., 2005; Meinders et al., 2005; Samuel, 2000). As discussed,

release	ring opening (mm)			
	ring 1	ring 2	ring 3	ring 4
d.f. = $1 \times 10^{-5}$	266.5	318.4	325.6	47.8
d.f. = 0	272.6	326.7	335.6	49.6
gra. 3,4,5	272.6	326.8	335.6	49.7
gra. 4,5,3	269.5	323.1	333.2	49.7
gra. 4,3,5	272.6	326.6	335.6	49.7

Table 2.6: Dependence of ring opening after splitting on type of release modeling used. Here, "d.f." represents damping factor, "gra. 3,4,5" represents gradual release of the degree of freedom 3, 4 and 5 sequentially. "gra. 4,3,5" and "gra. 5,3,4" are analogous.

the different response of the gradual and instantaneous tool unloading procedures is probably linked to a slight increase of the plastic deformation during unloading. However, in the ring-splitting problem, even using a friction coefficient (*e.g.*, 0.07), there is no significant difference in springback for different methods of tool release (the results are omitted here), implying that the tool release methods have less influence on springback after the forming a closed structure.

## 2.8 Conclusions

Sheet metal forming simulations carried out using the finite-element method may be influenced by a number of numerical factors. These include the element formulation, the mesh size, the integration scheme, the contact and friction algorithms, and so on. Even more sensitive in this regard to such factors is the corresponding springback prediction. Firstly, using ring-splitting as a basic example process, the simulations using different mesh sizes show that the meshing scheme by which one ring is discretized by  $100 \times 15$  elements along circumferential and width direction is sufficient to yield a convergence solution. The conventional shell element and continuum shell element in ABAQUS seem to produce very similar results due to similar kinematic and constitutive behavior. Secondly, the current results show that springback after ring-splitting is particularly sensitive to the number of integration points in the thickness direction of the shell elements being used. The number of such points acceptable for forming simulations is usually not sufficient for the springback simulation. In the current case, at least 21 integration points seem to be necessary to obtain a convergence solution for springback. The influence of contact has been investigated with the help of the so-called softened contact for different contact pressure parameters. It has been shown that for increasing contact pressures, a more accurate solution has been attained. A pressure value no less than 100 GPa is necessary for ring-splitting simulations. For such contact pressure, the penetration of the master surface (tools) into the slave surfaces (blank) is very small so that the deformation of the blank will conform to the shape of the tool maximally. This leads to a more realistic result. Note that the contact also correlate with friction because the friction model is also influenced by contact pressure. In the case of friction, the interaction between contact, holder force and friction is very complex and the overall effect influences springback dramatically. As shown, a larger holder force or larger friction coefficient results in more springback for ring 1 and 2, and less springback for ring 3 and 4. The same trend is also observed for an increase in contact pressure. Finally, alternatives to



standard damping-based stabilization techniques, such as the gradual boundary release method suggested in this work, have been shown to prevent instability and buckling without influencing the results.



## Chapter 3

# On the modeling and simulation of directional hardening in metals\*

**Abstract** – The purpose of the current work is the formulation and application of a phenomenological model for directional hardening effects in metals subject to non-proportional loading. This model is motivated by that of Teodosiu and Hu (1995, 1998). In their model, a fourth-order symmetric tensor-valued stress-like internal variable  $S$  is introduced to account for the effect of the directional strength of planar dislocation structures on the material hardening behavior. The model for  $S$  is based on the formulation of evolution equations for its projections (1) parallel, and (2) orthogonal, to the current direction of (the rate of) plastic deformation. Being non-standard in the sense that these projections may evolve during elastic unloading, the numerical solution of this model is non-trivial. Several approaches have been proposed in the literature on how to do this, each leading to different physical results. The alternative model for directional hardening proposed here is based on an evolution relation for  $S$  itself. As in the model of Teodosiu and Hu (1995), this alternative model for directional hardening captures in particular hardening stagnation after a load reversal as well as cross hardening after an orthogonal strain-path change. Differences between the two models include their behavior during (i) monotonic shear loading and (ii) continuous strain-path changes. Besides this, plastic spin effects not accounted for in the Teodosiu model are taken into account in the current model.

### 3.1 Introduction

In general, metal forming processes involve large strains and severe strain-path changes. Large plastic strains lead in many metals to the development of persistent dislocation structures resulting in strong flow anisotropy. This induced anisotropic behavior manifests itself in the case of a strain-path change through different stress-strain responses depending on the type of strain-path change. Since metal forming processes involve both large plastic strains and severe strain-path changes, an adequate modeling of this induced flow anisotropy is crucial for the proper prediction of residual stresses and, consequently, of the amount of springback in structural components.

Many studies (*e.g.*, Ghosh and Backofen, 1973; Hiwatashi et al., 1997, 1998; Hoc and Forest, 2001; Rauch and Schmitt, 1989; Rauch and Thuillier, 1993; Strauven and Aernoudt, 1987; Thuillier and Rauch, 1994; Wilson and Bate, 1994) have investigated the influence of the microstructure on the hardening behavior for various strain-path changes. In particular, loading-path changes may lead to changes in dislocation structures and result in additional effects beyond those accounted for by standard isotropic and kinematic models. A number of studies on these effects (*e.g.*, Bouvier et al., 2005, 2003; Nesterova et al., 2001a,b) have been carried out in order to understand the macroscopic material behavior of polycrystalline metals under

---

\*Wang et al. (2006d)

strain-path changes at large deformations.

Among the material models accounting for these additional effects, that of Teodosiu and Hu (1995, 1998) has been used by a number of authors (*e.g.*, Bouvier et al., 2005, 2003; Li et al., 2003; Montleau, 2004) to model the induced anisotropic hardening behavior and its effect on the springback processes. In what follows, we refer to this model for simplicity as the Teodosiu model. In this model, evolving structure tensors are used to account for directional hardening effects resulting from the development of persistent dislocation structures during monotonic loading and from their re-organization upon changes in loading direction. The directional hardening behavior is also influenced by the effective polarity of excess dislocations of the same sign building up at these structures. In addition, the model accounts for “standard” kinematic and isotropic hardening effects. In the Teodosiu model, a fourth-order tensor-valued stress-like internal variable  $S$  is introduced to account for the effect of the directional strength of planar dislocation structures on the material hardening state. The variable  $S$  is described in such a way that the evolution equations are given for its projections parallel

$$s^d = \mathbf{A}_p \cdot S [\mathbf{A}_p] \quad (3.1)$$

and orthogonal

$$S^\ell = S - s^d \mathbf{A}_p \otimes \mathbf{A}_p \quad (3.2)$$

to the direction<sup>1</sup>

$$\mathbf{A}_p := \mathbf{D}_p / |\mathbf{D}_p| \quad (3.3)$$

of the inelastic deformation rate (“:=” means “is defined by”). Here,  $s^d$  represents the strength of the dislocation structures associated with the currently active slip systems, and  $S^\ell$  the strength of the dislocation structures associated with the latent slip systems. Several approaches were proposed in the literature how to integrate the evolution equations for  $s^d$  and  $S^\ell$  in order to obtain  $S$ . They lead, however, to different physical results (Montleau, 2004). The purpose of the current work is to formulate an alternative model for directional hardening as based on an evolution relation for  $S$  itself. As in the model of Teodosiu, the current model accounts for hardening stagnation after a load reversal as well as for cross hardening after an orthogonal strain-path change.

The paper begins (§2) with a discussion of some basic experimental observations relevant to the issue of directional hardening in the sense of Teodosiu and Hu. In this framework, we then review (§3) the formulation of the model as described in Teodosiu and Hu (1995) and discuss some aspects of the evolution of  $s^d$ ,  $S^\ell$  and  $S$  for different strain-paths on the basis of different integration schemes. Then (§4), we present our model for the evolution  $S$  and demonstrate its capability to describe directional hardening behavior for different two-stage loading paths with and without unloading. Next (§5), we show the potentials of the model with the help of the so called plastic spin which has not been taken into account in Teodosiu and Hu (1998). Lastly (§6), to understand more of the current model, the influence of the numerical parameters for the model is investigated.

---

<sup>1</sup>As discussed in more detail below, note that this quantity is defined here with respect to the *back-rotated* configuration. In contrast, note that the analogous quantities  $\mathbf{N}$  in Teodosiu and Hu (1998) and that  $\mathbf{A}$  in Bouvier et al. (2005) are defined with respect to the *current* configuration.

### 3.2 Review of the Teodosiu and Hu model

The purpose of this section is to briefly review the model for directional hardening originally proposed by Teodosiu and Hu (1995). As mentioned above, this model mainly takes into account the effect of changes in loading direction on the hardening behavior. In its original form, it was developed to describe the following material behavior observed experimentally:

1. Monotonic strain-path. Here, the hardening mechanisms are the same during the pre-loading and the subsequent loading phases. From the microstructural point of view, this type of strain path change results in a continuous reinforcement of the dislocation wall or cell structures. The stress-strain curves after re-loading are identical with those of the monotonic loading case.
2. Bauschinger strain-path change. This represents the case of load reversal. Figure 3.1 shows the material response in the case of a load reversal for mild steel DC06. Besides the usual reduced yield stress after reloading (Bauschinger effect), hardening stagnation is evident. This is assumed to be associated with the annihilation of the dislocation walls created during monotonic pre-loading.

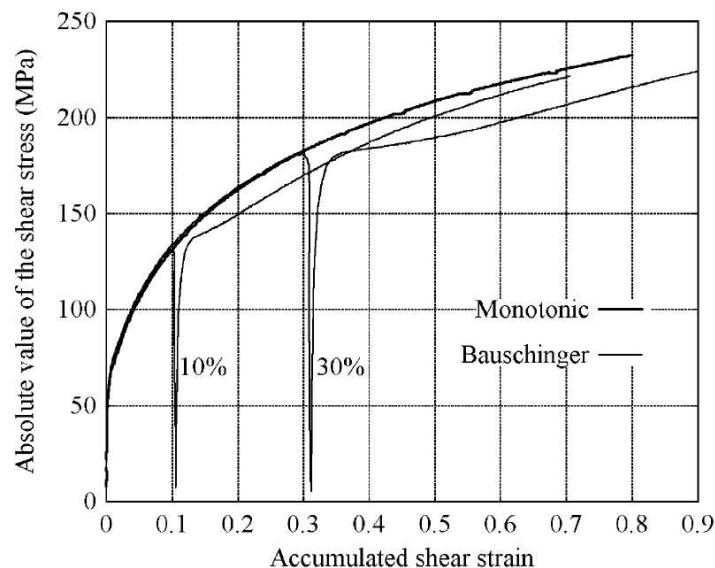


Figure 3.1: Experimental results for the mild steel DC06 subjected to simple shear followed by load reversal (Bouvier et al., 2006).

3. Orthogonal strain-path change. Here, the strain-path changes, *e.g.*, from tension to shear. Figure 3.2 exhibits an increase of the yield stress (cross hardening) after such a strain-path change. This behavior can be explained by the idea that the existing dislocation structures act as obstacles to slip on the newly activated slip systems after the strain-path change. Note in particular the softening observed at the beginning of the second stage. This is attributed to deformation localization in the so-called microbands. In addition, the experiments also show that the softening effect becomes stronger with an increasing

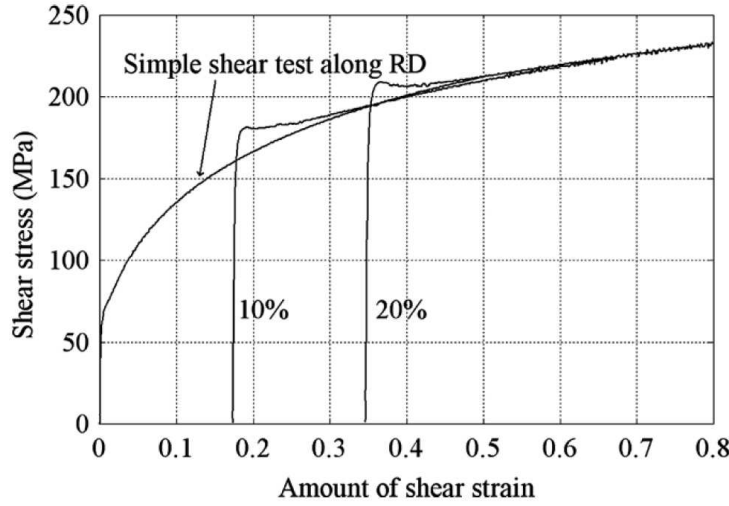


Figure 3.2: Experimental results for DC06 subjected to uniaxial tension followed by simple shear (Bouvier et al., 2006), representing an orthogonal strain-path change.

amount of pre-strain. After softening, further hardening takes place due to the formation of new dislocation walls.

To take into account the effect of hardening stagnation after load reversal and of cross hardening after an orthogonal strain-path change, Teodosiu and Hu (1995) proposed a microstructural material model that is based on a set of four internal variables  $\{r, \mathbf{X}, \mathbf{P}, \mathbf{S}\}$ . Besides isotropic hardening, represented by scalar-valued variable  $r$ , and the kinematic hardening, represented by second-order tensor-valued variable  $\mathbf{X}$ , both having stress dimension, Teodosiu and Hu introduced, additionally, a fourth-order tensor-valued stress-like internal variable  $\mathbf{S}$  and a second-order tensor-valued dimensionless internal variable  $\mathbf{P}$ . The variables  $\mathbf{S}$  and  $\mathbf{P}$  are associated with the directional strength of planar dislocation structures and with their polarity, respectively.

In the context of the incremental inelastic formulation chosen by Teodosiu and Hu (1995), all tensor-valued internal variables to follow, as well as their evolution relations, are defined with respect to a local “back-rotated” configuration whose orientation relative to the current configuration is given by the rotation  $\mathbf{Q}$ . In terms of this, the incremental hypoelastic relations

$$\begin{aligned} \dot{\mathbf{I}} \cdot \dot{\mathbf{K}} &= 3\kappa (\mathbf{I} \cdot \mathbf{D}) , \\ \dot{\mathbf{M}} &= 2\mu \{ \mathbf{Q}^T \text{dev}(\mathbf{D})\mathbf{Q} - \mathbf{D}_P \} , \end{aligned} \quad (3.4)$$

hold for the Kirchhoff<sup>2</sup> stress  $\mathbf{K}$  in the context of the orthogonal split

$$\mathbf{K} = \frac{1}{3} (\mathbf{I} \cdot \mathbf{K}) \mathbf{I} + \text{dev}(\mathbf{K}) \quad (3.5)$$

of  $\mathbf{K}$  into spherical and deviatoric parts, respectively, with

$$\mathbf{M} = \mathbf{Q}^T \text{dev}(\mathbf{K})\mathbf{Q} \quad . \quad (3.6)$$

<sup>2</sup>Note that Teodosiu and Hu (1995) work with the Cauchy stress  $\mathbf{T}$  in their formulation. As is well-known, its approximation by  $\mathbf{K}$  in the case of metals is physically well-justified, and results in a much simpler formulation.

These relations are determined in particular by the continuum deformation rate  $\mathbf{D} = \text{sym}(\mathbf{L})$  and its inelastic counterpart  $\mathbf{D}_p$ , with  $\mathbf{L} = \dot{\mathbf{F}}\mathbf{F}^{-1}$  the velocity gradient, and  $\mathbf{F}$  the deformation gradient. As usual for metals,  $\mathbf{D}_p$  is assumed to satisfy incremental inelastic incompressibility  $\mathbf{I} \cdot \mathbf{D}_p = 0$ . As usual, we also have  $\mathbf{I} \cdot \mathbf{D} \approx 0$ . Here,  $\kappa$  represents the elastic bulk modulus, and  $\mu$  the shear modulus, both with respect to the reference configuration.

Turning next to the inelastic part of the model, this is based on an anisotropic yield function of the form

$$\phi = \sigma_{\text{Hill}}(\mathbf{M} - \mathbf{X}) - \sigma_{y0} - r - f|S| \quad . \quad (3.7)$$

Here,

$$\sigma_{\text{Hill}}(\mathbf{M} - \mathbf{X}) = \sqrt{(\mathbf{M} - \mathbf{X}) \cdot \mathbf{A}_{\text{Hill}}[\mathbf{M} - \mathbf{X}]} \quad (3.8)$$

represents the Hill equivalent stress,  $\mathbf{A}_{\text{Hill}}$  the fourth-order symmetric traceless orthotropic Hill flow anisotropy tensor,  $\sigma_{y0}$  the initial yield stress, and  $f$  a material constant determining the fraction of the dislocation walls strength contributing to isotropic hardening. In the current associated rate-independent context,  $\phi$  determines in particular the plastic deformation rate

$$\mathbf{D}_p = \lambda \mathbf{A}_{\text{Hill}}[\mathbf{N}] \quad (3.9)$$

in terms of the measure

$$\mathbf{N} = \sigma_{\text{Hill}}^{-1}(\mathbf{M} - \mathbf{X}) \quad (3.10)$$

of the direction of the effective flow stress, with  $\lambda$  the plastic multiplier. Again, since  $\mathbf{A}_{\text{Hill}}$  is traceless, note that  $\mathbf{I} \cdot \mathbf{A}_{\text{Hill}}[\mathbf{M} - \mathbf{X}] = 0$  and  $\mathbf{D}_p = \text{dev}(\mathbf{D}_p)$  hold.

Consider next the modeling of hardening in the Teodosiu model. In particular, isotropic hardening  $r$  is determined here by the Voce form

$$\dot{r} = c_r (r_{\text{sat}} - r) \lambda \quad . \quad (3.11)$$

Here,  $r_{\text{sat}}$  represents the saturation value of  $r$  and  $c_r$  controls the saturation rate. Beyond this, the Teodosiu model accounts for the effect of the effective polarity of excess dislocations of the same sign building up at dislocation sheets on the hardening behavior via a second-order symmetric traceless tensor-valued internal variable  $\mathbf{P}$  whose evolution equation is described through

$$\dot{\mathbf{P}} = c_p (\mathbf{A}_p - \mathbf{P}) \lambda \quad (3.12)$$

with material constant  $c_p$  controlling the saturation rate. Turning next to the back stress  $\mathbf{X}$ , its evolution is determined in the Teodosiu model by the non-linear form

$$\dot{\mathbf{X}} = c_x \{x_{\text{sat}} \mathbf{N} - \mathbf{X}\} \lambda \quad (3.13)$$

involving growth and dynamic recovery. Here, the material constant  $c_x$  controls the saturation rate, and the constitutive relation

$$x_{\text{sat}} = x_0 + (1 - f) \sqrt{m|S|^2 + (1 - m)|s^d|^2} \quad (3.14)$$

determines the saturation value of  $\mathbf{X}$ , which is assumed to be influenced by the directional strength of dislocation sheets. In this relation,  $x_0$  represents the initial value of  $x_{\text{sat}}$ ,  $m$  is another

material parameter, whose meaning will become apparent later. The variable  $s^d$  as defined in (3.1) represents the strength of dislocation structures associated with the currently active slip systems. Together with (3.2), it induces the additive orthogonal split

$$\mathbf{S} = s^d \mathbf{A}_p \otimes \mathbf{A}_p + \mathbf{S}^\ell \quad (3.15)$$

of  $\mathbf{S}$ . Here,  $\mathbf{S}^\ell$  represents the strength of dislocation structures associated with latent slip systems. The orthogonality of the decomposition (3.15) implies

$$|\mathbf{S}|^2 = |s^d|^2 + |\mathbf{S}^\ell|^2 \quad . \quad (3.16)$$

On this basis, the expression (3.14) for  $x_{\text{sat}}$  can be rewritten as

$$x_{\text{sat}} = x_0 + (1 - f) \sqrt{|s^d|^2 + m |\mathbf{S}^\ell|^2} \quad . \quad (3.17)$$

Expressed in this form, one sees that values of  $m$  greater than 1 imply that the dislocation structures associated with the latent slip systems contribute more to the evolution of  $x_{\text{sat}}$  than those associated with the currently active slip systems.

The evolution relations in the Teodosiu model are completed by those

$$\begin{aligned} \dot{s}^d &= c_d \{ h_p (s_{\text{sat}} - s^d) - h_x s^d \} \lambda \ , \\ \dot{\mathbf{S}}^\ell &= -c_\ell \{ |\mathbf{S}^\ell|/s_{\text{sat}} \}^{n_\ell} \mathbf{S}^\ell \lambda \ , \end{aligned} \quad (3.18)$$

for  $s^d$  and  $\mathbf{S}^\ell$ , respectively. Here,  $c_\ell$  and  $c_d$  represent material constants controlling the saturation rates of  $\mathbf{S}^\ell$  and  $s^d$ , respectively. Further,  $s_{\text{sat}}$  is the saturation value of  $s^d$ . The exponent  $n_\ell$  determines the influence of prestraining on the evolution of  $\mathbf{S}^\ell$ . The material function  $h_p$  governs the contribution to the evolution of  $s^d$  arising from dislocation polarization processes. The magnitude of these contributions depends in particular on the projection  $\mathbf{A}_p \cdot \mathbf{P}$  of  $\mathbf{P}$  onto  $\mathbf{A}_p$ . Teodosiu and Hu (1995) worked with the form

$$h_p = \begin{cases} 1 - \frac{c_p}{c_d + c_p} \left| \frac{s^d}{s_{\text{sat}}} - \mathbf{A}_p \cdot \mathbf{P} \right| & \text{if } \mathbf{A}_p \cdot \mathbf{P} \geq 0 \\ (1 + \mathbf{A}_p \cdot \mathbf{P})^{n_p} \left\{ 1 - \frac{c_p}{c_d + c_p} \frac{s^d}{s_{\text{sat}}} \right\} & \text{if } \mathbf{A}_p \cdot \mathbf{P} < 0 \end{cases} \quad (3.19)$$

for  $h_p$ . The function  $h_x$  determines the influence of kinematic hardening processes on the development of  $s^d$  and is given as

$$h_x = \frac{1}{2} \left\{ 1 - \frac{1}{x_{\text{sat}}} \frac{\mathbf{A}_p \cdot \mathbf{X}}{\mathbf{A}_p \cdot \mathbf{N}} \right\} \quad . \quad (3.20)$$

Note that it attains non-negligible values only during a microplastic stage. In particular,  $h_x$  accounts for the slight decrease of  $s^d$  as the back stress approaches its saturation value.

Finally, consider the constitutive rotation  $\mathbf{Q}$  defining the local back-rotated configuration with respect to the current configuration. Teodosiu and Hu (1995) chose the local back-rotated Jaumann configuration, in which case

$$\dot{\mathbf{Q}} = \mathbf{W} \mathbf{Q} \quad , \quad (3.21)$$



with  $\mathbf{W} = \text{skw}(\mathbf{L})$  being as usual the continuum spin. As we discuss later, this is reasonable assumption when the initial flow anisotropy is mild and the material symmetry directions (*i.e.*, microstructure elements) effectively rotate with the continuum (in which case the plastic spin  $\mathbf{W}_p$  is zero). More generally, and in the case of significant initial flow anisotropy, this will not in general be the case. Since the evolution of  $\mathbf{Q}$  in this case is determined by  $\mathbf{W}$ ,  $\mathbf{Q}$  represents a dependent constitutive quantity here and not an additional internal variable in the formulation, as we will see in the next section.

The above relations contain a total of 21 material parameters. These include the two elastic constants  $\kappa$  and  $\mu$ , the six Hill anisotropy parameters  $F, G, H, L, M$ , and  $N$  determining  $A_{\text{Hill}}$ , the saturation parameters  $c_p, c_x, c_d, c_\ell$ , and  $c_r$ , as well as the remaining hardening parameters  $\sigma_{y0}, m, x_0, f, r_{\text{sat}}, s_{\text{sat}}, n_\ell$  and  $n_p$ . This completes the model formulation. Next, we turn to algorithmic considerations.

### 3.3 Algorithmic formulation and model behavior

Before discussing the algorithmic formulation, consider briefly first how the model describes the development of hardening behavior during strain-path changes. For example, consider the case of no such change, *i.e.*, monotonic loading. In this case,  $\mathbf{A}_p$  is constant, and (3.12) implies that  $\mathbf{P}$  evolves towards  $\mathbf{A}_p$ . In turn, (3.19) then implies that  $h_p$  decreases gradually from 1. Assuming that  $s^d$  is initially zero, (3.18)<sub>1</sub> then implies that  $s^d$  tends to  $s_{\text{sat}}$ . Likewise, assuming that  $S^\ell$  is initially zero, *i.e.*, that the material initially contains no dislocation structures contributing to directional hardening,  $S^\ell$  remains zero according to (3.18)<sub>2</sub>.

Consider next the case of a load reversal. In this case,  $\mathbf{A}_p \cdot \mathbf{P}$  “jumps” to a value close to  $-1$  for large deformation, and  $h_p$  to one close to  $0$ . According to (3.18)<sub>1</sub>, the last condition corresponds to hardening stagnation. As the strain increases along the reverse direction,  $\mathbf{A}_p \cdot \mathbf{P}$  then increases gradually towards positive values, leading to an increase of  $h_p$  and the resumption of hardening. Lastly, consider an orthogonal strain-path change. In this case, (3.1) implies that  $s^d$  becomes zero, and so  $S^\ell$  becomes equal to  $S$  from (3.15). Further, from (3.14), an orthogonal strain-path change then results in an immediate increase of  $x_{\text{sat}}$  for  $m \geq 1$ . This leads in turn to an accelerated growth of  $\mathbf{X}$  and a cross-hardening effect. In addition, at the start of the orthogonal path, note that (3.18)<sub>2</sub> implies a short stage of softening, while (3.18)<sub>1</sub> leads to a resumption of hardening.

With these observations in hand, we now turn to the numerical integration and solution of the Teodosiu model over a finite time-interval  $[0, d] = \bigcup_{n=0}^{m-1} [t_n, t_{n+1}]$  consisting of of  $m$  disjoint subintervals  $[t_0, t_1], \dots, [t_{m-1}, t_m]$ . Each such subinterval  $[t_n, t_{n+1}]$  is of duration  $t_{n+1, n} = t_{n+1} - t_n$ . As usual, the deformation gradient  $\mathbf{F}_n$ , as well as the values  $\mathbf{Q}_n, \mathbf{K}_n, \mathbf{X}_n, \mathbf{P}_n$ , and  $S_n$ , are all known at the start  $t = t_n$  of this interval from the solution for the last one. Assuming that  $\mathbf{L} = \dot{\mathbf{F}} \mathbf{F}^{-1}$  is approximately constant in the interval  $[t_n, t_{n+1}]$ , exponential backward-Euler integration yields the approximation

$$\mathbf{L}_{n+1, n} := t_{n+1, n} \mathbf{L}_{n+1} = \ln(\mathbf{F}_{n+1, n}) = \mathbf{H}_{n+1, n} - \frac{1}{2} \mathbf{H}_{n+1, n}^2 + \frac{1}{3} \mathbf{H}_{n+1, n}^3 - \dots \quad (3.22)$$

for the incremental velocity gradient in terms of the corresponding relative displacement  $\mathbf{H}_{n+1, n} = \mathbf{F}_{n+1, n} - \mathbf{I}$  and deformation  $\mathbf{F}_{n+1, n} = \mathbf{F}_{n+1} \mathbf{F}_n^{-1}$  gradients. Assuming  $|\mathbf{H}_{n+1, n}| \ll 1$ , this

will be approximated here for algorithmic simplicity by the midpoint form

$$\mathbf{L}_{n+1,n} = \mathbf{H}_{n+1,n} [\mathbf{I} + \frac{1}{2} \mathbf{H}_{n+1,n}]^{-1} = \mathbf{H}_{n+1,n} - \frac{1}{2} \mathbf{H}_{n+1,n}^2 + \frac{1}{4} \mathbf{H}_{n+1,n}^3 - \dots \quad (3.23)$$

In turn,  $\mathbf{L}_{n+1,n}$  determines the measures  $\mathbf{D}_{n+1,n} = \text{sym}(\mathbf{L}_{n+1,n})$  and  $\mathbf{W}_{n+1,n} = \text{skw}(\mathbf{L}_{n+1,n})$  of incremental strain and rotation, respectively. Next, exponential backward-Euler integration of (3.21) yields the algorithmic form

$$\mathbf{Q}_{n+1,n} = \mathbf{Q}_{n+1} \mathbf{Q}_n^T = \exp(\mathbf{W}_{n+1,n}) \quad (3.24)$$

for  $\mathbf{Q}_{n+1}$  which can be evaluated using the Rodrigues formula (*e.g.*, Simo and Hughes, 1998, Chapter 8).

Consider next the numerical time-integration of the Teodosiu model as discussed in the last section. Backward-Euler integration of these relations over  $[t_n, t_{n+1}]$  yields the system

$$\begin{aligned} \mathbf{M}_{n+1} &= \mathbf{M}_n + 2\mu \left\{ \mathbf{Q}_{n+1}^T \text{dev}(\mathbf{D}_{n+1,n}) \mathbf{Q}_{n+1} - \mathbf{A}_{\text{Hill}}[\mathbf{N}_{n+1}] \epsilon_{n+1,n} \right\}, \\ r_{n+1} &= r_n + c_r (r_{\text{sat}} - r_{n+1}) \epsilon_{n+1,n}, \\ \mathbf{X}_{n+1} &= \mathbf{X}_n + c_x \left\{ x_{\text{sat } n+1} \mathbf{N}_{n+1} - \mathbf{X}_{n+1} \right\} \epsilon_{n+1,n}, \\ \mathbf{P}_{n+1} &= \mathbf{P}_n + c_p \left\{ \mathbf{A}_{\text{P } n+1} - \mathbf{P}_{n+1} \right\} \epsilon_{n+1,n}, \\ s_{n+1}^d &= s_n^d + c_d \left[ h_{\text{p } n+1} (s_{\text{sat}} - s_{n+1}^d) - h_{\text{x } n+1} s_{n+1}^d \right] \epsilon_{n+1,n}, \\ \mathbf{S}_{n+1}^\ell &= \mathbf{S}_n^\ell - c_\ell \left\{ |\mathbf{S}_{n+1}^\ell| / s_{\text{sat}} \right\}^{n_\ell} \mathbf{S}_{n+1}^\ell \epsilon_{n+1,n}, \end{aligned} \quad (3.25)$$

together with the Karesh-Kuhn-Tucker condition  $\epsilon_{n+1,n} \phi_{n+1} = 0$  determining the incremental plastic multiplier  $\epsilon_{n+1,n} := t_{n+1,n} \lambda_{n+1}$  in the current rate-independent context. In particular, solution of this system yields the current value

$$\mathbf{S}_{n+1} = s_{n+1}^d \mathbf{A}_{\text{P } n+1} \otimes \mathbf{A}_{\text{P } n+1} + \mathbf{S}_{n+1}^\ell \quad (3.26)$$

of  $\mathbf{S}$  from (3.2). Note that the backward-Euler system (3.25) has been obtained on the premise that the variables involved vary *continuously* over the time interval  $[t_n, t_{n+1}]$ . In addition, the standard incremental procedure to the solution of internal variable systems over an entire time interval  $[0, d] = \bigcup_{n=0}^{m-1} [t_n, t_{n+1}]$  is based on the premise of piecewise-continuity of these variables in this interval (*e.g.*, Simo and Hughes, 1998). On the other hand, as is implied by the Teodosiu model, strain-path changes may lead in general to jumps in the values of  $s^d$  and  $\mathbf{S}^\ell$  between intervals of continuous change. Such possible jumps in the values of these variables are neither accounted for in the notation nor in the algorithmic formulation presented up to this point. In fact, to this end, it is useful to generalize the notation slightly. This is based on the correspondences  $s(n) \equiv t_n$ ,  $e(n) \equiv t_{n+1}$ , and  $[t_n, t_{n+1}] \equiv [s(n), e(n)]$ . Consequently,  $s(n)$  represent the start of the  $n^{\text{th}}$  time interval, and  $e(n)$  its end. In terms of this notation, we can rewrite (3.25)<sub>4,5</sub> in the form

$$\begin{aligned} s_{e(n)}^d &= s_{s(n)}^d + c_d \left\{ h_{\text{p } e(n)} (s_{\text{sat}} - s_{e(n)}^d) - h_{\text{x } e(n)} s_{e(n)}^d \right\} \epsilon_{e(n), s(n)}, \\ \mathbf{S}_{e(n)}^\ell &= \mathbf{S}_{s(n)}^\ell - c_\ell \left\{ |\mathbf{S}_{e(n)}^\ell| / s_{\text{sat}} \right\}^{n_\ell} \mathbf{S}_{e(n)}^\ell \epsilon_{e(n), s(n)}. \end{aligned} \quad (3.27)$$

In particular, this notation allows us for example to clearly distinguish between the value  $s_{s(n)}^d$  of  $s^d$  at start  $s(n)$  of the  $n^{\text{th}}$  time interval  $[s(n), e(n)]$  and its value  $s_{e(n-1)}^d$  at the end  $e(n-1)$  of

the previous time interval  $[s(n-1), e(n-1)]$ . In the standard notation, there is no distinction, *i.e.*,  $s_n^d = s_n^d$ ! In other words, the standard notation is tacitly based on the assumption the processes involved are (at least piecewise) continuous. As we have just discussed, however, strain-path changes between two “standard” continuous processes may result in  $s_{s(n)}^d \neq s_{e(n-1)}^d$  and  $S_{s(n)}^\ell \neq S_{e(n-1)}^\ell$ . In this case, the formulation up to this point is incomplete. Indeed, the question is then, how is  $s_{s(n)}^d$  related to  $s_{e(n-1)}^d$ , and likewise, how is  $S_{s(n)}^\ell$  related to  $S_{e(n-1)}^\ell$ ? To document the behavior of the algorithm for various cases here and in what follows, we use the material parameter values for IF steel DC06 from Bouvier et al. (2003) given in Table 3.1. As

parameter	value	units
$\kappa$	158333	MPa
$\mu$	73077	MPa
$\sigma_{Y0}$	121.1	MPa
$x_0$	15.9	MPa
$r_{\text{sat}}$	90.0	MPa
$s_{\text{sat}}$	231.1	MPa

parameter	value
$c_p$	5.5
$c_x$	446.0
$c_d$	4.0
$c_\ell$	1.86
$c_r$	31.9
$m$	1.5
$f$	0.445
$n_\ell$	0.0
$n_p$	27.9

Table 3.1: Material parameter values for DC06 (Bouvier et al., 2003).

is pointed out in Bouvier et al. (2003), this material exhibits significant cross-hardening as well as subsequent softening after an orthogonal strain-path change.

In the context of the current notation, the following discussion is based on the relations

$$\begin{aligned}
 S_{e(n-1)} &= s_{e(n-1)}^d \mathbf{A}_{Pe(n-1)} \otimes \mathbf{A}_{Pe(n-1)} + S_{e(n-1)}^\ell, \\
 s_{s(n)}^d &= \mathbf{A}_{Pi} \cdot S_{e(n-1)} [\mathbf{A}_{Pi}], \\
 S_{s(n)}^\ell &= S_{e(n-1)} - s_{s(n)}^d \mathbf{A}_{Pi} \otimes \mathbf{A}_{Pi},
 \end{aligned} \tag{3.28}$$

for the transition from the  $(n-1)^{\text{th}}$  to the  $n^{\text{th}}$  time step, where  $\mathbf{A}_{Pi}$  represents some discrete value of  $\mathbf{A}_p$ . The first of these is just (3.26) re-expressed in the current notation. On this basis, consider the simplest case, *i.e.*, monotonic loading. Here,  $\mathbf{A}_p$  is constant (*e.g.*, simple tension) or varies continuously (*e.g.*, simple shear). Assume now that  $S_{s(0)}$ , and so  $s_{s(0)}^d$  as well as  $S_{s(0)}^\ell$ , are zero. For the case of simple tension,  $\mathbf{A}_p$  is constant, and we can set  $\mathbf{A}_{Pi} \equiv \mathbf{A}_{Pe(n-1)}$  (note that  $\mathbf{A}_p$  is single-valued in each interval). In this case, (3.27)<sub>1</sub> implies that  $s^d$  will grow, and (3.27)<sub>2</sub> that  $S^\ell$  will remain zero. On the other hand, in the case of a simple shear,  $\mathbf{A}_p$  is no longer constant, and we have a continuous strain-path change. If we choose  $\mathbf{A}_{Pi} \equiv \mathbf{A}_{Pe(n-1)}$  as before,  $S^\ell$  will remain zero, as before. Choosing alternatively  $\mathbf{A}_{Pi} \equiv \mathbf{A}_{Ps(n)}$ , (3.28) yields

$$\begin{aligned}
 s_{s(n)}^d &= s_{e(n-1)}^d (\mathbf{A}_{Ps(n)} \cdot \mathbf{A}_{Pe(n-1)})^2 + \mathbf{A}_{Ps(n)} \cdot S_{e(n-1)}^\ell [\mathbf{A}_{Ps(n)}], \\
 S_{s(n)}^\ell &= s_{e(n-1)}^d \mathbf{A}_{Pe(n-1)} \otimes \mathbf{A}_{Pe(n-1)} - s_{s(n)}^d \mathbf{A}_{Ps(n)} \otimes \mathbf{A}_{Ps(n)} + S_{e(n-1)}^\ell.
 \end{aligned} \tag{3.29}$$

Consequently, even if  $S_{e(n-1)}^\ell$  is zero,  $S_{s(n)}^\ell$  will not be zero here. So, if we have some reason to believe that a continuous strain-path change should result in the development of latent hardening effects in the form of a non-trivial  $S^\ell$ , the choice  $\mathbf{A}_{Pi} \equiv \mathbf{A}_{Ps(n)}$  is relevant.

With this insight in hand, consider next the case of uniaxial tension followed by simple shear, where the strain-path change is either (i) continuous, or (ii), separated by unloading into the elastic, and reloading into the inelastic, range. As shown in Figure 3.3, in the context of the choice  $\mathbf{A}_{P_i} \equiv \mathbf{A}_{P_{e(n-1)}}$ ,  $S^\ell$  remains zero throughout the process without unloading.

This corresponds to the algorithm of Hoferlin (2001); Montleau (2004) for this case, who

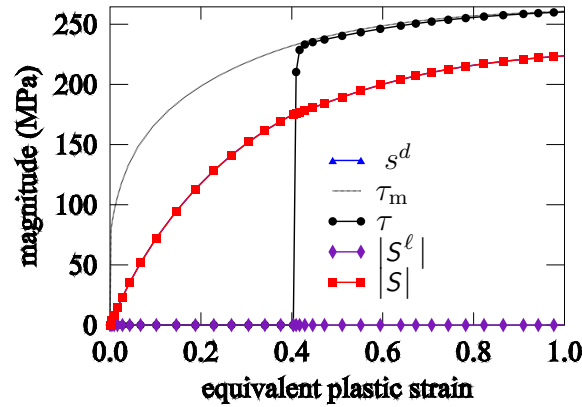


Figure 3.3: Predicted material response of DC06 obtained for the algorithm of Hoferlin (2001) in a tension-shear orthogonal loading-path change at 40% effective plastic strain without unloading. Here,  $\tau_m$  represents the monotonic shear stress and  $\tau$  the shear stress during strain path change. They both are the component of  $K_{12}$  of  $\mathbf{K}$  and they have the same meaning in what follows.

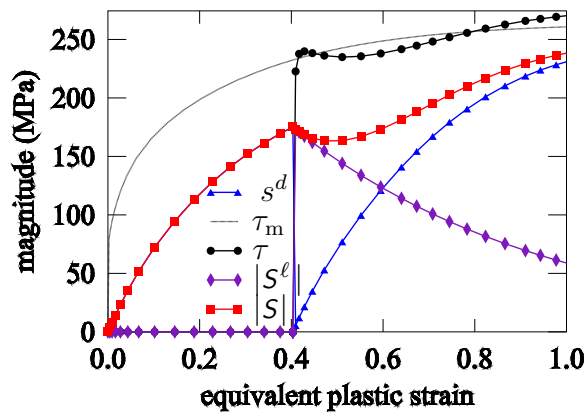


Figure 3.4: Predicted material response of DC06 obtained from the algorithm of Hoferlin (2001) for a tension-shear orthogonal loading-path change at 40% effective plastic strain with unloading. Curves are the same as in Figure 3.3.

implemented the Teodosiu model into the finite-element programs Lagamine and ABAQUS. Generalizing now to the case with unloading, Hoferlin (2001) determined the initial inelastic state at reloading using the condition  $\mathbf{A}_{P_i} \equiv \mathbf{A}_{P_{s(n)}}$ ; otherwise, he used  $\mathbf{A}_{P_i} \equiv \mathbf{A}_{P_{e(n-1)}}$ . This results in the cross-hardening behavior shown in Figure 3.4. Note that the only difference

between the processes with and without unloading consists in how one switches from tension to simple shear. Since in the case without unloading, this switch is very "fast" (only a small amount of plastic strain is accumulated during the transition), both cases remain comparable. From the physical point of view, the amount of accumulated plastic strain during the transition is too small to destroy the dislocation structures developed during the preceding uniaxial-tension stage. Consequently, it does not affect the cross hardening behavior after the strain-path change. From this point of view, it doesn't seem physically reasonable to obtain completely different behavior in the two cases.

Such is not the case, for example, in the algorithm of Balan (see Montleau, 2004). Indeed, he worked with the choice  $\mathbf{A}_{P_i} \equiv \mathbf{A}_{P_{s(n)}}$  for all cases. More recently, in a paper coauthored by Teodosiu, Haddadi et al. (2006) discussed the evolution of the variables  $S$ ,  $s^d$  and  $S^\ell$  for processes with both constant and variable  $\mathbf{A}_P$ . Their discussion seems to imply the use of Balan algorithm, *i.e.*, except for the behavior of  $S^\ell$  in (monotonic) simple-shear loading. Indeed, since  $\mathbf{A}_P$  does not remain constant during such loading, Balan's approach predicts an evolution of  $S^\ell$ . On the other hand, Montleau (2004) reports that Teodosiu is of the opinion that  $S^\ell$  should remain zero during a monotonic simple shear process. In addition, the Teodosiu-model-based simulation results shown in Figure 13 of Bouvier et al. (2005) indicate no evolution of  $S^\ell$  in such a process. This state of affairs has motivated us to formulate an alternative model for the evolution of  $S$  which avoids these algorithmic ambiguities. This is the subject of the next section.

### 3.4 Alternative model for directional hardening

The formulation here is based on the inelastic multiplicative decomposition, plastic incompressibility, and small elastic strain. In the context of the modeling of local inelastic deformation as a change of local reference configuration (Svendsen, 2001), this results in the incremental context in a generalization of (3.4)<sub>2</sub> to the form

$$\dot{\mathbf{M}} = 2\mu \{ \mathbf{R}_E^T \text{dev}(\mathbf{D}) \mathbf{R}_E - \mathbf{D}_P \} \quad . \quad (3.30)$$

Here,  $\mathbf{R}_E$  represents the local rotation of the intermediate configuration with respect to the current configuration, with evolution equation

$$\dot{\mathbf{R}}_E = \mathbf{W} \mathbf{R}_E - \mathbf{R}_E \mathbf{W}_P \quad (3.31)$$

determined in particular by the plastic spin  $\mathbf{W}_P$ . This latter form reduces to (3.21) when  $\mathbf{W}_P$  is assumed negligible. Further, we now have

$$\mathbf{M} = \mathbf{R}_E^T \text{dev}(\mathbf{K}) \mathbf{R}_E \quad (3.32)$$

analogous to (3.6). Beyond this, the current model is based on the modeling of  $S$  as a standard internal variable. In particular, such variables evolve only in the inelastic regime. This alternative model for  $S$  is based on the constitutive relation

$$\dot{S} = c_d [h_p (s_{\text{sat}} - s^d) - h_x s^d] \lambda \mathbf{A}_P \otimes \mathbf{A}_P - c_\ell \{ |S^\ell| / s_{\text{sat}} \}^{n_\ell} S^\ell \lambda \quad (3.33)$$

for the evolution of  $S$  in the back-rotated frame. Here,  $s^d$  is given as a function of  $S$  by (3.1), and  $S^\ell$  as such a function by (3.2). To compare this with the Teodosiu model, consider the equivalent expression

$$\begin{aligned}\dot{S} &= \dot{s}^d \mathbf{A}_P \otimes \mathbf{A}_P + s^d \overline{\dot{\mathbf{A}}_P \otimes \mathbf{A}_P} + \dot{S}^\ell \\ &= c_d \{h_p (s_{\text{sat}} - s^d) - h_x s^d\} \mathbf{A}_P \otimes \mathbf{A}_P \lambda - c_\ell \{|S^\ell|/s_{\text{sat}}\}^{n_\ell} S^\ell \lambda + s^d \overline{\dot{\mathbf{A}}_P \otimes \mathbf{A}_P}\end{aligned}\quad (3.34)$$

for  $\dot{S}$  following from (3.1), (3.2) and (3.18). Comparing (3.33) and (3.34), we see that these differ by the term  $s^d \overline{\dot{\mathbf{A}}_P \otimes \mathbf{A}_P}$ . These two expressions for  $\dot{S}$  are then equivalent only when  $\mathbf{A}_P$  is constant. Otherwise, the directional hardening described by the current ansatz (3.33) will differ from the model of Teodosiu. In particular, this is the case for monotonic simple shear. As we saw above, in this case,  $\mathbf{A}_P$  varies continuously. As shown by the results in Figure 3.5, the current model predicts that  $S$  evolves in such a way that  $S^\ell$  becomes non-zero, even if  $S$  is initially zero. Note that  $\mathbf{W}_P$  has been neglected for simplicity.

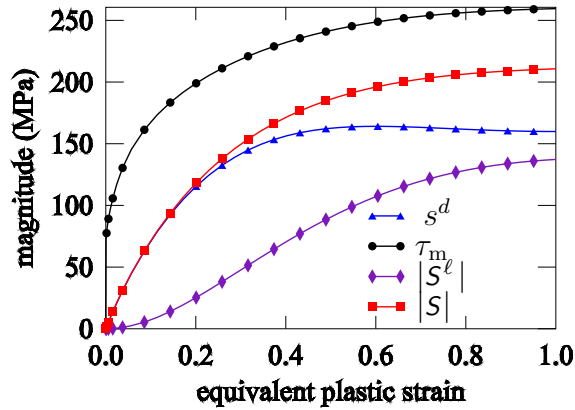


Figure 3.5: Hardening response of DC06 on the basis of (3.33) during monotonic simple-shear assuming  $\mathbf{W}_P$  negligible.

That the current approach predicts an evolution of  $S^\ell$  in the simple shear case is simply a consequence of the fact that  $S$  does not become coaxial with  $\mathbf{A}_P \otimes \mathbf{A}_P$  in the case of continuously changing  $\mathbf{A}_P$  (*i.e.*, with respect to the back-rotated frame). This is, for example, also the case for the back stress which does not become coaxial with  $\mathbf{A}_P$ , or with the effective stress (difference between the applied stress and the back stress) as in the Teodosiu model, in the case of simple shear. A possible microstructural explanation for the evolution of  $S^\ell$  in simple shear associated with the strength of latent slip systems is that strong rotation in individual grains may lead to activation of new slip systems and the deactivation of initially-active ones. These latter then become latent in the course of further deformation and contribute to the development of  $S^\ell$ .

Consider now the behavior of the current model, and in particular its ability, like the Teodosiu model to capture the hardening stagnation after a load reversal, as well as the cross hardening after an orthogonal strain-path changes. To this end, consider a simple shear test with load reversal as well as an orthogonal test (uniaxial tension followed by simple shear) with and

without unloading. For simplicity and comparability with the Teodosiu model,  $\mathbf{W}_p$  is assumed negligible for the moment. We again use the material parameters for DC06 listed in Table 3.1.

Figure 3.6 shows the simulation results for a simple shear test with load-reversal after 30% of shear pre-strain. The shear stress curve reveals a pronounced Bauschinger effect and a dis-

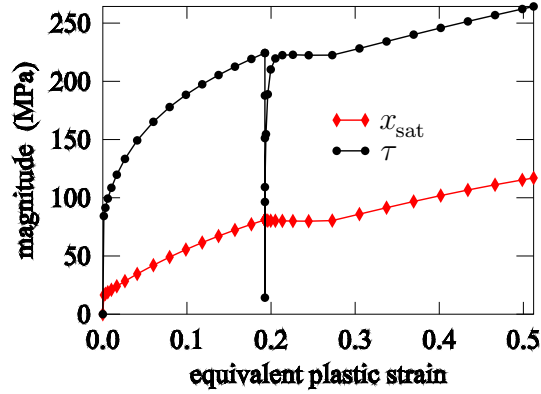


Figure 3.6: Hardening response of DC06 on the basis of (3.33) during reverse simple-shear loading neglecting  $\mathbf{W}_p$ .

tinct area of hardening stagnation after the load reversal. The ability of the model to describe the Bauschinger effect is due to the usage of kinematic hardening. The diagram also shows the evolution of the saturation value  $x_{\text{sat}}$  for kinematic hardening. After continuously increasing during pre-loading,  $x_{\text{sat}}$  decreases slightly immediately after load reversal, becomes approximately constant, and then begins to increase in the course of further loading along the reversed path. Such an evolution of  $x_{\text{sat}}$  is responsible for the hardening stagnation.

Finally, in the case of an orthogonal strain-path change, consider the evolution of  $S$ ,  $s^d$  and  $S^\ell$  with and without unloading. As shown in Figure 3.7 (above), the value of the norm of  $S^\ell$  with unloading remains zero during the first deformation stage and then jumps to a finite value after the strain-path change. In contrast, the value of  $s^d$  increases continuously during the first stage and then drops to zero at the beginning of the subsequent strain path. Such behavior of  $s^d$  and  $S^\ell$  immediately after the strain-path change leads to cross hardening via (3.17) for  $m > 1$ . At the beginning of the second stage,  $S^\ell$  decreases more rapidly than  $s^d$  increases. This results in a short softening stage followed by hardening. Similar behavior is observed for these variables in the case without unloading (Figure 3.7, below). The only difference is that  $s^d$  and  $S^\ell$  don't jump as in the case with unloading but change their values continuously. Since the change in  $\mathbf{A}_p$  is sufficiently fast, we obtain almost identical results for the evolution of the shear stress in the second stage.

The simulations of orthogonal strain-path changes up to this point have considered simple tension followed by simple shear. On this basis, it has been shown that  $S^\ell$  evolves during the shear stage but not during tension. Consider now the reverse order, *i.e.*, simple shear followed by simple tension. Figure 3.8 shows the corresponding material response. As in the tension-shear case, the model predicts a cross-hardening effect. However, there are still differences

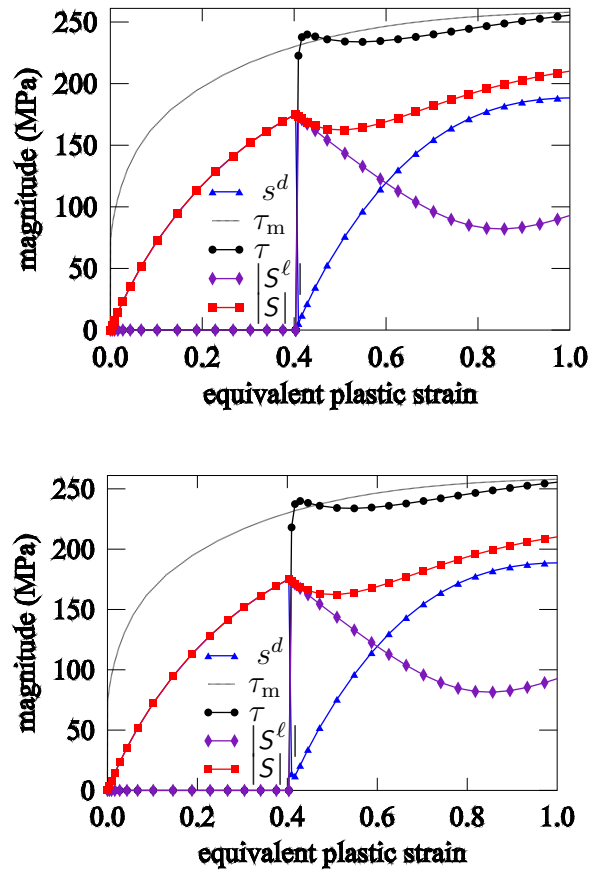


Figure 3.7: Comparison of hardening behavior results for DC06 obtained using the current model as based on (3.33) for a tension-shear orthogonal loading-path change with (above) and without (below) unloading assuming  $W_p$  negligible. Curves are the same as in Figure 3.3.

between this case and the tension-shear orthogonal strain-path change. In tension-shear case, the values of  $s^d$  and the norm of  $S^\ell$  switches after the strain path change. But in the shear-tension case, we note that even  $S^\ell$  has nonzero value before the strain path change, the value of its norm is smaller than  $s^d$ . From the mathematic point of view, considering the definition of  $s^d$  and  $S^\ell$  from (3.15) and (3.16), it is easy to have the conclusion that if the value of  $s^d$  is larger than the norm of  $S^\ell$  before the orthogonal strain path change, then the new value of  $s^d$  after strain path change should be smaller than the new value of the norm of  $S^\ell$  (the proving is omitted here). If the material parameter  $m$  is larger than 1.0, we can see this would lead to cross hardening due to the increasing the value of  $x_{\text{sat}}$  according to (3.17). This is the reason why the cross hardening can be also reproduced for this orthogonal sequence.

### 3.5 Initial flow anisotropy and plastic spin

Up to this point, we have been discussing cases where effects such as an initial flow anisotropy or rotation of the microstructure relative to the continuum is of second-order importance in comparison to the effect of directional hardening. For completeness, we now look briefly at these effects. As already mentioned above in the context of the Jaumann form (3.21) for the



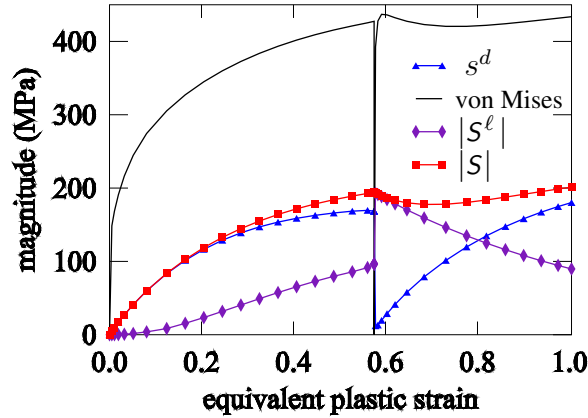


Figure 3.8: Material response in the simple shear-tension orthogonal test with unloading assuming  $\mathbf{W}_P$  negligible.

local back-rotated constitutive configuration, this choice tacitly assumes that there is no relative rotation of the material symmetry axes (*i.e.*, microstructure) relative to the continuum. In previous work (Wang et al., 2005a), it was shown that there is no significant difference between the Jaumann and Green-Naghdi choices in the context of the Teodosiu model for deformation up to about 100%. Again, the choice of either of these implies that the material symmetry directions for anisotropic inelastic flow are rotating in some sense with the continuum, *e.g.*, not relative to it. More generally, however, there will be such a net rotation, and the plastic spin  $\mathbf{W}_P$  is no longer negligible. Indeed, as pointed out by Dafalias (1985, 1998), the rotation of the material symmetry directions of the microstructure with respect to the current configuration as embodied in a non-zero value of  $\mathbf{W}_P$  is in general significant and has actually been observed in experiments (Dafalias, 2000). Following, *e.g.*, Dafalias (1998), assume that this relative rotation is driven by the non-coaxiality between the inelastic deformation rate and effective flow stress. In this case, we have

$$\mathbf{W}_P = \eta (\mathbf{D}_P \mathbf{N} - \mathbf{N} \mathbf{D}_P) = \eta \{A_{\text{Hill}}[\mathbf{N}] \mathbf{N} - \mathbf{N} A_{\text{Hill}}[\mathbf{N}]\} \lambda \quad (3.35)$$

for the plastic spin via (3.9) in terms of the direction  $\mathbf{N}$  of the effective flow stress from (3.10) and the material coefficient  $\eta$ . Note that in the isotropic case  $A_{\text{Hill}} = \frac{3}{2} \text{dev}$ , the plastic spin vanishes. In contrast to the Jaumann case (3.21) (or to the Green-Naghdi case), note that  $\mathbf{R}_E$  and (3.31) now depend on the stress state via  $\mathbf{W}_P$  and (3.35). As such, it becomes an independent internal variable in the formulation.

To investigate the effect of initial flow anisotropy and resultant plastic spin on the hardening behavior, consider again the case of monotonic simple shear. In particular, assume an initial flow anisotropy of Hill-type. For the material DC06, we have  $F = 0.243$ ,  $G = 0.297$ ,  $H = 0.703$  and  $N = 1.2$  from Bouvier et al. (2003). The corresponding stress response up to 200% shear for  $\eta = 0$  and for  $\eta = 10$  is shown in Figure 3.9 and Figure 3.10, respectively. These results can be compared with the analogous results for the case of initial flow isotropy in Figure 3.5. Recall that the growth of  $S^\ell$  in this case was due to changing orientation of the back-rotated configuration with respect to the shear direction. The case in Figure 3.9, corresponding to the case of the

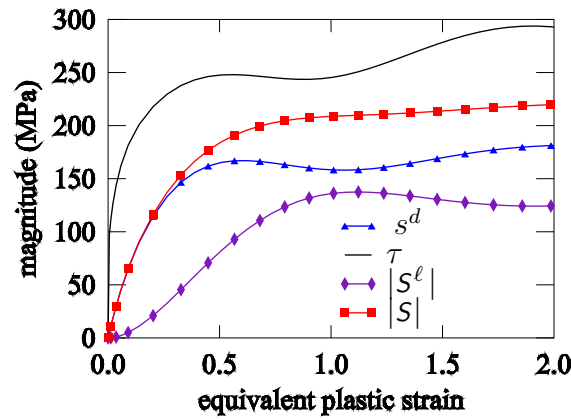


Figure 3.9: Simple shear test using current model with initial flow anisotropy,  $\eta = 0$ .

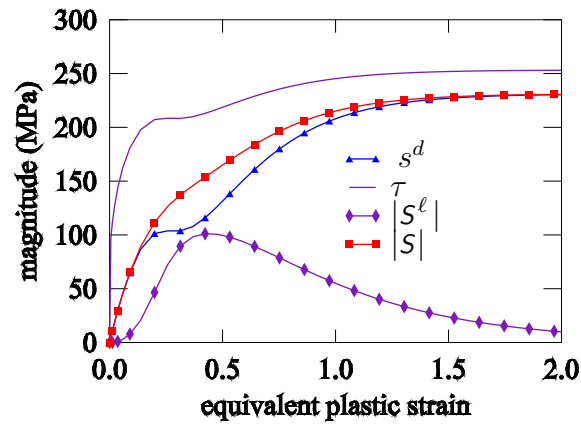


Figure 3.10: Simple shear test using current model with initial flow anisotropy,  $\eta = 10$ .

Jaumann rate together with kinematic hardening, shows that well-known stress oscillations in that case also affect the evolution of  $S^d$  and  $S^\ell$ . Because these are required to remain orthogonal to each other, their “sum” in the form of  $S^\ell$  is less affected by this behavior. In contrast, the results in Figure 3.10 show that activation of the plastic spin results in smooth behavior. More importantly, the fact that in this case the material symmetry (*i.e.*, microstructural) directions are able to rotate with respect to the continuum results in an accelerated saturation and breakdown of  $S^\ell$ , *i.e.*, of the planar dislocation structures responsible for directional hardening.

### 3.6 Influence of material parameters

For completeness, consider finally the influence of varying the parameter values on the constitutive response. In particular, the current model contains of course as a special case standard isotropic-kinematic hardening behavior, obtained when  $c_p$ ,  $c_d$ ,  $c_\ell$ ,  $f$ ,  $n_\ell$  and  $n_p$  are all zero, and  $m$  is equal to 1. This will be our starting point for the following investigation in which attention is focused mainly on directional hardening. As typical values for these, we continue to work with the parameter values for DC06 from Table 3.1.

To begin, consider varying  $s_{\text{sat}}$  and  $c_d$ . Note that activating these alone results no cross hardening after an orthogonal strain-path change and no hardening stagnation after a load reversal. The reason for this is that, according to (3.14),  $m = 1$  will result in the same value of  $x_{\text{sat}}$  after an orthogonal strain-path change and, according to (3.12),  $c_p = 0$  in the non-evolution of  $\mathbf{P}$  and, consequently, in  $h_p \equiv 1$ . Since  $c_\ell$  is equal to zero, (3.33) degenerates to an evolution equation for  $\mathcal{S}_d$  (here,  $\mathcal{S}_d = s^d \mathbf{A}_P \otimes \mathbf{A}_P$ ) of the Armstrong-Frederick form, with  $s_{\text{sat}}$  and  $c_d$  being the saturation value and saturation rate, respectively. An evolution of  $\mathcal{S}_d$  will result in an increase of  $x_{\text{sat}}$  via 3.14 and, consequently, in an increase of the stress level in a monotonic process as well as in an increase of the Bauschinger effect after a load reversal. The influence of different values of  $s_{\text{sat}}$  and  $c_d$  on the stress response in monotonic and reversed loading are shown in Figures 3.11 and Figure 3.12, respectively. Activation of  $c_p$  and  $n_p$  results in an

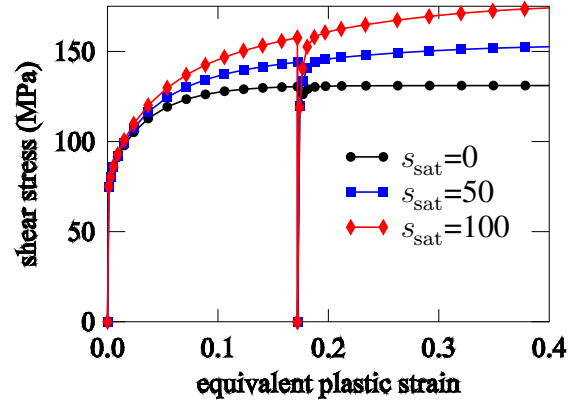


Figure 3.11: Model behavior for different values of  $s_{\text{sat}}$  during load reversal.

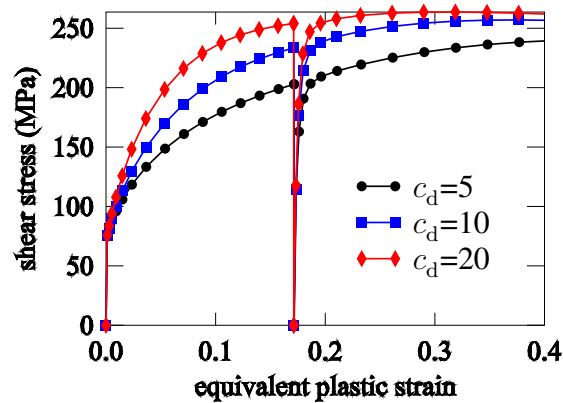


Figure 3.12: Model behavior for different values of  $c_d$  during load reversal.

evolution of  $\mathbf{P}$ . Consequently,  $h_p$  is activated as well, resulting in hardening stagnation after a load reversal. As shown in Figure 3.13, an increase in  $c_p$  reduces the level of hardening in this sense. An increase in the value of  $n_p$  leads to a more pronounced effect of hardening

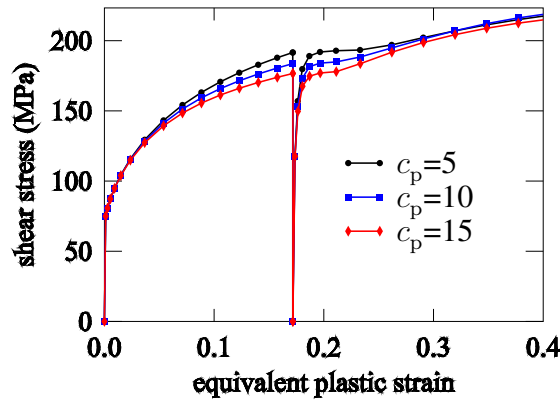


Figure 3.13: Model behavior for different values of  $c_p$  during load reversal.

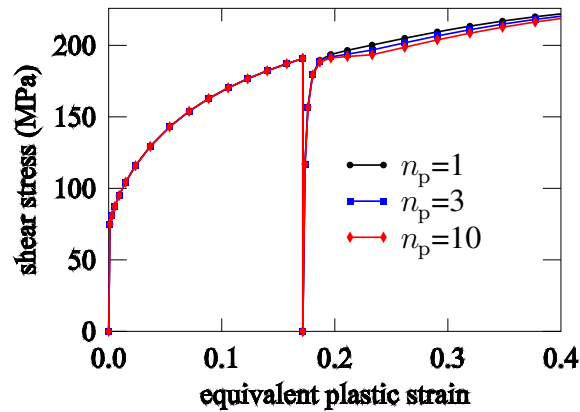


Figure 3.14: Model behavior for different values of  $n_p$  during load reversal.

stagnation, as shown in Figure 3.14.

Consider next  $m$ ,  $c_\ell$  and  $n_\ell$ . Since the influence of these parameters on monotonic and reversed loading is marginal, consider an orthogonal strain-path change from tension to simple shear. The parameter  $m$  describes via (3.14) the amount of the cross hardening/softening effect. While for  $m$  values between 0 and 1 (3.14) will lead to a reduction of  $x_{\text{sat}}$  after an orthogonal strain-path change and, thus, to a cross softening.  $m$  values larger than 1 will result in cross hardening (Figure 3.15). Activation of  $c_\ell$  will result in a decay of  $S^\ell$  after an orthogonal strain-path change via (3.33) and, consequently, in a reduction of  $x_{\text{sat}}$  via (3.14), which will in turn lead to a short stage of work-softening as shown in Figure 3.16. In addition, the figure shows that the larger  $c_\ell$ , the steeper the softening is. The parameter  $n_\ell$  has a similar effect. Since the expression  $|S^\ell|/s_{\text{sat}}$  in (3.33) cannot be larger than one, raising it to the power of  $n_\ell$  will reduce its value and, thus, lead to a reduction of the softening rate of  $S^\ell$ . Accordingly, as shown by Figure 3.17, the larger the value of  $n_\ell$ , the less steeper the work-softening is. In this figure, a higher value of  $c_\ell$  (equal to 10) is used to show more pronounced softening effect instead of using the corresponding value from DC06.

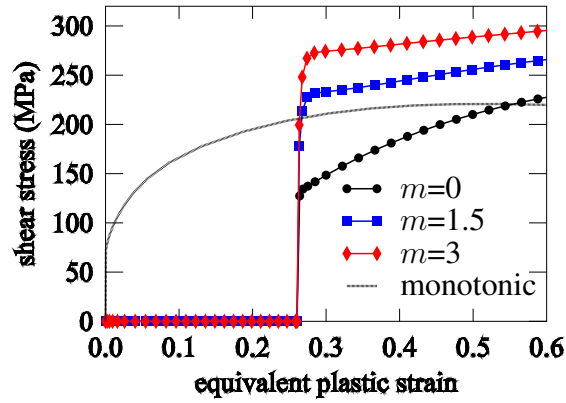


Figure 3.15: Model behavior for different values of  $m$  in tension-shear loading. Here, Monotonic shear stress response using  $m = 0$  is presented for reference.

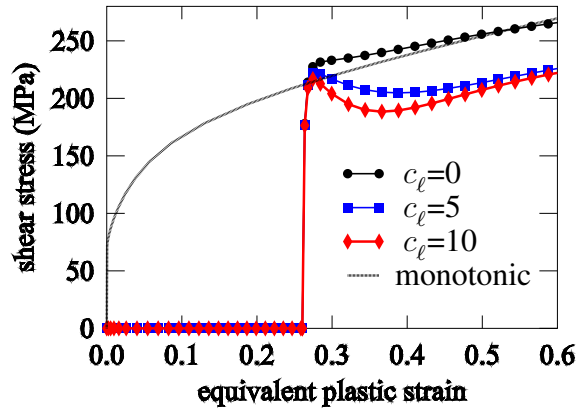


Figure 3.16: Model behavior for different values of  $c_\ell$  in tension-shear loading. Here, Monotonic shear stress response using  $c_\ell = 0$  is presented for reference.

Finally, consider the influence of  $f$  on the stress response. The corresponding results are shown in Figure 3.18. Recall that  $f$  determines the fraction of  $|S|$  contributing to isotropic hardening. Accordingly, for  $f$  being equal to one there will be no cross hardening effect and for  $f = 0$  the cross hardening effect will be the highest due to (3.14).

### 3.7 Conclusions

In this work, a phenomenological model for directional hardening effects in metals subject to non-proportional loading has been formulated and compared in detail to the existing model of Teodosiu and Hu (1998). A detailed discussion of the formulation and numerical implementation of the two models documented their similarities and differences. As shown in detail in this work, the major difference between the two models consists in their behavior during (i) monotonic shear loading and (ii) continuous strain-path changes. The development of directional hardening effects during simple shear processes predicted by the current model is due to relative rotation of the microstructure and corresponding material symmetry directions with

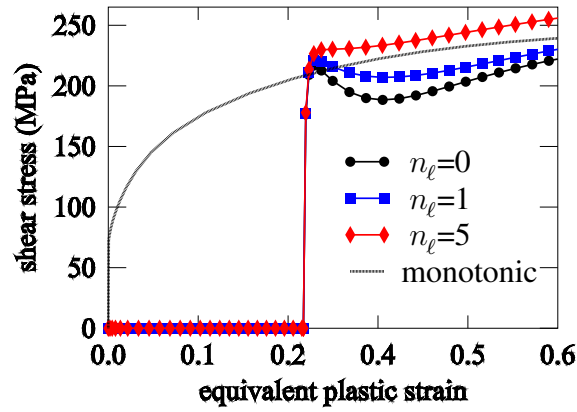


Figure 3.17: Model behavior for different values of  $n_\ell$  in tension-shear loading. Here, Monotonic shear stress response using  $n_\ell = 0$  is presented for reference.

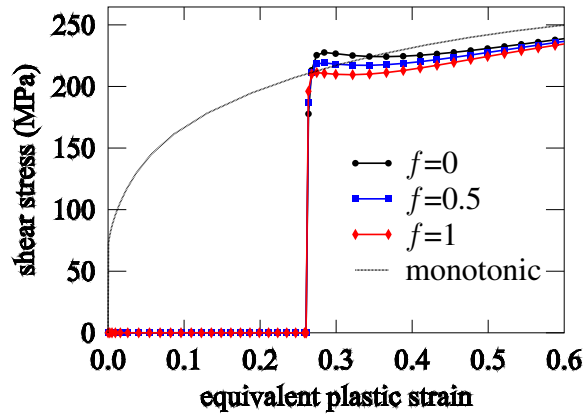


Figure 3.18: Model behavior for different values of  $f$  in tension-shear loading. Here, Monotonic shear stress response using  $f = 0$  is presented for reference.

respect to the continuum, something not predicted by the Teodosiu model. Indeed, in contrast to the Teodosiu model, the current model as based on (3.33) predicts a development of latent directional hardening  $S^\ell$  during simple shear due to continual reorientation of glide systems relative to the loading direction. As shown by the results in Figure 3.5, the current model predicts that  $S$  evolves in such a way that  $S^\ell$  becomes non-zero, even if  $S$  is initially zero. The consequences of this behavior for the modeling and simulation of sheet metal forming processes and springback represent work in progress, and will be reported on elsewhere.

## Chapter 4

# Application of directional hardening modeling to the simulation of sheet metal forming and springback\*

**Abstract** – Springback is a common phenomenon in sheet-metal forming, caused by the release of stored energy in the material during unloading. To accurately predict springback, it is essential to work with a model in which the effects of complex non-proportional loading path changes on the material microstructure and material behavior are taken into consideration. To this end, the micromechanically-based phenomenological model of Wang et al. (2006d) for isotropic, kinematic and directional hardening effects in metals is applied to the modeling and simulation of such processes including springback. The first process considered is the so-called draw-bending test which involves load reversal. Next, cylindrical deep drawing followed by ring-splitting is investigated as a process involving more complex and in particular orthogonal loading-path changes. Lastly, the deep-drawing of a square box is simulated. In this latter case, directional hardening and residual stress development is particularly prominent in the corners of the box where the strain-path changes are most complex.

### 4.1 Introduction

As is well-known, severe non-proportional loading path changes, ubiquitous in complicated multiple-stage forming processes, can induce strongly anisotropic material behavior. Many studies (*e.g.*, Ghosh and Backofen, 1973; Hiwatashi et al., 1997, 1998; Hoc and Forest, 2001; Rauch and Schmitt, 1989; Rauch and Thuillier, 1993; Strauven and Aernoudt, 1987; Thuillier and Rauch, 1994; Wilson and Bate, 1994) have investigated the influence of strain-path changes on the microstructure and on the hardening behavior. In particular, most sheet metal forming processes involve non-proportional loading and changes in loading direction, resulting in a very complex material and structural behavior. Much of this complexity can be traced back to interaction between the material microstructure and the loading (*i.e.*, boundary) conditions. In particular, loading-path changes resulting in reorganization of persistent planar dislocation structures result in additional hardening effects beyond those accounted for by standard isotropic and kinematic models. A number of studies on these effects (*e.g.*, Bouvier et al., 2005, 2006, 2003; Nesterova et al., 2001a,b) have been carried out in order to understand the macroscopic material behavior of polycrystalline metals under strain-path changes at large deformations. Among the material models accounting for these additional effects, that of Teodosiu and Hu (1995, 1998) has been used by a number of authors (*e.g.*, Bouvier et al., 2005, 2003; Li et al., 2003; Montleau, 2004) to model the induced anisotropic hardening behavior and its effect on the springback processes. In the current work, the alternative model of (Wang et al., 2006a,d) is employed. In

---

\*Wang et al. (2006b)

this model, the effect of latent directional hardening on the total hardening behavior is modeled in the same way for continuous loading-path changes and for strain-path changes involving release. As such, this model is quite suitable for use in realistic sheet forming processes in which continuous strain path changes take place even in the range of inelastic deformation.

The paper begins (§2) with the review of the directional hardening model from Wang et al. (2006a,d). Next, the algorithmic formulation of the model for both implicit and explicit solution procedures is discussed (§3). Implementation of these into ABAQUS then facilitates their application to several forming processes including springback (§4). To investigate the effect of the hardening stagnation during load reversal, the draw-bending test is considered first. This is followed by the case of deep drawing of a cylindrical blank followed by ring-splitting involving more complex non-proportional and in particular orthogonal strain-path changes. Lastly, the deep-drawing of a square box is considered. The work ends with a summary and conclusions (§5).

## 4.2 Material model

Generally speaking, so-called “combined” hardening models based on isotropic and kinematic mechanisms are not capable of describing additional “cross” or “directional” hardening effects in metals arising from the orientation-dependence of the activation of dislocation motion and inelastic deformation. As such, they are generally inadequate for modeling the material behavior of metals in modern manufacturing processes involving complex, multistage, non-proportional loading paths. Because of this, a number of extensions of such “standard” models have been proposed in the literature (*e.g.*, Teodosiu and Hu, 1995, 1998; Yoshida and Uemori, 2003). Perhaps the most successful and well-known of these is that of Teodosiu and Hu (1998). This model has been applied by Li et al. (2003) and Bouvier et al. (2005) to the modeling and simulation of directional hardening effects in steels such as DP600 or DC06 subject to technologically-relevant processes such as deep drawing. In this model, evolving structure tensors are used to account for directional hardening effects resulting from the development of persistent dislocation structures during monotonic loading and from their re-organization upon changes in loading direction. The directional hardening behavior is also influenced by the effective polarity of excess dislocations of the same sign building up at these structures. In addition, the model accounts for “standard” kinematic and isotropic hardening effects. In the Teodosiu model, a fourth-order tensor-valued stress-like internal variable  $S$  is introduced to account for the effect of the directional strength of planar dislocation structures on the material hardening state. The variable  $S$  is described in such a way that the evolution equations are given for its projections parallel

$$s^d := \mathbf{A}_p \cdot S [\mathbf{A}_p] \quad (4.1)$$

and orthogonal

$$S^\ell := S - s^d \mathbf{A}_p \otimes \mathbf{A}_p \quad (4.2)$$

to the direction of the rate of plastic deformation. Here, the symbol “ $:=$ ” means “is defined equal to”,  $s^d$  represents the strength of the dislocation structures associated with the currently active slip systems, and  $S^\ell$  the strength of the dislocation structures associated with the latent slip systems. Several approaches were proposed in the literature how to integrate the evolution



equations for  $s^d$  and  $S^\ell$  in order to obtain  $S$ . They lead, however, to different physical results (Montleau, 2004). In the more recent model of Wang et al. (2006a,d), which is the one used here, this is not the case. Like the Teodosiu model, it is able to predict hardening stagnation during reversed loading as well as cross hardening and work softening which may occur during orthogonal strain-path changes. Differences arise in the way continuous changes in loading path affect the hardening behaviour as well as in the effect of simple shear on the development of latent directional hardening. Since the current work focuses mainly on the application of the model of (Wang et al., 2006a,d) to the simulation of forming processes and of springback, it as well as its numerical implementation are summarized only briefly in what follows. For more details, the reader is referred to the original sources.

The model formulation is based here on the inelastic multiplicative decomposition, plastic incompressibility, and small elastic strain, *i.e.*, expressed in incremental form. As usual, the evolution of all tensor-valued internal variables in this context is defined with respect to a local configuration rotating relative to the current configuration. For simplicity, this local configuration is defined as that in which the material symmetry directions for inelastic flow, as embodied in the fourth-order (symmetric traceless) flow anisotropy tensor  $A_{\text{Hill}}$ , are constant. In the current model, this is identified with the rotation  $R_E$  of the intermediate configuration with respect to the current configuration, with evolution equation

$$\dot{R}_E = WR_E - R_E W_P \quad (4.3)$$

determined by the continuum  $W = \text{skw}(L)$  and plastic  $W_P$  spins,  $L = \dot{F}F^{-1}$  being the velocity gradient as usual. On this basis, the elastic behavior of the model is based on the incremental hypoelastic relations

$$\begin{aligned} \overline{\dot{I} \cdot K} &= 3\kappa(I \cdot D), \\ \dot{M} &= 2\mu \{R_E^T \text{dev}(D)R_E - D_P\}, \end{aligned} \quad (4.4)$$

for the Kirchhoff stress  $K$  in the context of the orthogonal split

$$K = \frac{1}{3}(I \cdot K)I + \text{dev}(K) \quad (4.5)$$

of  $K$  into spherical and deviatoric parts, with

$$M = R_E^T \text{dev}(K)R_E. \quad (4.6)$$

These relations are determined in particular by the continuum deformation rate  $D = \text{sym}(L)$  and its inelastic counterpart  $D_P$ , with  $L = \dot{F}F^{-1}$  the velocity gradient, and  $F$  the deformation gradient. As usual for metals,  $D_P$  is assumed to satisfy incremental inelastic incompressibility  $I \cdot D_P = 0$ . As usual, we also have  $I \cdot D \approx 0$ . Here,  $\kappa$  represents the elastic bulk modulus, and  $\mu$  the shear modulus, both with respect to the reference configuration.

Turning next to the inelastic behavior, this is modeled in particular using the anisotropic form

$$\phi = \sigma_{\text{Hill}}(M - X) - \sigma_{y0} - r - f|S| \quad (4.7)$$

of the yield function analogous to the form introduced by Teodosiu and Hu (1998). Here,

$$\sigma_{\text{Hill}}(M - X) = \sqrt{(M - X) \cdot A_{\text{Hill}}[M - X]} \quad (4.8)$$

represents the Hill equivalent stress, and  $A_{\text{Hill}}$  the fourth-order symmetric traceless (orthotropic) Hill flow anisotropy tensor. Directional hardening effects are accounted for in  $\phi$  with the help of a stress-like fourth-order symmetric tensor  $S$  representing the effect of a persistent planar or sheet-like dislocation structures on the hardening behavior. Further,  $\mathbf{X}$  represents the back stress,  $\sigma_{Y0}$  represents the initial yield stress, and  $f$  represents a material constant determining the fraction of  $|S|$  contributing to isotropic hardening. In the current associated context,  $\phi$  determines in particular the inelastic deformation rate

$$\mathbf{D}_p = \lambda \partial_{M-\mathbf{X}} \phi = \lambda A_{\text{Hill}}[\mathbf{N}] \quad (4.9)$$

in terms of the measure

$$\mathbf{N} = \sigma_{\text{Hill}}^{-1}(\mathbf{M} - \mathbf{X}) \quad (4.10)$$

of the direction of the effective flow stress. In the current rate-independent context,  $\lambda$  represents the plastic multiplier enforcing rate-independence. Since  $A_{\text{Hill}}$  is deviatoric, note that  $\mathbf{I} \cdot A_{\text{Hill}}[\mathbf{M} - \mathbf{X}] = 0$  and  $\mathbf{D}_p = \text{dev}(\mathbf{D}_p)$  hold.

Consider next the evolution relations for hardening. For example, isotropic hardening is generally described in this work via the Voce model

$$r = (\sigma_{Y\infty} - \sigma_{Y0}) [1 - \exp(-c_r \alpha)] \quad (4.11)$$

Here,  $\sigma_{Y\infty}$  is the saturation value of the yield stress,  $\sigma_{Y0}$  is the initial yield stress,  $c_r$  controls the saturation rate, and  $\alpha$  represents the accumulated equivalent inelastic deformation, with evolution relation

$$\dot{\alpha} = \lambda \quad (4.12)$$

Alternatively, one could work with the Swift model, *i.e.*,

$$r = \sigma_{Yr}(\alpha_0 + \alpha)^n \quad (4.13)$$

where  $\sigma_{Yr}$  and  $\alpha_0$  are such material parameters that  $\sigma_{Y0} = \sigma_{Yr} \alpha_0^n$  holds.  $n$  is the hardening exponent. In contrast to the Voce model, note that the Swift model predicts no saturation of the yield stress. In some case, this is more appropriate to describe the monotonic hardening behavior of some steels.

Turning next to kinematic hardening, the evolution of the back stress  $\mathbf{X}$  is given here by the Armstrong-Frederick-like form

$$\dot{\mathbf{X}} = c_x(x_{\text{sat}} \mathbf{N} - \mathbf{X}) \lambda \quad (4.14)$$

involving growth and dynamic recovery. Note that in this context, the saturation magnitude  $x_{\text{sat}}$  of the back stress is not constant, *i.e.*, in contrast to the standard Armstrong-Frederick form. Indeed, it is determined by the constitutive form

$$x_{\text{sat}} = x_0 + (1 - f) \sqrt{|s^d|^2 + m |S^\ell|^2} \quad (4.15)$$

influenced in particular by directional hardening. Here,  $s^d$  represents the effect of dislocation structures associated with the currently active slip systems, and  $S^\ell$  that of dislocation structures

associated with latent systems, on the hardening behavior. In particular, it is this latter part that is responsible for cross or directional hardening effects. Further,  $x_0$  represents the (constant) value of  $x_{\text{sat}}$  for the case that  $f = 1$ , *i.e.*, when directional hardening does not affect kinematic hardening processes. Further,  $m$  represents the fraction of latent hardening processes influencing the development of  $x_{\text{sat}}$ .

In order to deal with the case of orthogonal strain-path changes both with and without unloading, we work with  $S$  itself as the independent internal variable here. This is in contrast to the model of Teodosiu and Hu (1998), who formulated evolution constitutive relations for  $s^d$  and  $S^\ell$ . In this sense, the current model is completed by the evolution constitutive relation

$$\dot{S} = c_d \{h_p s_{\text{sat}} - (h_p + h_x) s^d\} \mathbf{A}_p \otimes \mathbf{A}_p \lambda - c_\ell \{ |S^\ell| / s_{\text{sat}} \}^{n_\ell} S^\ell \lambda \quad (4.16)$$

for directional hardening as represented by  $S$ . Here,

$$\mathbf{A}_p := \text{sgn}(\mathbf{D}_p) = \mathbf{D}_p / |\mathbf{D}_p| \quad (4.17)$$

represents the direction of the inelastic deformation rate  $\mathbf{D}_p$ . Further,

$$s^d = s^d(S, \mathbf{A}_p) = \mathbf{A}_p \cdot S[\mathbf{A}_p] \quad (4.18)$$

represents the (scalar) dynamic part, and

$$S^\ell = S^\ell(S, \mathbf{A}_p) = S - (\mathbf{A}_p \cdot S[\mathbf{A}_p]) \mathbf{A}_p \otimes \mathbf{A}_p \quad (4.19)$$

the (tensorial) latent part, of  $S$  introduced above. Here,  $c_\ell$  and  $c_d$  represent material constants controlling the saturation rates of  $S^\ell$  and  $s^d$ , respectively. Further,  $s_{\text{sat}}$  is the saturation value of  $s^d$ . The exponent  $n_\ell$  determines the influence of prestraining on the evolution of  $S^\ell$ . In the meantime, excess dislocations building up at cell walls are of the same sign and hence polarized. The effect of this on the hardening behavior is represented mathematically in the model via a second-order symmetric traceless tensor-valued internal variable  $\mathbf{P}$ . Its evolution is given by

$$\dot{\mathbf{P}} = c_p (\mathbf{A}_p - \mathbf{P}) \lambda \quad (4.20)$$

as determined by the material constant  $c_p$  controlling the saturation rate of  $\mathbf{P}$  and  $\mathbf{A}_p$ . The material function  $h_p$  governs the contribution to current directional hardening arising from dislocation polarization processes. The magnitude of these contributions depends in particular on the projection  $\mathbf{A}_p \cdot \mathbf{P}$  of  $\mathbf{P}$  onto  $\mathbf{A}_p$ . Teodosiu and Hu (1995) worked with the form

$$h_p = \begin{cases} 1 - \frac{c_p}{c_d + c_p} \left| \frac{s^d}{s_{\text{sat}}} - \mathbf{A}_p \cdot \mathbf{P} \right| & \text{if } \mathbf{A}_p \cdot \mathbf{P} \geq 0 \\ (1 + \mathbf{A}_p \cdot \mathbf{P})^{n_p} \left\{ 1 - \frac{c_p}{c_d + c_p} \frac{s^d}{s_{\text{sat}}} \right\} & \text{if } \mathbf{A}_p \cdot \mathbf{P} < 0 \end{cases} \quad (4.21)$$

for  $h_p$ . The function  $h_x$  determines the influence of kinematic hardening processes on the development of  $s^d$  and is given as

$$h_x = \frac{1}{2} \left\{ 1 - \frac{1}{x_{\text{sat}}} \frac{\mathbf{A}_p \cdot \mathbf{X}}{\mathbf{A}_p \cdot \mathbf{N}} \right\} \quad (4.22)$$

Note that it attains non-negligible values only during a microplastic stage. In particular,  $h_x$  accounts for the slight decrease of  $s^d$  as the back stress approaches its saturation value.

Finally, following, *e.g.*, Dafalias (1998), the plastic spin  $\mathbf{W}_p$  is assumed to be driven by the non-coaxiality between the inelastic deformation rate and effective flow stress. In this case,

$$\mathbf{W}_p = \eta [\mathbf{D}_p, \mathbf{N}] = \eta (\mathbf{D}_p \mathbf{N} - \mathbf{N} \mathbf{D}_p) \quad (4.23)$$

holds, with  $\mathbf{N}$  the effective flow stress from (4.10), and  $\eta$  a material coefficient mediating the magnitude of this spin. In the isotropic case  $A_{\text{Hill}} = \frac{3}{2} \text{dev}$ , and the plastic spin vanishes. In contrast to the Jaumann case (or to the Green-Naghdi case), note that  $\mathbf{R}_E$  and (4.3) now depend on the stress state via  $\mathbf{W}_p$  and (4.23). As such,  $\mathbf{R}_E$  represents an independent internal variable in the formulation.

The above relations contain a total of 22 material parameters. These include the two elastic constants  $\kappa$  and  $\mu$ , the six Hill anisotropy parameters  $F$ ,  $G$ ,  $H$ ,  $L$ ,  $M$ , and  $N$  determining  $A_{\text{Hill}}$ , the saturation rate parameters  $c_p$ ,  $c_x$ ,  $c_d$ ,  $c_\ell$ , and  $c_r$ , as well as the remaining hardening parameters  $\sigma_{Y0}$ ,  $m$ ,  $x_0$ ,  $f$ ,  $\sigma_{Y\infty}$ ,  $s_{\text{sat}}$ ,  $n_\ell$ ,  $n_p$  and the plastic spin parameter  $\eta$ . This completes the material model summary. For more details, see Wang et al. (2006a,d). Next, we turn to algorithmic considerations.

### 4.3 Fully implicit and semi-implicit algorithmic formulations

In the context of the material model summarized in the last section, the goal of the present work is the investigation of the effects of some numerical issues on the simulation of metal forming processes and concomitant effects such as springback. To this end, the above material model has been implemented in the implicit finite-element program ABAQUS/Standard via the user-material interface UMAT. For completeness, we also discuss briefly the semi-explicit algorithmic formulation of the model for implementation in explicit codes such as ABAQUS/Explicit via the corresponding user interface VUMAT. Such a formulation facilitates application of the model to very large forming simulations where memory constraints make an implicit solution generally unviable. The simulations to be discussed in the following sections were all carried out using the implicit implementation.

#### 4.3.1 Implicit algorithm

Consider the implicit numerical integration and solution of the model over a finite time-interval  $[0, d] = \bigcup_{n=0}^{m-1} [t_n, t_{n+1}]$  consisting of  $m$  disjoint subintervals  $[t_0, t_1], \dots, [t_{m-1}, t_m]$ . Each such subinterval  $[t_n, t_{n+1}]$  is of duration  $t_{n+1,n} = t_{n+1} - t_n$ . As usual, the deformation gradient  $\mathbf{F}_n$ , as well as the values  $\mathbf{R}_{En}$ ,  $\mathbf{M}_n$ ,  $\mathbf{X}_n$ ,  $S_n$  and  $\mathbf{P}_n$ , are all known at the start  $t = t_n$  of this interval from the solution for the last one. On this basis, the current algorithm calculates the updates  $\mathbf{R}_{E_{n+1}}$ ,  $\mathbf{M}_{n+1}$ ,  $\mathbf{X}_{n+1}$ ,  $S_{n+1}$  and  $\mathbf{P}_{n+1}$  directly from the current algorithmic value  $\mathbf{F}_{n+1}$  of  $\mathbf{F}$ , representing in the current isothermal context the basic input at the Gauss-point level. In the context of commercial user interfaces such as ABAQUS UMAT, this means that we require as input variables (*i.e.*, in the incremental case) only  $\mathbf{F}_n$  and  $\mathbf{F}_{n+1}$ . All other quantities made available by such interfaces (*e.g.*, incremental rotations like DROT) are not needed.

Assuming that  $\mathbf{L} = \dot{\mathbf{F}}\mathbf{F}^{-1}$  is approximately constant in the interval  $[t_n, t_{n+1}]$ , exponential backward-Euler integration yields the approximation

$$\mathbf{L}_{n+1,n} := t_{n+1,n} \mathbf{L}_{n+1} = \ln(\mathbf{F}_{n+1,n}) = \mathbf{H}_{n+1,n} - \frac{1}{2} \mathbf{H}_{n+1,n}^2 + \frac{1}{3} \mathbf{H}_{n+1,n}^3 - \dots \quad (4.24)$$

for the incremental velocity gradient in terms of the corresponding relative displacement  $\mathbf{H}_{n+1,n} = \mathbf{F}_{n+1,n} - \mathbf{I}$  and deformation  $\mathbf{F}_{n+1,n} = \mathbf{F}_{n+1} \mathbf{F}_n^{-1}$  gradients. Assuming  $|\mathbf{H}_{n+1,n}| \ll 1$ , this will be approximated here for algorithmic simplicity by the midpoint form

$$\mathbf{L}_{n+1,n} = \mathbf{H}_{n+1,n} [\mathbf{I} + \frac{1}{2} \mathbf{H}_{n+1,n}]^{-1} = \mathbf{H}_{n+1,n} - \frac{1}{2} \mathbf{H}_{n+1,n}^2 + \frac{1}{4} \mathbf{H}_{n+1,n}^3 - \dots \quad (4.25)$$

In turn,  $\mathbf{L}_{n+1,n}$  determines the measures  $\mathbf{D}_{n+1,n} = \text{sym}(\mathbf{L}_{n+1,n})$  and  $\mathbf{W}_{n+1,n} = \text{skw}(\mathbf{L}_{n+1,n})$  of incremental strain and rotation, respectively. Consequently, both these quantities and the trace

$$\mathbf{I} \cdot \mathbf{K}_{n+1} = \mathbf{I} \cdot \mathbf{K}_n + 3\kappa (\mathbf{I} \cdot \mathbf{D}_{n+1,n}) \quad (4.26)$$

of the Kirchhoff stress obtained from backward-Euler integration of (4.4)<sub>1</sub> are determined directly by  $\mathbf{F}_{n+1,n}$ .

In the context of the backward-Euler approximation, numerical time-integration of the evolution relations (4.3), (4.4)<sub>2</sub>, (4.14), (4.16), (4.20) and (4.12) over an arbitrary time interval  $[t_n, t_{n+1}]$  yields the backward-Euler relations

$$\begin{aligned} \mathbf{r}_{\mathbf{R}_{E n+1,n}} &= \mathbf{R}_{E n+1,n} - \text{exv}(\boldsymbol{\omega}_{E n+1,n}), \\ \mathbf{r}_{\mathbf{M}_{n+1,n}} &= \mathbf{M}_{n+1,n} - 2\mu \{ \mathbf{R}_{E n+1}^T \text{dev}(\mathbf{D}_{n+1,n}) \mathbf{R}_{E n+1} - \mathbf{A}_{\text{Hill}}[\mathbf{N}_{n+1}] \lambda_{n+1,n} \}, \\ \mathbf{r}_{\mathbf{X}_{n+1,n}} &= \mathbf{X}_{n+1,n} - c_x \{ x_{\text{sat } n+1} \mathbf{N}_{n+1} - \mathbf{X}_{n+1} \} \lambda_{n+1,n}, \\ \mathbf{r}_{\mathbf{S}_{n+1,n}} &= \mathbf{S}_{n+1,n} \\ &\quad - c_d \{ h_{p n+1} s_{\text{sat}} - (h_{p n+1} + h_{x n+1}) s_{n+1}^d \} \mathbf{A}_{P n+1} \otimes \mathbf{A}_{P n+1} \lambda_{n+1,n} \\ &\quad - c_\ell \{ |\mathbf{S}_{n+1}^\ell| / s_{\text{sat}} \}^{n_\ell} \mathbf{S}_{n+1}^\ell \lambda_{n+1,n}, \\ \mathbf{r}_{\mathbf{P}_{n+1,n}} &= \mathbf{P}_{n+1,n} - c_p \{ \mathbf{A}_{P n+1} - \mathbf{P}_{n+1} \} \lambda_{n+1,n}, \\ r_{\alpha n+1,n} &= \alpha_{n+1,n} - \lambda_{n+1,n}, \\ r_{\lambda n+1,n} &= \phi_{n+1}, \end{aligned} \quad (4.27)$$

for the unknowns  $\mathbf{R}_{E n+1}$ ,  $\mathbf{M}_{n+1}$ ,  $\mathbf{X}_{n+1}$ ,  $\mathbf{S}_{n+1}$ ,  $\mathbf{P}_{n+1}$ ,  $\alpha_{n+1}$  and  $\lambda_{n+1,n} := t_{n+1,n} \lambda_{n+1}$ . Here,

$$\begin{aligned} \boldsymbol{\omega}_{E n+1,n} &:= \text{axv} \{ \mathbf{R}_{E n+1}^T \mathbf{W}_{n+1,n} \mathbf{R}_{E n+1} - \eta [\mathbf{A}_{\text{Hill}}[\mathbf{N}_{n+1}], \mathbf{N}_{n+1}] \lambda_{n+1,n} \} \\ &= \mathbf{R}_{E n+1}^T \mathbf{w}_{n+1,n} - \eta \text{axv} \{ [\mathbf{A}_{\text{Hill}}[\mathbf{N}_{n+1}], \mathbf{N}_{n+1}] \} \lambda_{n+1,n}, \end{aligned} \quad (4.28)$$

with  $\text{axv}(\mathbf{W})$  the axial vector of any skew-symmetric tensor  $\mathbf{W}$ , and  $\mathbf{w}_{n+1,n} := \text{axv}(\mathbf{W}_{n+1,n})$ . Further, the vector form

$$\text{exv}(\mathbf{w}) = \mathbf{I} + \sin |\mathbf{w}| \text{axt}(\text{sgn}(\mathbf{w})) + (\cos |\mathbf{w}| - 1) \text{axt}(\text{sgn}(\mathbf{w}))^2 \quad (4.29)$$

of the Rodrigues formula maps any non-zero vector  $\mathbf{w}$  into a rotation  $\text{exv}(\mathbf{w})$  with rotation axis  $\text{sgn}(\mathbf{w}) := \mathbf{w}/|\mathbf{w}|$ , and rotation angle  $|\mathbf{w}|$ . In addition,  $\text{axt}(\mathbf{w})$  is the skew-symmetric tensor

induced by any Euclidean vector  $\mathbf{w}$ , *i.e.*,  $\text{axt}(\mathbf{w})\mathbf{a} := \mathbf{w} \times \mathbf{a}$  for all  $\mathbf{a}$ . Introducing then the array

$$\boldsymbol{\epsilon}_{n+1} := \{\mathbf{R}_{\text{E}n+1}, \mathbf{M}_{n+1}, \mathbf{X}_{n+1}, \mathbf{S}_{n+1}, \mathbf{P}_{n+1}, \alpha_{n+1}, \lambda_{n+1,n}\} \quad (4.30)$$

of all internal variables, the backward-Euler relations above yield the implicit system

$$\mathbf{r}_{\boldsymbol{\epsilon}_n}(\boldsymbol{\epsilon}_{n+1}; \mathbf{F}_{n+1}) = \mathbf{0} \quad (4.31)$$

of relations to solve for  $\boldsymbol{\epsilon}_{n+1}$ . These are completed by the algebraic relations

$$\begin{aligned} r_{n+1} &= r(\alpha_{n+1}), \\ s_{n+1}^d &= \mathbf{A}_{\text{P}n+1} \cdot \mathbf{S}_{n+1}[\mathbf{A}_{\text{P}n+1}], \\ s_{n+1}^\ell &= \mathbf{S}_{n+1} - (\mathbf{A}_{\text{P}n+1} \cdot \mathbf{S}_{n+1}[\mathbf{A}_{\text{P}n+1}]) \mathbf{A}_{\text{P}n+1} \otimes \mathbf{A}_{\text{P}n+1}, \end{aligned} \quad (4.32)$$

from (4.11) or (4.13), (4.18), and (4.19), respectively. On this basis, this system can be solved in standard predictor-corrector fashion (*e.g.*, Simo and Hughes, 1998, Chapter 8). Note that in the elastic corrector step (*i.e.*,  $\phi_{n+1}^{\text{tr}} < 0$ ), the system (4.27) reduces to the form

$$\begin{aligned} \mathbf{R}_{\text{E}n+1} &= \text{exv}(\mathbf{w}_{n+1,n})\mathbf{R}_{\text{E}n}, \\ \mathbf{M}_{n+1} &= \mathbf{M}_n + 2\mu \mathbf{R}_{\text{E}n}^{\text{T}} \text{dev}(\mathbf{D}_{n+1,n})\mathbf{R}_{\text{E}n}, \\ \mathbf{X}_{n+1} &= \mathbf{X}_n, \\ \mathbf{S}_{n+1} &= \mathbf{S}_n, \\ \mathbf{P}_{n+1} &= \mathbf{P}_n, \\ \alpha_{n+1} &= \alpha_n. \end{aligned} \quad (4.33)$$

Lastly, we require the algorithmic derivative  $\partial_{\mathbf{F}_{n+1}}^a \mathbf{K}_{n+1}$  of the Kirchhoff stress  $\mathbf{K}_{n+1}$  with respect to  $\mathbf{F}_{n+1}$  for consistent linearization of the algorithmic weak form. This is based on the result

$$\mathbf{K}_{n+1} = \frac{1}{3} \kappa (\mathbf{I} \cdot \mathbf{D}_{n+1,n})\mathbf{I} + \mathbf{R}_{\text{E}n+1} \mathbf{M}_{n+1} \mathbf{R}_{\text{E}n+1}^{\text{T}} \quad (4.34)$$

for  $\mathbf{K}_{n+1}$  from (4.5), (4.6), and (4.26). On this basis, one obtains

$$\partial_{\mathbf{F}_{n+1}}^a \mathbf{K}_{n+1} = (\partial_{\mathbf{D}_{n+1,n}}^a \mathbf{K}_{n+1})(\partial_{\mathbf{F}_{n+1}} \mathbf{D}_{n+1,n}) + (\partial_{\mathbf{w}_{n+1,n}}^a \mathbf{K}_{n+1})(\partial_{\mathbf{F}_{n+1}} \mathbf{w}_{n+1,n}), \quad (4.35)$$

with

$$\partial_{\mathbf{D}_{n+1,n}}^a \mathbf{K}_{n+1} = \frac{1}{3} \kappa (\mathbf{I} \otimes \mathbf{I}) + (\mathbf{R}_{\text{E}n+1} \square \mathbf{R}_{\text{E}n+1}^{\text{T}})(\partial_{\mathbf{D}_{n+1,n}}^a \mathbf{M}_{n+1}) \quad (4.36)$$

and

$$\partial_{\mathbf{w}_{n+1,n}}^a \mathbf{K}_{n+1} = (\mathbf{K}_{n+1} \triangle \mathbf{I} + \mathbf{I} \square \mathbf{K}_{n+1})(\mathbf{I} \square \mathbf{R}_{\text{E}n+1}^{\text{T}})(\partial_{\mathbf{w}_{n+1,n}}^a \mathbf{R}_{\text{E}n+1}). \quad (4.37)$$

Here, the usual tensor products

$$\begin{aligned} (\mathbf{A} \square \mathbf{B})\mathbf{C} &:= \mathbf{ACB}, \\ (\mathbf{A} \triangle \mathbf{B})\mathbf{C} &:= \mathbf{AC}^{\text{T}}\mathbf{B}, \\ (\mathbf{A} \otimes \mathbf{B})\mathbf{C} &:= (\mathbf{B} \cdot \mathbf{C})\mathbf{A}, \end{aligned} \quad (4.38)$$

between second-order Euclidean tensors have been used. As usual, the backward-Euler system (4.31) yields the algorithmic derivatives

$$\begin{bmatrix} \partial_{\mathbf{D}_{n+1,n}}^a \mathbf{R}_{\mathbf{E}n+1} \\ \partial_{\mathbf{D}_{n+1,n}}^a \mathbf{M}_{n+1} \\ \vdots \\ \partial_{\mathbf{D}_{n+1,n}}^a \lambda_{n+1,n} \end{bmatrix} = -(\partial_{\boldsymbol{\epsilon}_{n+1}} \mathbf{r}_{\boldsymbol{\epsilon}n})^{-1} \begin{bmatrix} \mathbf{0} \\ \partial_{\mathbf{D}_{n+1,n}} \mathbf{r}_{\mathbf{M}n} \\ \vdots \\ \mathbf{0} \end{bmatrix} \quad (4.39)$$

and

$$\begin{bmatrix} \partial_{\mathbf{w}_{n+1,n}}^a \mathbf{R}_{\mathbf{E}n+1} \\ \partial_{\mathbf{w}_{n+1,n}}^a \mathbf{M}_{n+1} \\ \vdots \\ \partial_{\mathbf{w}_{n+1,n}}^a \lambda_{n+1,n} \end{bmatrix} = -(\partial_{\boldsymbol{\epsilon}_{n+1}} \mathbf{r}_{\boldsymbol{\epsilon}n})^{-1} \begin{bmatrix} \partial_{\mathbf{w}_{n+1,n}} \mathbf{r}_{\mathbf{R}_{\mathbf{E}n}} \\ \mathbf{0} \\ \vdots \\ \mathbf{0} \end{bmatrix} \quad (4.40)$$

of the internal variables with respect to  $\mathbf{F}_{n+1}$ ; in compact form

$$\begin{aligned} \partial_{\mathbf{D}_{n+1,n}}^a \boldsymbol{\epsilon}_{n+1} &= -(\partial_{\boldsymbol{\epsilon}_{n+1}} \mathbf{r}_{\boldsymbol{\epsilon}n})^{-1} (\partial_{\mathbf{D}_{n+1,n}} \mathbf{r}_{\boldsymbol{\epsilon}n}), \\ \partial_{\mathbf{w}_{n+1,n}}^a \boldsymbol{\epsilon}_{n+1} &= -(\partial_{\boldsymbol{\epsilon}_{n+1}} \mathbf{r}_{\boldsymbol{\epsilon}n})^{-1} (\partial_{\mathbf{w}_{n+1,n}} \mathbf{r}_{\boldsymbol{\epsilon}n}). \end{aligned} \quad (4.41)$$

Here,

$$\partial_{\boldsymbol{\epsilon}_{n+1}} \mathbf{r}_{\boldsymbol{\epsilon}n} := \begin{bmatrix} \partial_{\mathbf{R}_{\mathbf{E}n+1}} \mathbf{r}_{\mathbf{R}_{\mathbf{E}n}} & \partial_{\mathbf{M}_{n+1}} \mathbf{r}_{\mathbf{R}_{\mathbf{E}n}} & \cdots & \partial_{\lambda_{n+1,n}} \mathbf{r}_{\mathbf{R}_{\mathbf{E}n}} \\ \partial_{\mathbf{R}_{\mathbf{E}n+1}} \mathbf{r}_{\mathbf{M}n} & \partial_{\mathbf{M}_{n+1}} \mathbf{r}_{\mathbf{M}n} & \cdots & \partial_{\lambda_{n+1,n}} \mathbf{r}_{\mathbf{M}n} \\ \vdots & \vdots & \ddots & \vdots \\ \mathbf{0} & \partial_{\mathbf{M}_{n+1}} \mathbf{r}_{\lambda n} & \cdots & 0 \end{bmatrix} \quad (4.42)$$

represents the Jacobian of the system (4.31). In particular,

$$\begin{aligned} \partial_{\mathbf{w}_{n+1,n}} \mathbf{r}_{\mathbf{R}_{\mathbf{E}n}} &= -(\partial_{\boldsymbol{\omega}_{\mathbf{E}n+1,n}} \text{exv}) \mathbf{R}_{\mathbf{E}n+1}^{\mathbf{T}}, \\ \partial_{\mathbf{D}_{n+1,n}} \mathbf{r}_{\mathbf{M}n} &= 2\mu (\mathbf{R}_{\mathbf{E}n+1}^{\mathbf{T}} \square \mathbf{R}_{\mathbf{E}n+1}), \end{aligned} \quad (4.43)$$

follow from (4.31)<sub>1,2</sub>. Lastly,

$$\begin{aligned} \partial_{\mathbf{F}_{n+1}} \mathbf{D}_{n+1,n} &= \frac{1}{2} (\mathbf{I} \square \mathbf{I} + \mathbf{I} \triangle \mathbf{I}) (\partial_{\mathbf{H}_{n+1,n}} \mathbf{L}_{n+1,n}) (\mathbf{I} \square \mathbf{F}_n^{-1}), \\ \partial_{\mathbf{F}_{n+1}} \mathbf{w}_{n+1,n} &= \frac{1}{2} \text{axv} (\mathbf{I} \square \mathbf{I} - \mathbf{I} \triangle \mathbf{I}) (\partial_{\mathbf{H}_{n+1,n}} \mathbf{L}_{n+1,n}) (\mathbf{I} \square \mathbf{F}_n^{-1}), \end{aligned} \quad (4.44)$$

are obtained from the midpoint approximation (4.25) to the exact algorithmic expression (4.24).

For the implementation of the above algorithm in ABAQUS UMAT, we require only the “material part” of  $\partial_{\mathbf{F}_{n+1}}^a \mathbf{K}_{n+1}$ . In the current context, we have

$$\text{DDSDDE} \equiv \det(\mathbf{F}_{n+1}^{-1}) (\partial_{\mathbf{D}_{n+1,n}}^a \mathbf{K}_{n+1}) \quad , \quad (4.45)$$

where DDSDDE represents the ABAQUS UMAT variable for the material part of the consistent tangent. This together with the current algorithmic state of stress  $\mathbf{K}_{n+1}$  (in the form of the corresponding Cauchy stress) are returned to ABAQUS/Standard for the global solution via global Newton-Raphson iteration. Again, we emphasize that the implementation of the current algorithm in ABAQUS UMAT require only the variables DFGRD0  $\equiv \mathbf{F}_n$  and DFGRD1  $\equiv \mathbf{F}_{n+1}^{(i)}$  as input. All other quantities made available by such interfaces are not needed.

### 4.3.2 Semi-implicit form

As is well-known, for large-scale structural simulations, implicit solution methods may become less efficient than mixed or fully-explicit methods. Use of the latter methods entails stability requirements which result in a global limitation on the time-step size. As such, the efficiency gained by employing implicit rather than explicit time-integration to solve for the material response at the integration-point level is then lost. In the current rate-independent case, however, algorithmic fulfillment of the yield condition  $\phi_{n+1} = 0$  using a purely explicit scheme is tricky. Indeed, the fulfillment of this condition is most straightforward via a plastic corrector step in the context of an implicit solution. These observations have been incorporated into the idea of so-called cutting plane algorithm (*e.g.*, Simo and Hughes, 1998, Chapter 3), representing one kind of semi-implicit scheme (*e.g.*, Belytschko et al., 2000, Chapter 5). For the current model, the corresponding algorithm takes the following form:

1. initialization:

$$\begin{aligned}
 i &= 0; \\
 \mathbf{R}_{E n+1}^{(i)} &= \text{exv}(\mathbf{w}_{n+1,n}) \mathbf{R}_{E n}; \\
 \mathbf{M}_{n+1}^{(i)} &= \mathbf{M}_n + 2\mu \mathbf{R}_{E n}^T \text{dev}(\mathbf{D}_{n+1,n}) \mathbf{R}_{E n}; \\
 \mathbf{X}_{n+1}^{(i)} &= \mathbf{X}_n; \\
 \mathbf{S}_{n+1}^{(i)} &= \mathbf{S}_n; \\
 \mathbf{P}_{n+1}^{(i)} &= \mathbf{P}_n; \\
 \alpha_{n+1}^{(i)} &= \alpha_n;
 \end{aligned}$$

2. if  $\phi_{n+1}^{(i)} \leq 0$ , go to 4; 3. else while  $\phi_{n+1}^{(i)} > 0$ ,

$$\begin{aligned}
 \lambda_{n+1,n}^{(i+1)} &= \lambda_{n+1,n}^{(i)} - \{ \phi_{n+1} / \partial \lambda_{n+1,n} \phi_{n+1} \}^{(i)}; \\
 \mathbf{R}_{E n+1}^{(i+1)} &= \mathbf{R}_{E n+1}^{(i)} \text{exv} \{ \mathbf{R}_{E n+1}^{(i)T} \mathbf{w}_{n+1,n} - \eta \text{axv} \{ [A_{\text{Hill}}[\mathbf{N}_{n+1}^{(i)}], \mathbf{N}_{n+1}^{(i)}] \} \lambda_{n+1,n}^{(i+1)} \}; \\
 \mathbf{M}_{n+1}^{(i+1)} &= \mathbf{M}_{n+1}^{(i)} + 2\mu \{ \mathbf{R}_{E n+1}^{(i)T} \text{dev}(\mathbf{D}_{n+1,n}) \mathbf{R}_{E n+1}^{(i)} - A_{\text{Hill}}[\mathbf{N}_{n+1}^{(i)}] \lambda_{n+1,n}^{(i+1)} \}; \\
 \mathbf{X}_{n+1}^{(i+1)} &= \mathbf{X}_{n+1}^{(i)} + c_x \{ x_{\text{sat } n+1}^{(i)} \mathbf{N}_{n+1}^{(i)} - \mathbf{X}_{n+1}^{(i)} \} \lambda_{n+1,n}^{(i+1)}; \\
 \mathbf{S}_{n+1}^{(i+1)} &= \mathbf{S}_{n+1}^{(i)} \\
 &+ c_d \{ h_{p n+1}^{(i)} s_{\text{sat}} - (h_{p n+1}^{(i)} + h_{x n+1}^{(i)}) s_{n+1}^{d(i)} \} \mathbf{A}_{P n+1}^{(i)} \otimes \mathbf{A}_{P n+1}^{(i)} \lambda_{n+1,n}^{(i+1)} \\
 &- c_\ell \{ |S_{n+1}^{\ell(i)}| / s_{\text{sat}} \}^{n_\ell} S_{n+1}^{\ell(i)} \lambda_{n+1,n}^{(i+1)}; \\
 \mathbf{P}_{n+1}^{(i+1)} &= \mathbf{P}_{n+1}^{(i)} + c_p \{ \mathbf{A}_{P n+1}^{(i)} - \mathbf{P}_{n+1}^{(i)} \} \lambda_{n+1,n}^{(i+1)}; \\
 \alpha_{n+1}^{(i+1)} &= \alpha_{n+1}^{(i)} + \lambda_{n+1,n}^{(i+1)}; \\
 i &++;
 \end{aligned} \tag{4.46}$$

4. update internal variables:

$$\epsilon_{n+1} = \epsilon_{n+1}^{(i)}. \tag{4.47}$$

Note that

$$\begin{aligned}
 \partial_{\lambda_{n+1,n}} \phi_{n+1} &= (\partial_{\mathbf{M}_{n+1}} \phi_{n+1}) \cdot (\partial_{\lambda_{n+1,n}} \mathbf{M}_{n+1}) + (\partial_{\mathbf{X}_{n+1}} \phi_{n+1}) \cdot (\partial_{\lambda_{n+1,n}} \mathbf{X}_{n+1}) \\
 &+ (\partial_{\mathbf{S}_{n+1}} \phi_{n+1}) \cdot (\partial_{\lambda_{n+1,n}} \mathbf{S}_{n+1}),
 \end{aligned} \tag{4.48}$$



follows from the functional form (4.7) of the yield condition. In terms of simplicity, the advantage of this algorithm is of course the fact that the iteration is explicit. As such, there is no need to solve an entire equation system for each iteration in the sense of Newton-Raphson iteration.

Detailed comparisons between the implicit and explicit solution approaches on large structures represent work in progress and will be reported on in the future. In the current work, attention is restricted for simplicity to simulations carried out using the implicit algorithm discussed above implemented into ABAQUS/Standard via the user material interface UMAT.

## 4.4 Application to springback prediction

### 4.4.1 Draw-bending test

A number of authors (*e.g.*, Carden et al., 2002; Kleiner et al., 2005; Wagoner et al., 2002) have investigated the draw-bending test as a well-characterized forming operation that produces springback similarly to industrial stamping forming operations. In this test, sheet metal is drawn, stretched, bent, and then straightened over a die radius comparable to that of a typical die cavity. As such, it is exemplary for a number of sheet forming operations, but has the advantage of simplicity. More importantly, sheet loading may be controlled directly and accurately. In real press forming operations, sheet loading depends on the complex interaction between the material behavior, contact and friction, draw-bead configurations, as well as blank holder forces and displacements. This makes it very difficult to compare simulation and experimental results. The draw-bending test offers the necessary simplification for such a comparison in the sense that it simplifies the boundary conditions and eliminates friction effects, allowing for a focus on the effect of the loading conditions on the material behavior, residual stress development and springback.

The test itself is carried out with the help of a standard servo-hydraulic mechanical test machine and bending frame as shown in Figure 4.1 (left). Here, two hydraulic actuators oriented at  $90^\circ$  to each other control the forming of the strip. In particular, the right actuator provides a constant restraining force (*i.e.*, the tension force), while the left one moves at a constant speed. The tension force is measured by sensors attached to each actuator. At the beginning of the test, the specimen is first pre-bent in a right angle with a triangular punch rounded off at the corner. Then it was clamped into the machine. A tension force of 81.5 KN was applied at the left end of the strip holding the right end fixed. This results in the strip being drawn over the fixed roller with negligible friction at constant tension. The drawing speed was 40 mm/s. In this case, the sheet metal strip undergoes bending and unbending under constant tension, resulting in a load reversal in the material in the sense of bending and unbending. Finally, the specimen is released, resulting in springback and the final form of the strip (Figure 4.1, right).

For simplicity, any effects of the mild initial flow anisotropy and the plastic spin are neglected here. As just discussed, in the experiment, the strips are pre-bent from straight into a right angle by means of a triangular punch rounded off at the corner. This pre-bending process is idealized in the simulation by pre-bending the strip directly around the guide roller with the bending tool, resulting in the initial configuration as shown in Figure 4.2. In the current simulation, the

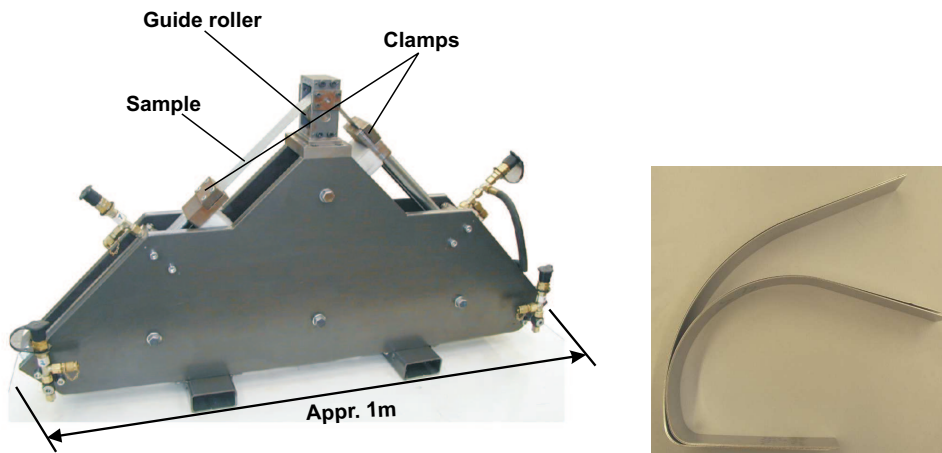


Figure 4.1: Left: Bending-tension test machine from Kleiner et al. (2005). In this test, the sheet metal strip is first pre-bent, clamped into the machine and stretched around the roller to the corresponding form. The test itself is then performed by pulling the strip from left to right via the clamps around the roller. Right: Specimens of the sheet metal DP600 with thicknesses of 1mm and 2mm after being subject to the draw-bending (Kleiner et al., 2005).

roller and bending tool are idealized as analytical rigid surfaces. As in the tests, the strip is 448 mm long, 50 mm wide and with a thickness 1 mm. In addition, the roller, and so the bending radius is 10 mm. Due to the symmetry of the specimen, only half of the structure need to be included in the simulation. The 4-node doubly curved general-purpose shell element S4R with 11 integration points along the thickness is used here. As investigated elsewhere (Wang et al., 2006d), a convergent solution is obtained for this case with 10 such elements across the strip (Figure 4.2). The material used in the test is the high-strength steel DP600.

During the draw-bending process, the strip undergoes bending and unbending. This results in compression followed by extension of the material on the underside of the strip in contact with the roller. On the other hand, the material on the top of the strip experience first extension followed by compression. Consequently, the strain-path change here takes the form of strain reversal. As shown by experimental investigations (Figure 4.3), besides a very pronounced Bauschinger effect, DP600 also exhibits hardening stagnation after strain reversal. To demonstrate the importance of taking hardening stagnation into account, we compare the experimental results for springback after draw-bending with corresponding simulation results based on “standard” combined and current hardening models. Here and in what follows, “combined hardening” refers to the combination of Voce isotropic and Armstrong-Frederick kinematic hardening. The material parameter values for DP600 for these models obtained from the data in Banu et al. (2001) are given in Table 4.1 (left) for the directional hardening model and for the combined hardening model (right). The data used by Banu et al. (2001) takes the form of uniaxial tensile and simple shear tests with load reversal. Since standard combined hardening modeling does not take hardening stagnation into account, the yield stress upon the load reversal predicted by this model is higher than in the case of the current model (Figure 4.4, left). Turning now to the

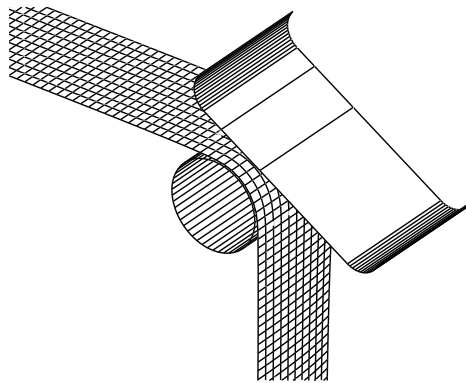


Figure 4.2: 3D FEM model for the draw-bending test.

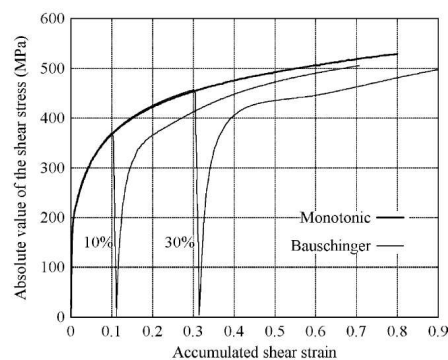


Figure 4.3: Experimental stress-strain results for the steel DP600 subject to simple shear followed by load reversal (Bouvier et al., 2006).

simulation of draw-bending, Figure 4.4 (right) shows the predicted von Mises residual stress distribution along the strip after springback using the current model. This clearly shows the inhomogeneous residual stress distribution in the strip. The highest residual stresses occur at the edges. Relatively high stresses are also observed in the center of the strip.

A comparison of experimental and predicted sheet metal shapes after draw-bending is given in Figure 4.5. These results show that, in the drawn area ( $0 \leq x \leq 140$  mm), the sheet shape predicted by the current model is closer to experiment than the combined model. Indeed, the latter model overestimates the amount of springback. As already mentioned above, the reason for this is to be found in the higher yield stress predicted by the combined hardening model upon the load reversal (Figure 4.4, left). This results in higher residual stresses in the unbent part of the strip, and so more stored energy. As for the non-drawn parts of the strip ( $140 \text{ mm} \leq x$ ), the differences here between the experimental results and current model prediction are a result of the differences in the experimental and modeling procedures for the pre-bending stage discussed above and are of no consequence for the springback comparison.

#### 4.4.2 Ring-splitting test

As another application of the current model, consider the case of cylindrical cup drawing followed by ring-splitting as shown in Figure 4.6. In this process, a cylindrical cup is deep-drawn and

parameter	value	units
$\kappa$	158333	MPa
$\mu$	73077	MPa
$\sigma_{Y0}$	308.3	MPa
$x_0$	153.0	MPa
$\sigma_{Y\infty}$	433.5	MPa
$s_{sat}$	387.2	MPa

parameter	value
$c_p$	0.13
$c_x$	53.5
$c_d$	4.0
$c_\ell$	0.0
$c_r$	49.7
$m$	0.0
$f$	0.862
$n_\ell$	0.0
$n_p$	649

parameter	value	units
$\kappa$	158333	MPa
$\mu$	73077	MPa
$\sigma_{Y0}$	308.3	MPa
$x_{sat}$	225.3	MPa
$\sigma_{Y\infty}$	673.9	MPa
$c_x$	73.7	
$c_r$	6.75	

Table 4.1: Current hardening model parameter values (left two tables) and combined hardening (*i.e.*, Voce isotropic, Armstrong-Frederick kinematic) model parameter values (right table) for DP600 based on data from Banu et al. (2001).

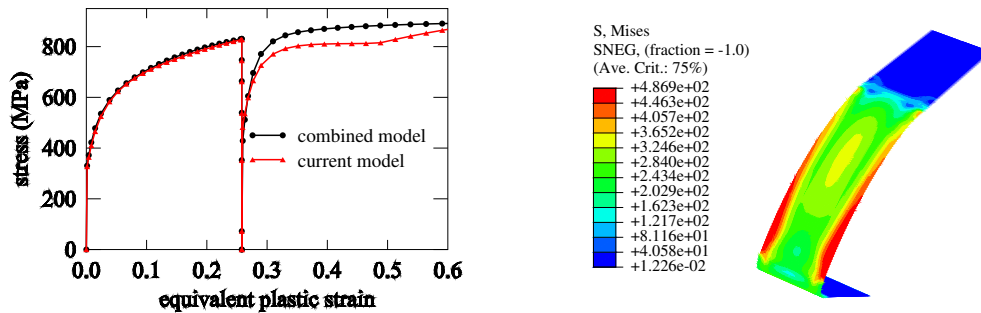


Figure 4.4: Left: Stress development in DP600 during tension pre-loading followed by compression predicted by the combined and current hardening models. Right: Predicted von Mises residual stress distribution along the strip after springback using the current model.

then cut into several closed rings. These are then split open perpendicular to the circumference of the ring. This results in the release of energy stored in the material during deep-drawing and residual stress development, leading to springback. As shown by the experimental results, this process is highly heterogeneous. More specifically, we have the following steps: (i) deep drawing of a cylindrical cup from a circular blank with a constant blank holder force, (ii) cutting of 4 rings every 10mm from the open edge of the drawn cup, and the width of rings is 10mm too, (iii) splitting of the rings, (iv) measurement of the resulting ring-opening or closing, representing the form taken by springback here. Next, consider the experimental setup. This is shown in Figure 4.7. The circular blanks considered here have an initial radius of 140 mm and an initial thickness of 0.6 mm. The punch has a radius of 73.35 mm and is rounded off at the corner with a radius of 8 mm. The die has an internal radius of 76 mm and is rounded off at the corner with a radius of 6.5 mm. The blank holder has an internal radius of 76 mm.

Again neglecting the (relatively mild) initial flow anisotropy for simplicity, as well as any plastic-spin effects, the deep-drawing stage of the test is simulated using an axisymmetric FE-model to reduce the computational cost. In this model, the blank is discretized using 208 2-node linear axisymmetric shell elements of type SAX1 in ABAQUS. After deep-drawing, the simulation results are transformed to a three-dimensional FE-model for the ring-splitting stage

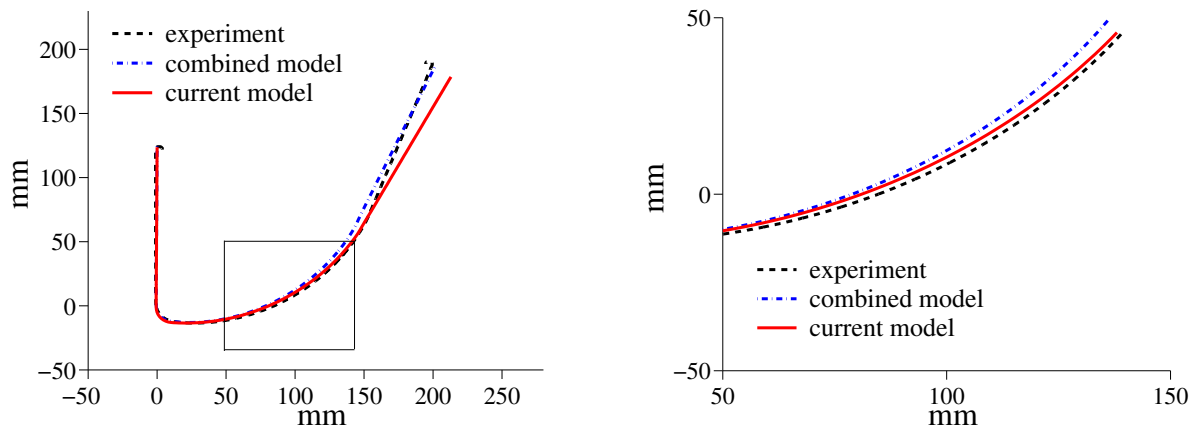


Figure 4.5: Comparison of experimental and predicted springback after draw-bending. Left: entire strip and drawn part of the strip (in black box). Right: enlarged view of drawn area of the strip inside black box on the left.

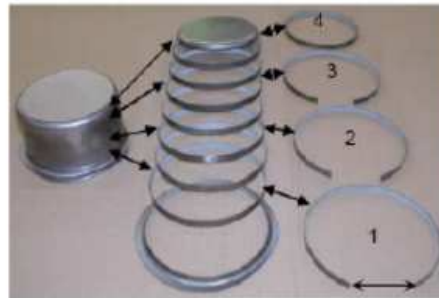


Figure 4.6: Ring-splitting test for the steel DC04 (Rohleder et al., 2001). See text for details.

of the simulation. This is done for one-half of the structure using elements of the type S3 and S4 as shown in Figure 4.8 (left). Corresponding to the experimental procedure, the cup is “cut” into several rings of height 10 mm perpendicular to the cup axis. The rings are numbered 1, 2, 3 and 4 in the sequence shown in Figure 4.8 (right). For simplicity, the rigid punch, the die and the blank holder are modeled as analytical rigid surfaces. In addition, the mechanical interaction between the contact surfaces is set to be a frictional contact with a Coulomb friction coefficient of 0.07. During the deep-drawing stage, a force of 130 kN is applied to the blank holder.

Deep-drawing involves not only “simple” strain paths like monotonic or reversed loading but also more complex orthogonal and mixed ones. As such, directional hardening effects should become important. In addition, the local deformation history and state in the cup and rings is quite heterogeneous. In order to gain insight into the connection between hardening type and resulting springback, results for combined hardening as well as for the current directional hardening model are compared in what follows. The blank material here is assumed to be DC06. This material exhibits a mild Bauschinger effect as well as pronounced hardening stagnation and cross hardening (Figure 4.9). The corresponding material parameters values used for combined hardening are given in Table 4.2 (left), and those for the current model in Table 4.2 (right). The material parameters of the combined hardening model were determined in Banu et al. (2001)

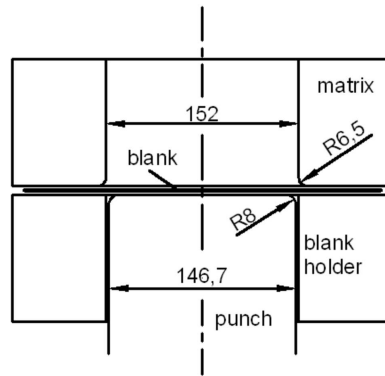


Figure 4.7: Geometry of the deep drawing setup. See text for details.

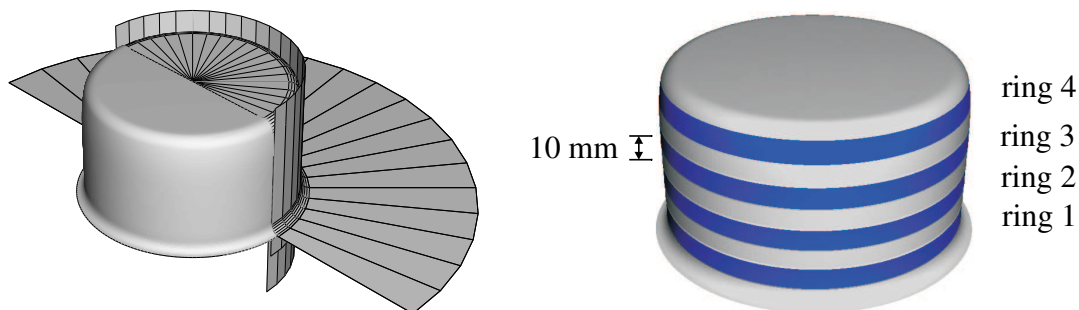


Figure 4.8: FE model of deep drawing test (left) and the location of rings (right).

using monotonic (*i.e.*, uniaxial tension and simple shear) tests as well as non-monotonic simple shear tests with load reversal. Those for directional hardening were determined with the help of orthogonal tests consisting of tension pre-loading, release and simple shear re-loading. Note that both models identified in this way exhibit approximately the same monotonic hardening behavior (Figure 4.10, left). The differences between these models become evident when tests with strain-path changes are considered. For example, after load reversal, both the current and combined hardening models predict the Bauschinger effect. In the current model, however, the yield stress after the load reversal is lower than in the Armstrong-Frederick case due to the hardening stagnation (Figure 4.10, upper right). And since it takes cross hardening into account, the current model predicts a higher yield stress than the combined model after an orthogonal strain-path change (Figure 4.10, lower middle). The yield stress predicted by combined hardening is significantly lower than the others because the back stress of the Armstrong-Frederick type predicts a reduction of the yield stress during orthogonal strain-path changes. Consequently, for load reversal, the combined hardening model predicts harder behavior than the current model including in addition hardening stagnation and cross hardening. On the other hand, for an orthogonal change, the latter process results in the current model predicting harder behavior. So, depending on the loading history, one or the other model will predict higher residual stresses for a given forming operation.

To compare the influence of the hardening behavior on the residual stresses and springback

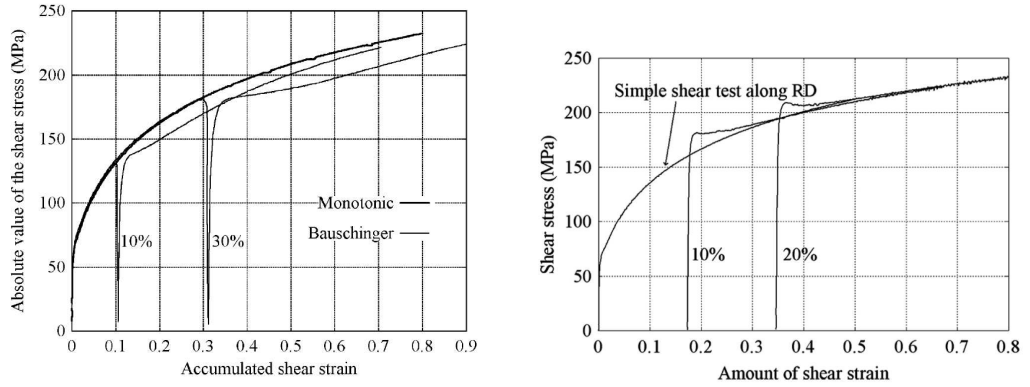


Figure 4.9: Experimental results for the mild steel DC06 subjected to simple shear followed by load reversal (left) and to uniaxial tension followed by simple shear (right) (Bouvier et al., 2006). The latter represents an orthogonal strain-path change.

parameter	value	units
$\kappa$	158333	MPa
$\mu$	73077	MPa
$\sigma_{Y0}$	121.1	MPa
$x_{\text{sat}}$	49.0	MPa
$\sigma_{Y\infty}$	357.6	MPa
$c_x$	153.3	
$c_r$	7.3	

parameter	value	units
$\kappa$	158333	MPa
$\mu$	73077	MPa
$\sigma_{Y0}$	121.1	MPa
$x_0$	15.9	MPa
$\sigma_{Y\infty}$	211.1	MPa
$s_{\text{sat}}$	231.1	MPa

parameter	value
$c_p$	5.5
$c_x$	446.0
$c_d$	4.0
$c_\ell$	1.86
$c_r$	31.9
$m$	1.5
$f$	0.445
$n_\ell$	0.0
$n_p$	27.9

Table 4.2: Combined (left table) and directional (right two tables) hardening model parameter values for DC06 determined from the data of Banu et al. (2001).

in the case of a cylindric cup deep-drawing, consider next the simulation results for ring opening as shown in Figure 4.11. Ring opening after deep-drawing is considered a measure of the amount of energy stored in the (closed) structure during the drawing stage due to inhomogeneous deformation and residual stress development, in particular in the circumferential direction. Note that the current model predicts more ring opening in all four rings than the combined hardening model. To understand the reason for this, consider the evolution of the direction of the rate of plastic deformation. This can be represented locally in terms of the scalar product  $\theta(t) := \mathbf{A}_p(t) \cdot \mathbf{A}_p(0)$  of the initial  $\mathbf{A}_p(0)$  and current  $\mathbf{A}_p(t)$  values of the direction  $\mathbf{A}_p$  of the plastic rate of deformation  $\mathbf{D}_p$ . Figure 4.12 shows the development of  $\mathbf{A}_p$ ,  $\theta$  and the accumulated equivalent plastic strain  $\alpha$  for a material point on the outside (above) and the inside (below) of the cup as parameterized by the displacement of the punch. Up to a punch displacement of approximately 28 mm, *i.e.*, in the flange region, both points experience the same monotonic loading path, representing a combination of radial stretching ( $A_{p11}$ ) and tangential compression ( $A_{p22}$ ). As the material enters the bending stage (*i.e.*, punch displacement between 28 and 32 mm), however, the radial stretching on the outside of the cup reverses into compression (Figure 4.12, left), while that on the inside intensifies (Figure 4.12, right). At the end of the bending stage, the parameter  $\theta$  is close to zero on the outside (Figure 4.12, left), im-

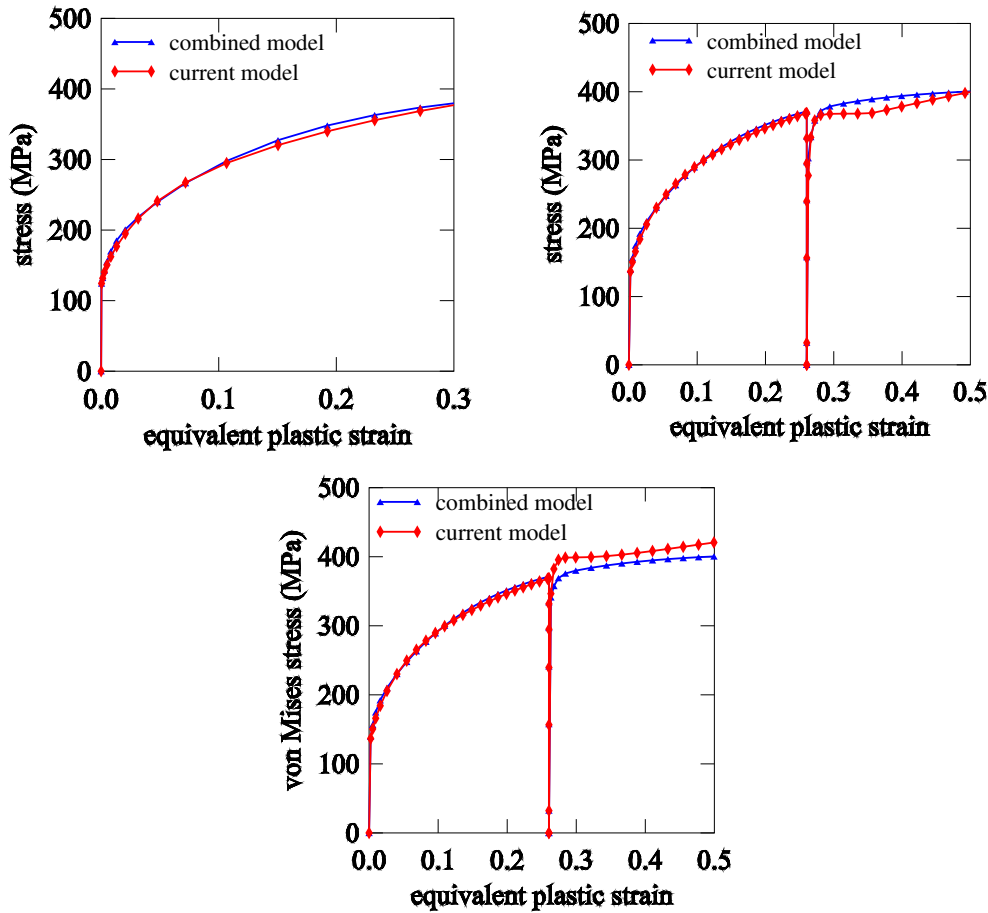


Figure 4.10: Predicted stress development in DC06 for standard combined and current hardening models for different loading paths. Above left: monotonic uniaxial tension. Above right: tension-compression reverse strain-path change. Below middle: tension-shear orthogonal strain-path change.

plying an orthogonal strain-path change. On the other hand, on the inside (Figure 4.12, right),  $\theta$  has a value of approximately 0.65, representing a “mixture” of orthogonal and monotonic loading. Note also that all of these are *continuous* strain-path changes (*i.e.*, not changes involving unloading), something indicated by the continual increase in  $\alpha$  as well. Recall now that, for monotonic loading (Figure 4.10, above left), the predicted hardening behavior from the combined and current models is about the same. On the other hand, for an orthogonal loading-path change (4.10, below middle), the current model predicts harder behavior. Consequently, during the bending stage, the current model leads to a higher hardening level, implying higher residual stresses, and larger ring opening.

It is also interesting to investigate the evolution of the hardening variables at these points in the structure during deep drawing. Figure 4.13 displays the evolution of the corresponding variables at the two points in question. Note that, in the bending stage,  $s^d$  and  $|S^\ell|$  develop in manner typical for an orthogonal strain-path change. In particular, on the outside of the cup (4.13, left),  $s^d$  drops almost to zero, and  $|S^\ell|$  increases almost to the value of  $s^d$  before the strain-path change (Wang et al., 2006c). This results in an accelerated growth of  $\mathbf{X}$  in the



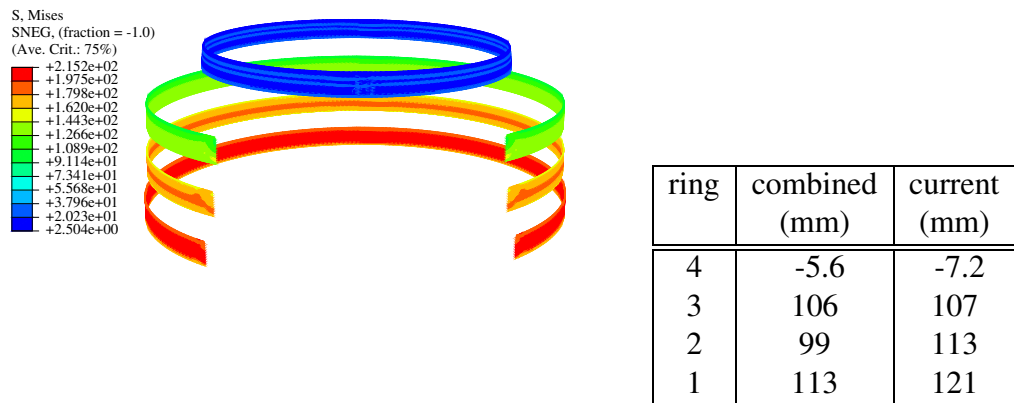


Figure 4.11: Left: von Mises stress distribution in the opened rings after splitting. Right: Results for ring opening simulated with the combined and current models.

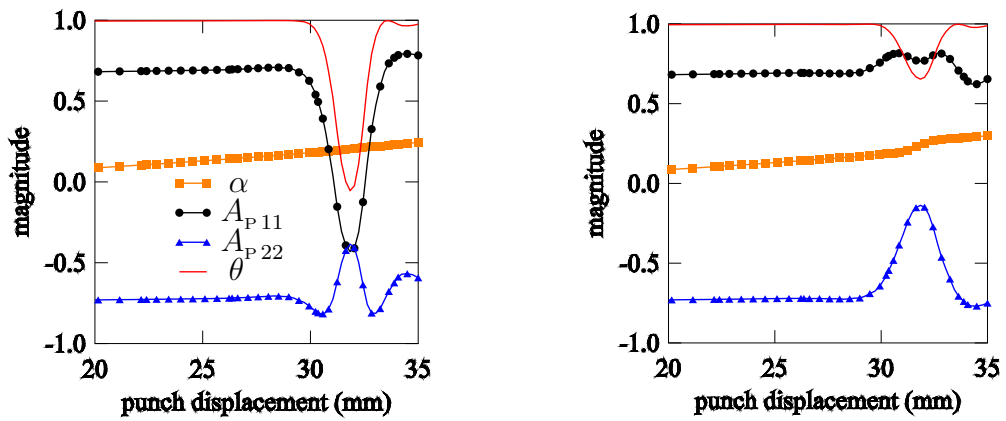


Figure 4.12: Evolution of  $\alpha$ ,  $A_p$  and  $\theta$  at a material point on the outside (left) and on the inside (right) in the middle of Ring 3 during deep drawing.

sense of (4.15). The point on the inside of the cup (4.13, right) shows a similar behavior of the corresponding variables during the bending stage, the only difference that the changes are not so drastic due to the fact that the strain-path change is milder than orthogonal. It is worth pointing out that all of these results and trends are highly dependent on the parameter values used. For more details on this, the reader is referred to Wang et al. (2006d).

Due to the absence of the experiment result for the above simulation, more recently, another simulation has been carried out to compare with the experiment. In this test, the same forming tools are used, but only two rings are taken out of the cup with ring height 4 mm. The rings are numbered 1 and 2 in the sequence shown in Figure 4.14 (right). The positions of the upper edges of the ring 1 and ring 2 have a vertical distance of 67 mm and 41.5 mm to the cup bottom, respectively. Different from the precious case, the punch displacement is 75 mm. Holder force has the same value as the previous one.

To compare the influence of the hardening behavior on the residual stresses and springback in the case of a cylindric cup deep-drawing, consider next the simulation results for ring opening as shown in Figure 4.15. Similarly, note that the current model predicts more ring opening in both

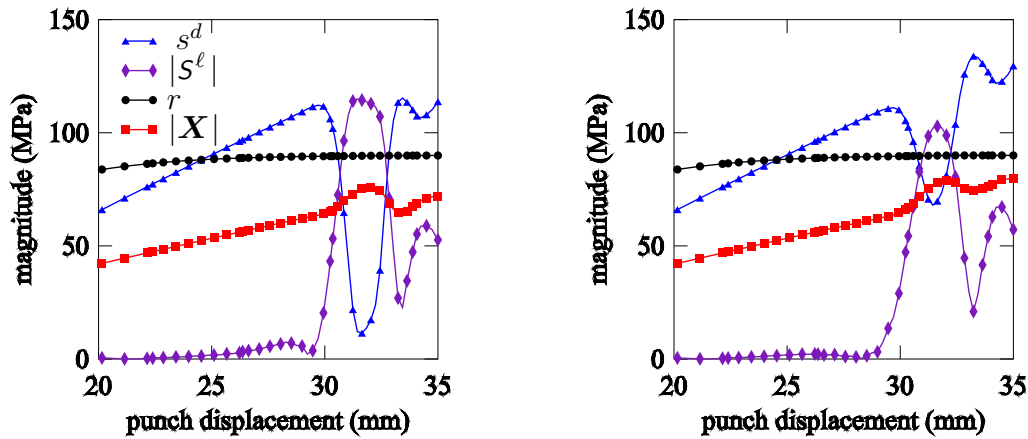


Figure 4.13: Evolution of the current model hardening variables at a material point on the outside (left) and on the inside (right) in the middle of Ring 3 during deep drawing.



Figure 4.14: Location of rings in the experiment.

rings than the combined hardening model. Figure 4.16 shows the development of  $A_p$ ,  $\theta$  and the accumulated equivalent plastic strain  $\alpha$  for a material point on the outside (left) and the inside (right) of the cup as parameterized by the displacement of the punch. Figure 4.17 displays the evolution of the corresponding variables at the two points in question in this case. We can see the evolution of  $\theta$  and hardening variables are also very similar to the previous simulation. Concerning the comparison to the experimental results, both models underestimate the ring opening. Nevertheless, the difference of 7.6 mm between the experiment and current model is rather moderate given the complexity of the process. The reason for the larger deviation in the case of ring 1 (15.2 mm) is probably a high amount of accumulated plastic strain in this ring. The equivalent plastic strain for material points, lying on the inward and outward surfaces of the ring, reaches up to 60 percents. The experimental curves, however, to that the material parameters were fitted in Banu et al. (2001), go maximal up to 45 percent of equivalent plastic strain (simple shear curves). Accordingly, it cannot be excluded that the model underestimate the real hardening level at plastic strains larger than 50 percent and, thus, predicts lower amount of elastic energy, stored during the deep drawing process. Additionally, such numerical aspects as the simplified modeling of the friction between the blank and the tools as well as of the cutting procedure may, of course, contribute to the inaccuracy of the numerical prediction.

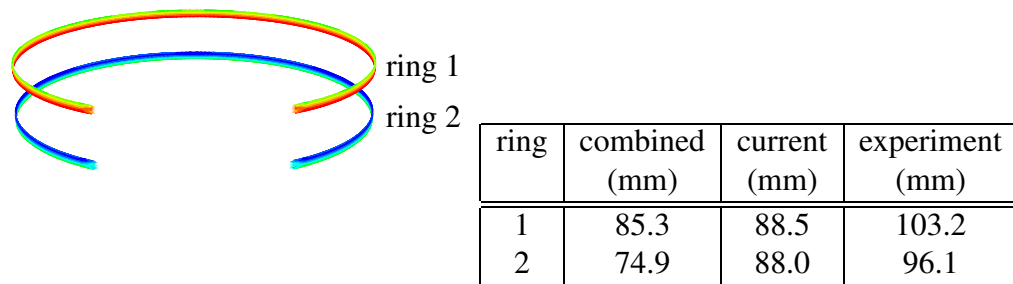


Figure 4.15: Left: von Mises stress distribution in the opened rings after splitting, ring 1: about 231 MPa, ring 2: about 160 MPa. Right: Results for experimental and numerical ring opening simulated with the combined and current models.

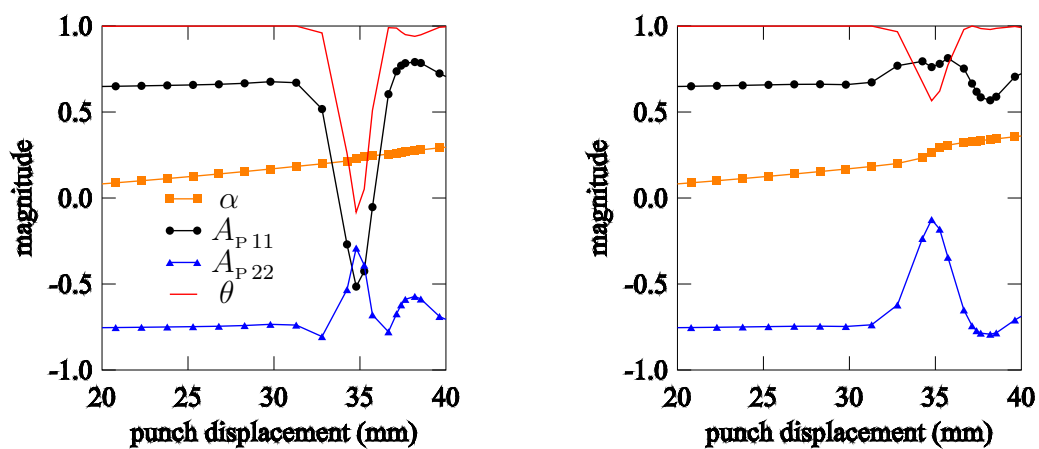


Figure 4.16: Evolution of  $\alpha$ ,  $A_P$  and  $\theta$  at a material point on the outside (left) and on the inside (right) in the middle of Ring 2 during deep drawing.

#### 4.4.3 Deep drawing of a square box

As the last application of the current material model, consider the case of the deep drawing of a square box (Figure 4.18). The blank has an initially square shape (200 mm by 200 mm) and is 0.82 mm thick. The die is modeled as a rigid surface with a square hole of 102.5 mm by 102.5 mm rounded at the edges by a radius of 10 mm. The rigid square punch measures 100 mm by 100 mm and is rounded at the edges by the same 10 mm radius. The drawing process is carried out with a load of 20 kN applied to the blank holder. The friction coefficient between the sheet and the punch is taken to be 0.25, and that between the sheet and the die is fixed at 0.125. It is assumed that there is no friction between the blank and the blank holder. For the finite-element simulation, one-quarter of the structure was discretized using conventional shell elements (S4R) with reduced integration for the blank, and three-dimensional rigid surface elements (R3D4) for the die, the punch and the blank holder (Figure 4.18). The springback simulation is carried out in two steps. First, the punch is removing for fixed holder and die. Secondly, fixing the center of the sheet, the die and holder are removed. For comparison, the simulations are also carried out with the combined hardening model. As before, we work here with DC06 and the parameter values given in 4.2 (Banu et al., 2001; Bouvier et al., 2003) discussed above. In addition, the initial flow anisotropy of DC06 is accounted for here. The corresponding Hill anisotropy

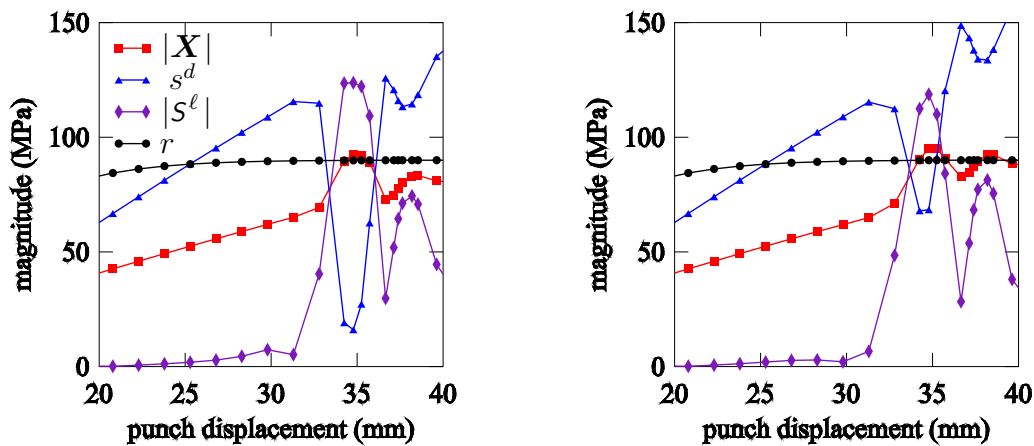


Figure 4.17: Evolution of the current model hardening variables at a material point on the outside (left) and on the inside (right) in the middle of Ring 2 during deep drawing.

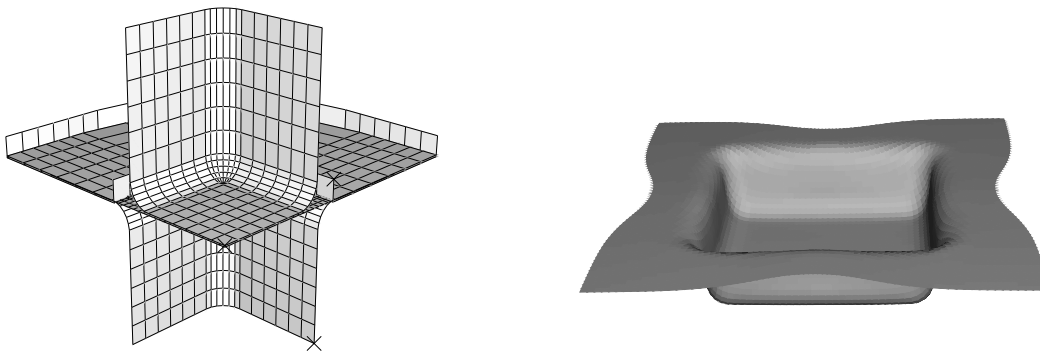


Figure 4.18: Left: Square-box finite-element structure for deep drawing simulation example. Right: Simulated form for the deep-drawn square box.

coefficients are  $F = 0.243$ ,  $G = 0.297$ ,  $H = 0.703$  and  $N = 1.2$  (Banu et al., 2001).

To begin, consider the predicted spatial distribution of the directional hardening in the structure before and after springback. This is displayed in Figure 4.19 for  $s^d$  (above) and  $|S^\ell|$  (below). As expected from the model behavior, note that the dynamic contribution  $s^d$  to directional hardening is transferred in the corner area of the box to  $S^\ell$  during elastic unloading and springback. Interestingly, this is strongest not directly in the center of the corner itself, but rather in the immediate neighborhood around it.

To look into this in more detail, consider again individual material points in the structure as shown in Figure 4.20. For the case of residual stress development, for example, consider the distribution of the von Mises in the side and the corner area of the outward surface of the box as shown in Figure 4.20. The corresponding stress distribution is shown in Figure 4.21 for the side (left) and the corner (right) areas, respectively. Note that in the side area the combined hardening model yields larger residual stresses, while in the corner area the current model. The reason for this is that the side area experiences mainly bending-unbending similar to the draw-

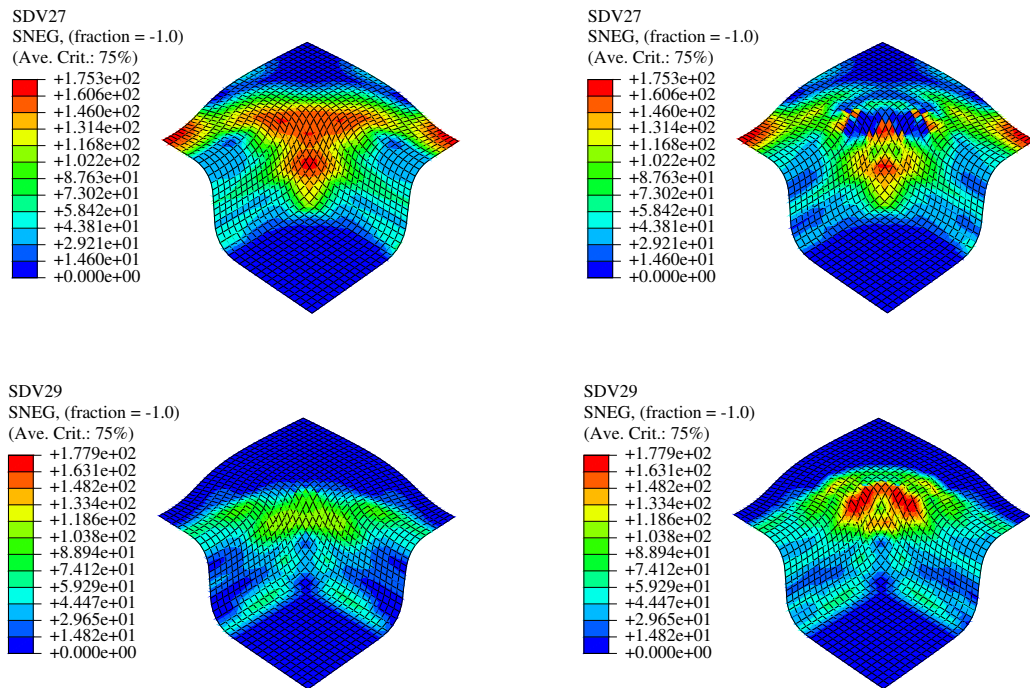


Figure 4.19: Spatial variation of  $s^d$  (above) and  $|S^l|$  (below) before (left) and after (right) springback. All values in MPa.

bending case. This implies only strain reversal as the strain-path change while the deformation conditions in the corner area are similar to those in the cup deep-drawing process (Figure 4.22), implying a strain-path change close to orthogonal during the bending stage. As discussed above, the combined hardening model behaves harder in the case of load reversal due to the absence of hardening stagnation. This results in higher residual stresses in the side area. On the other hand, the current model behaves harder in the case of orthogonal loading due to cross hardening, resulting in higher residual stresses in the corner area.

## 4.5 Conclusions

In this work, a material model taking isotropic, kinematic, hardening stagnation and cross hardening effects into consideration for continuous and discontinuous non-proportional loading path histories has been implemented and applied to various sheet metal forming processes. The simulation results have shown the important role of the directional hardening under complex strain path changes. In the case of draw-bending test, where the Basuschinger effect is the dominant phenomena, the hardening stagnation effects resulting from dynamic directional hardening contributions result in a deviation of the current model behavior from standard combined hardening. In the case of cylindrical or square deep-drawing, orthogonal strain-path changes and so latent contributions to directional hardening become significant and influence the residual stress state development and so the springback behavior. Moreover, due to the inhomogeneous nature of the deformation, these effects are inhomogeneous in the structure. Of course, the magnitude of hardening stagnation and directional effects is strongly material- and microstructure-

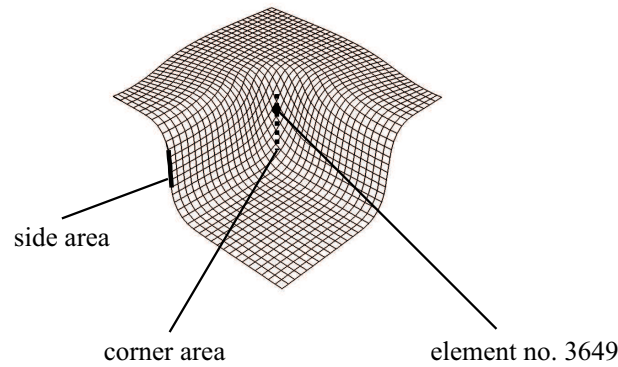


Figure 4.20: Finite-element mesh of the deep-drawn square box showing Element 3649 as well as the side and corner areas discussed in the text. In each area, 6 elements from the upper end to the lower end are considered. These are labeled as positions 1, . . . , 6 in Figure 4.21 below.

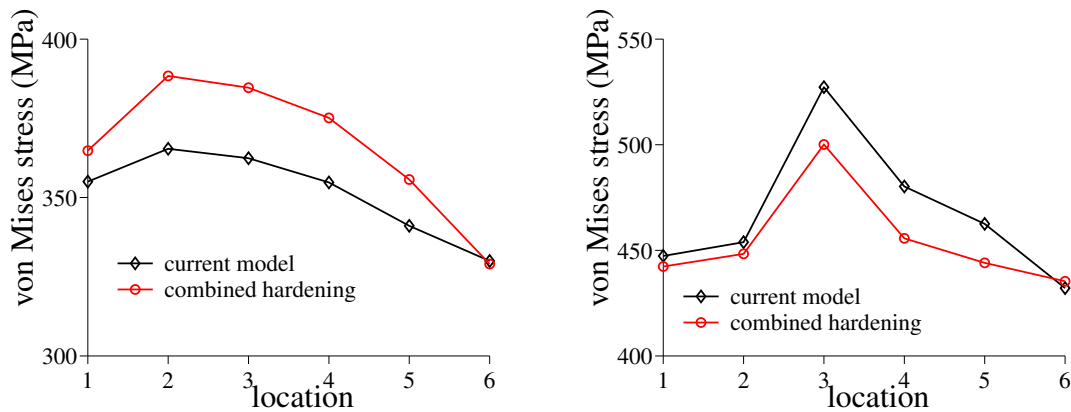


Figure 4.21: von Mises stresses distribution along the side (left) and along the corner (right) for the case of combined hardening and the current model. The location of the elements where the stresses are measure is shown as Figure 4.20.

dependent. For example, DP600 exhibits basically no cross hardening, while DC06 shows very strong cross hardening. Some studies have been carried out to explain why such materials have different hardening behavior under the same strain-path change (*e.g.*, Gardey et al., 2005a,b). Apparently, the detailed mechanisms of dislocation structure breakdown and reinforcement is extremely microstructure- and material-dependent.

This clearly represents work in progress. Additional aspects of such work include for example extension of the model to take into account a change in shape of the yield surface. Indeed, the flow anisotropy as represented by  $A_{Hill}$  is assumed constant in the current model, something that may not hold for materials with a stronger texture than those investigated here. In this case,  $A_{Hill}$  is also modeled as an evolving structure tensor – internal variable, and the plastic spin may become important (*e.g.*, Levkovitch et al., 2006; Wang et al., 2006d). As well, additional processes such as wrinkling, geometric instability, damage, and the attendant consequences for forming limits, are all influenced by the hardening behavior of the material, and are being incorporated into an extended version of it which will be reported on in the future.

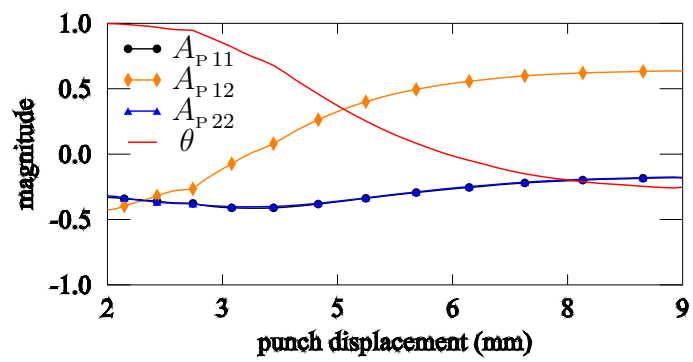


Figure 4.22: Evolution of  $A_p$  and  $\theta$  in element 3649 during the deep-drawing stage. Element 3649 is located in the middle of the corner area on the outward surface of the box as shown in Figure 4.20.





## References

- Asnafi, N., Springback and fracture in V-die bending of thick stainless steel sheets, *Materials and Design*, Volume 21, pp. 217–236, 2000.
- Baba, A., Tozawa, Y., Effect of tensile force in stretch-forming process on the springback, *Bulletin of JSME*, Volume 7, pp. 834–843, 1964.
- Banu, M., Bouvier, S., Haddadi, H., Maier, C., Tabacaru, V., Teodosiu, C., Selection and identification of the elastoplastic models for the materials used in the benchmarks of the 3DS research project, Report of LPMTM-CNRS, IMS 1999 000051, University Paris 13, Villetaneuse, France, 2001.
- Belytschko, T., Liu, W., Moran, B., *Nonlinear Finite Elements for Continua and Structures*, John Wiley & Sons Ltd., London, UK, 2000.
- Bertram, A., Description of finite inelastic deformations, in A. Benallal, R. Billardon, D. Marquis (editors), *Proceedings of MECAMAT '92 Multiaxial Plasticity*, pp. 821–835, 1993.
- Boehler, J. P., A simple derivation of representations for non-polynomial constitutive equations in some cases of anisotropy, *Zeitschrift für Angewandte Mathematik und Mechanik*, Volume 59, pp. 157–167, 1979.
- Bouvier, S., Alves, J., Oliveira, M., Menezes, L., Modelling of anisotropic work-hardening behaviour of metallic materials subjected to strain-path changes, *Computational Materials Science*, Volume 32, pp. 301–315, 2005.
- Bouvier, S., Gardey, B., Haddadi, H., Teodosiu, C., Characterization of the strain-induced plastic anisotropy of rolled sheets by using sequences of simple shear and uniaxial tensile tests, *Journal of Materials Processing Technology*, Volume 174, pp. 115–126, 2006.
- Bouvier, S., Teodosiu, C., Haddadi, H., Tabacaru, V., Anisotropic work-hardening behaviour of structural steels and aluminium alloys at large strains, *J. Phys. IV France*, Volume 105, pp. 215–222, 2003.
- Cao, J., Shi, M. F., Stoughton, T. B., Wang, C. T., Zhang, L., NUMISHEET 2005, Part B, AIP Conference Proceedings, Volume 778, pp. 881–1190, American Institute of Physics, Detroit, Michigan, USA, 2005.
- Carden, W. D., Geng, L. M., Matlock, D. K., Wagoner, R. H., Measurement of springback, *International Journal of Mechanical Science*, Volume 44, pp. 79–101, 2002.
- Chan, K. C., Theoretical analysis of springback in bending of integrated circuit leadframes, *International Journal of Materials Processing Technology*, Volume 91, pp. 111–115, 1999.
- Chen, X. M., Shi, M. F., Ren, R., Xia, Z. C., Springback prediction on slit-ring test, in *Proceedings of NUMISHEET 2005*, pp. 222–227, Detroit, Michigan, USA, 2005.
- Chun, B. K., Jinn, J. T., Lee, J. K., Modeling the Bauschinger effect for sheet metals, part I : theory, *International Journal of Plasticity*, Volume 18, pp. 571–595, 2002.
- Coleman, B., Gurtin, M., Thermodynamics with internal state variables, *Journal of Chemical Physics*, Volume 47, 1967.

- Dafalias, Y., The plastic spin, *Journal of Applied Mechanics*, Volume 52, pp. 865–871, 1985.
- Dafalias, Y. F., Plastic spin: necessity or redundancy, *International Journal of Plasticity*, Volume 14, pp. 909–931, 1998.
- Dafalias, Y. F., Orientational evolution of plastic orthotropy in sheet metals, *Journal of the Mechanics and Physics of Solids*, Volume 48, pp. 2231–2255, 2000.
- Davies, R. G., Liu, Y. C., Control of springback in flanging operation, *Journal of Applied Metal Working*, Volume 3, pp. 142–147, 1984.
- Dettmer, W., Reese, S., On the theoretical and numerical modeling of Armstrong-Frederick kinematic hardening in the finite-strain regime, *Computer Methods in Applied Mechanics and Engineering*, Volume 193, pp. 87–116, 2004.
- Edelen, D. G. B., On the existence of symmetry relations and dissipation potentials, *Archive for Rational Mechanics and Analysis*, Volume 51, pp. 218–227, 1973.
- Focellese, A., Fratini, L., Gabrielli, F., Micari, F., The evaluation of springback in 3D stamping and coining processes, *Journal of Materials Processing Technology*, Volume 81, pp. 108–112, 1998.
- Gardey, B., Bouvier, S., Bacroix, B., Correlation between the macroscopic behavior and the microstructural evolutions during large plastic deformation of a dual-phase steel, *Metallurgical and Materials Transactions A*, Volume 36A, pp. 2937–2945, 2005a.
- Gardey, B., Bouvier, S., Richard, V., Bacroix, B., Texture and dislocation structures observation in a dual-phase steel under strain-path changes at large deformation, *Materials Science and Engineering A*, Volume 400-401, pp. 136–141, 2005b.
- Gelin, J. C., Picart, P., *Proceedings of NUMISHEET 1999*, University of Franche-Compte, Besancon, France, 1999.
- Geng, L. M., Wagoner, R. H., Springback analysis with a modified hardening model, *Journal of Materials and Manufacturing*, Volume 109, pp. 365–375, 2000.
- Ghosh, A. K., Backofen, W. A., Strain-hardening and instability in biaxially stretched sheets., *Metallurgical Transactions*, Volume 4, pp. 1113–1123, 1973.
- Govindarajan, R., Schikorra, M., Brosius, A., Kleiner, M., Einfluss geometrischer Skalierung und isotrop-kinematisch kombinierter Verfestigungsmodelle bei der Simulation der Ruckfederung, *Strahltechnik*, Volume 27, pp. 95–104, 2005.
- Haddadi, H., Bouvier, S., Banu, M., Maier, C., Teodosiu, C., Towards an accurate description of the anisotropic behaviour of sheet metals under large plastic deformations: modelling, numerical analysis and identification, *International Journal of Plasticity*, Volume 22, pp. 2226–2271, 2006.
- Haddag, B., Balan, T., Abed-Meraim, F., Springback simulation: impact of some advanced constitutive models and numerical parameters, in *Proceedings of NUMISHEET 2005*, pp. 286–291, Detroit, Michigan, U.S.A., 2005.
- Han, W., Reddy, B. D., *Plasticity: Mathematical Theory and Numerical Analysis*, Springer

- Series on Mechanics and Materials, Volume 9, 1999.
- Hauptmann, R., Schweizerhof, K., A systematic development of "solid-shell" element formulations for linear and non-linear analyses employing only displacement degrees of freedom, *International Journal for Numerical Methods in Engineering*, Volume 42, pp. 49–69, 1998.
- He, N., Wagoner, R. H., Springback simulation in sheet metal forming, in *Proceedings of NUMISHEET 1996*, pp. 308–315, The Ohio State University, Columbus, Ohio, USA, 1996.
- Hiwatashi, S., Bael, A. V., Houtte, P. V., Teodosiu, C., Modelling of plastic anisotropy based on texture and dislocation structure, *Computational Materials Science*, Volume 9, pp. 274–284, 1997.
- Hiwatashi, S., Bael, A. V., Houtte, P. V., Teodosiu, C., Prediction of forming limit strains under strain-path changes: application of an anisotropic model based on texture and dislocation structure, *International Journal of Plasticity*, Volume 14, pp. 647–669, 1998.
- Hoc, T., Forest, S., Polycrystal modelling of IF-Ti steel under complex loading path, *International Journal of Plasticity*, Volume 17, pp. 65–85, 2001.
- Hoferlin, E., Incorporation of an accurate model with a texture based local description of the yield locus, Ph.D. thesis, Katholieke Universiteit Leuven, 2001.
- Hu, Y., Du, C., Quasi static finite element algorithms for sheet metal stamping springback simulation, in *Proceedings of NUMISHEET 1999*, pp. 71–76, University of Franche-Compte, Besancon, France, 1999.
- Huang, M., Gerdeen, J. C., Springback of doubly curved developable sheet metal surface, *Analysis of Autobody Stamping Technology*, Society of Automotive Engineers, 1994.
- Huang, Y. M., Leu, D. K., An elastoplastic finite element analysis of sheet metal U-bending process, *Journal of Materials Processing Technology*, Volume 48, pp. 151–157, 1995.
- Huang, Y. M., Leu, D. K., Effects of process variables on V-die bending process of steel sheet, *International Journal of Mechanical Sciences*, Volume 40, pp. 631–650, 1998.
- Kleiner, M., M. M. S., Brosius, A., Analysis of a measurement system for the characterisation of springback, in Vollertsen, F. (editor), *Proceedings of the 1<sup>st</sup> Colloquium of the DFG Priority Program on Process Scaling*, Volume 19, pp. 11–18, 2003.
- Kleiner, M., Schikorra, M., Govindarajan, R., Brosius, A., Springback analysis of sheet metals regarding material hardening, in *Proceedings of the 11<sup>th</sup> International Conference on Sheet Metal*, pp. 712–728, Erlangen, Germany, 2005.
- Lee, J. K., Kinzel, G. L., Wagoner, R. H., *Proceedings of NUMISHEET 1996*, The Ohio State University, Columbus, USA, 1996.
- Lee, S. W., Yang, D. Y., An assessment of numerical parameters influencing springback in explicit finite element analysis of sheet metal forming process, *Journal of Materials Processing Technology*, Volume 80, pp. 60–67, 1998.
- Lemaitre, J., Chaboche, J. L., *Mechanics of solid materials*, Cambridge University Press, 1990.

- Levkovitch, V., Svendsen, B., Wang, J., Micromechanically motivated phenomenological modeling of induced flow anisotropy and its application to sheet forming processes with complex strain path changes, in Proceedings of ESAFORM 2006, pp. 179–182, Galsgow, UK, 2006.
- Levy, B. S., Empirically derived equations for predictiong springback in bending, Journal of Applied Metalworking, Volume 3, pp. 135–141, 1984.
- Li, K. P., Geng, L. M., Wagoner, R. H., Simulation of springback: choice of element, in Advanced Technology of Plasticity, Volume III, pp. 2091–2098, Springer, Berlin, 1999.
- Li, S., Hoferlin, E., Bael, A., Houtte, P., Teodosiu, C., Finite element modeling of plastic anisotropy induced by texture and strain-path change, International Journal of Plasticity, Volume 19, pp. 647–674, 2003.
- Liu, I. S., On representations of anisotropic invariants, International Journal of Engineering Science, Volume 20, pp. 1099–1109, 1982.
- Makinouchi, A., Nakamachi, E., Onate, E., Wagoner, R. H., Proceedings of NUMISHEET 1993, The Institute of Physical and Chemical Research, Isehara, Japan, 1993.
- Mandel, J., Thermodynamics and Plasticity, in Foundations of Continuum Thermodynamics Delgado Domingos, MacMillan, 1974.
- Martin, G., Tsang, S., The plastic bending of beams considering die friction effects, Journal of Engineering for Industry, Volume 88, pp. 237–250, 1966.
- Mattiasson, K., Strange, A., Thilderkvist, P., Samuelsson, A., Simulatuion of springback in sheet metal forming, in Proceedings of NUMIFORM 1995, pp. 115–124, New York, USA, 1995.
- Meinders, T., Konter, A., Meijers, S., Atzema, E., Kappert, H., A Sensitivity analysis on the srpingback behavior of the unconstrained bending problem, in Proceedings of NUMISHEET 2005, pp. 272–277, Detroit, Michigan, U.S.A., 2005.
- Mickalich, M. K., Wenner, M. L., Calculation of springback and its variation in channel forming operations, in Proceedings of Advances and Trends in Automotive Sheet Metal Stamping, pp. 99–100, Society of Automotive Engineers, Warrendale, Pennsylvania, USA, 1988.
- Montleau, P. D., Programming of the Teodosiu's hardening model, IAP P5/08 progress report, (internal report), 2004.
- Narasimhan, N., Lovell, M., Predicting springback in sheet metal forming: an explicit to implicit sequential solution procedure, Finite Elements in Analysis and Design, Volume 33, pp. 29–42, 1999.
- Nesterova, E. V., Bacroix, B., Teodosiu, C., Experimental observation of microstructure evolution under strain-path changes in low-carbon IF steel, Material Science and Engineering, Volume A309-310, pp. 495–499, 2001a.
- Nesterova, E. V., Bacroix, B., Teodosiu, C., Microstructure and texture evolution under strain-path changes in low-carbon interstitial-free steel, Metallurgical and Materials transaction, Volume 32A, pp. 2527–2538, 2001b.

- Park, D. W., Kang, J. J., Hong, J. P., Oh, S. I., Springback simulation by combined method of explicit and implicit FEM, in Proceedings of NUMISHEET 1999, pp. 35–40, University of Franche-Compte, Besancon, France, 1999.
- Queener, C. A., Angelis, R. J. D., Elastic springback and residual stresses in sheet metal formed by bending, Transactions of ASM, Volume 61, pp. 757–768, 1968.
- Rauch, E. F., Schmitt, J. H., Dislocation substructures in mild steel deformed in simple shear, Material Science and Engineering, Volume A113, pp. 441–448, 1989.
- Rauch, E. F., Thuillier, S., Rheological behaviour of mild steel under monotonic loading conditions and cross-loading, Material Science and Engineering, Volume A164, pp. 255–259, 1993.
- Reese, S., Svendsen, B., On the use of evolving structure tensors to model initial and induced elastic and inelastic anisotropy at finite deformation, Journal de Physique IV, Volume 14, pp. 31–37, 2003.
- Rockafellar, R. T., Convex Analysis, Princeton University Press, 1973.
- Rohleder, M., Roll, K., Brosius, A., Kleiner, M., Investigation of springback in sheet metal forming using two different testing methods, in Proceedings of ESAFORM 2001, pp. 321–324, Liège, Belgium, 2001.
- Samuel, M., Experimental and numerical prediction of springback and side wall curl in U-bendings of anisotropic sheet metals, Journal of Materials Processing Technology, Volume 105, pp. 382–393, 2000.
- Shaffer, B. W., House, J. R. N., the elastic-plastic stress distribution within a wide curved bar subjected to pure bending, ASME Journal of Applied Mechanics, Volume 22, pp. 305–310, 1955.
- Simo, J. C., Hughes, T. J., Computational Inelasticity, Springer Verlag, 1998.
- Strano, M., Robustness evaluation and tolerance prediction for a stamping process with springback calculation by the FEM, in Proceedings of NUMISHEET 2005, pp. 266–271, Detroit, Michigan, USA, 2005.
- Strauven, Y., Aernoudt, E., Directional strain softening in ferritic steel, Acta Metallurgica, Volume 35, pp. 1029–1036, 1987.
- Sudo, C., Kojima, M., Matsuoka, T., Some investigations on elastic recovery of press formed parts of high strength steel sheets, in Proceedings of IDDRG 1974, pp. 192–202, Goteborg, Sweden, 1974.
- Svendsen, B., On the representation of constitutive relations using structure tensors, International Journal of Engineering Science, Volume 12, pp. 1889–1892, 1994.
- Svendsen, B., A thermodynamic formulation of finite-deformation elastoplasticity with hardening based on the concept of material isomorphism, International Journal of Plasticity, Volume 14, pp. 473–488, 1998.
- Svendsen, B., On the modeling of anisotropic elastic and inelastic material behaviour at large

- deformation, *International Journal of Solids and Structures*, Volume 38, pp. 9579–9599, 2001.
- Tan, Z., Persson, B., Magnusson, C., An empiric model for controlling springback in V-die bending of sheet metals, *Journal of Materials Processing Technology*, Volume 34, pp. 449–455, 1992.
- Teodosiu, C., Hu, Z., Evolution of the intragranular microstructure at moderate and large strains: modelling and computational significance, in S. F. Shen, P. R. Dawson (editors), *Proceedings of Simulation of Materials Processing: Theory, Methods and Applications*, pp. 173–182, Balkema, Rotterdam, 1995.
- Teodosiu, C., Hu, Z., Microstructure in the continuum modelling of plastic anisotropy, in J. V. Carstensen, T. Leffers, T. Lorebzen, O. B. Pedersen, B. F. Sorensen, G. Winther (editors), *Proceedings of 19<sup>th</sup> Risø International Symposium on Material's Science: Modelling of Structure and Mechanics of Materials from Microscale to Product*, pp. 149–168, Risø National Laboratory, Roskilde, Denmark, 1998.
- Thuillier, S., Rauch, E. F., Development of microbands in mild steel during cross loading, *Acta Metallurgica et Materialia*, Volume 42, pp. 1973–1983, 1994.
- Truesdell, C., Noll, W., *The Non-Linear Field Theories of Mechanics*, Second Edition, Springer-Verlag, 1992.
- Ueda, M., Ueno, M., Kobayashi, M., A study of springback in the stretch bending of channels, *Journal of Mechanics and Working Technology*, Volume 5, pp. 163–179, 1981.
- Šilhavý, M., *The Mechanics and Thermodynamics of Continuous Media*, Springer Verlag, 1997.
- Wagoner, R. H., Li, K. P., Carden, W. P., Simulation of springabck, *International Journal of Mechanical Sciences*, Volume 44, pp. 103–122, 2002.
- Wagoner, R. H., Li, M., Advances in springback, in *Proceedings of NUMISHEET 2005*, pp. 209–214, Detroit, Michigan, USA, 2005.
- Wang, C. C., Bloom, J., Material uniformity and inhomogeneity in anelastic bodies, *Archive for Rational Mechanics and Analysis*, Volume 53, pp. 246–276, 1974.
- Wang, J. F., Principles of the draw-bend spirngback test, Ph.D. thesis, The Ohio State University, Columbs, Ohio, USA, 2004.
- Wang, J., Levkovitch, V., Reusch, F., Svendsen, B., Modeling and simulation of induced anisotropic hardening and springback in sheet metals during non-proportional loading, in *Proceedings of NUMISHEET 2005*, pp. 234–239, Detroit, Michigan, USA, 2005a.
- Wang, J., Levkovitch, V., Reusch, F., Svendsen, B., On the modeling and simulation of induced anisotropy in polycrystalline metals with application to springback, *Archive of Applied Mechanics*, Volume 74, pp. 890–899, 2005b.
- Wang, J., Levkovitch, V., Reusch, F., Svendsen, B., Modeling and simulation of directional hardening in metals during non-proportional loading, *Journal of Materials Processing Tech-*

- nology, Volume 176, pp. 430–432, 2006a.
- Wang, J., Levkovitch, V., Svendsen, B., Application of directional hardening modeling to the simulation of sheet metal forming and springback, *International Journal of Mechanical Sciences*, submitted, 2006b.
- Wang, J., Levkovitch, V., Svendsen, B., On some numerical aspects of the simulation of sheet metal forming and springback, *Journal of Materials Processing Technology*, submitted, 2006c.
- Wang, J., Levkovitch, V., Svendsen, B., On the modeling and simulation of directional hardening in metals, *International Journal of Plasticity*, submitted, 2006d.
- Wenner, M. L., On the work hardening and springback in plane strain draw forming, *Journal of Applied Metalworking*, Volume 2, pp. 277–287, 1983.
- Wilson, D. V., Bate, P. S., Influences of cell walls and grain boundaries on transient responses of an IF steel to changes in strain path, *Acta Metall. Mater.*, Volume 42, pp. 1099–1111, 1994.
- Yoshida, F., Uemori, T., A model of large-strain cyclic plasticity and its application to springback simulation, *International Journal of Mechanical Sciences*, Volume 45, pp. 1687–1702, 2003.
- Yuen, W., Springback in the stretch-bending of sheet metal with non-uniform deformation, *Journal of Materials Processing Technology*, Volume 22, pp. 1–20, 1990.
- Zhang, J. M., Rychlewski, J., Structural tensors for anisotropic solids, *Archives of Mechanics*, Volume 42, pp. 267–277, 1990.
- Zhang, Z. T., Lee, D., Effect of process variables and material properties on the springback of 2D-draw bending parts, in *Proceedings of Automotive Stamping Technology*, pp. 11–18, Society of Automotive Engineers, Detroit, USA, 1995.





# Acknowledgements

The work presented in this thesis was carried out between 2003 and 2006 during my time as a Ph.D. student at the Chair of Mechanics, University of Dortmund. Having come to the end, I would like to express my thanks to all the people here who gave me tremendous support and help in the last three years.

First of all, I would like to express my heartfelt thanks to my academic advisor Professor Bob Svendsen for his scientific support and seasoned guidance. Without his work in the fields of material modeling and computational mechanics, this thesis could not have been achieved. Further, I would like to thank Professor Karl Roll and Professor Marc Geers for their interest in my work and willingness to act as the external examiner of this thesis. My special thanks also go to the chief engineers of our group Dr. Vladislav Levkovitch and Dr. Fredrick Reusch for their help with all aspects of the work, willingness to answer my question and for their friendship. In particular, much of the material and structural modeling in my thesis is based on detailed scientific discussions with Dr. Levkovitch.

Next I want to thank my fellow workers responsible for the friendly atmosphere in the group. Especially, I would like to express my gratitude to my Mr. Jaan Unger for his great support, help and the many discussions we had on various scientific issues. Furthermore, I would like to thank Mr. Tobias Kayser for his continuous support in the area of computational hardware and software facilities. I also appreciate Mr. Xin Gu and Mr. Christian Hortig for sharing their ideas concerning mechanical and computational issues throughout the years. Special thanks would go to Mrs. Kerstin Walter for her years warm help for my research, business travelling issues and solving my daily inconvenience such as language problem in living in Dortmund. Thank Miss Christine Vu for her excellent language correction of the thesis and papers. I also thank Professor Klaus Thermann and his Ph.D. students Miss Andrea Schuetze and Mr. Vadim Palnau for their kind help and time during the last three years.

Finally, I want to thank my wife Ying Yang for giving me so much moral support during our stay in Germany. She dealt with our everyday-life problems for me, freeing me to pursue my research activities. Special thanks also goes to my old friend Dr. Yiping Shi who supported me so much. Last but not least I would like to extend my heartfelt thanks to my friend Dr. Achim Schneider for his great support and help in Germany.

Dortmund, August 2006

*Jian WANG*



# Curriculum Vitae

## Personal

Name: Wang Jian  
Date of Birth: April 21, 1972  
Place of Birth: Hebei, China  
Nationality: Chinese

## Education and Experience

1978-1990 Primary and middle schools, Hebei, China  
1990-1994 B.Sc. study, Department of Metal Forming, University of Science and Technology Beijing, China  
1994-1997 M.Sc. research, Department of Metal Forming, University of Science and Technology Beijing, China  
1997-2003 Project manager, China Metallurgical Equipment Corporation, China  
2003-2006 Graduate Student, Chair of Mechanics, University of Dortmund, Germany